

## TABLE OF CONTENTS

	Page
INTRODUCTION .....	1
CHAPTER 1 LITERATURE REVIEW .....	3
1.1 Wire and arc additive manufacturing processes .....	3
1.1.1 GTAW-based WAAM.....	5
1.1.2 PAW-based WAAM.....	6
1.1.3 GMAW-based WAAM.....	8
1.2 The challenges of manufacturing by WAAM.....	10
1.2.1 Surface roughness .....	10
1.2.2 Microstructure and gas porosity.....	10
1.2.3 Residual stress and distortion.....	13
CHAPTER 2 FEASIBILITY STUDY OF ALUMINUM DEPOSITION BY ROBOTIC MIG WELDING PROCESS .....	17
Abstract.....	17
2.1 Introduction.....	18
2.2 Experimental description .....	22
2.3 Results and discussion .....	26
2.4 Conclusion .....	34
CHAPTER 3 ASSESSING THE EFFECTS OF SYNERGIC GMAW-P PARAMETERS ON WELD CURRENT AND HEAT INPUT IN ALUMINUM ROBOTIC ARC WELDING USING THE DESIGN OF EXPERIMENTS.....	35
Abstract.....	35
3.1 Introduction.....	36
3.2 Experimental Procedure.....	37
3.3 Results and Discussion .....	40
3.4 Summary and Conclusion.....	50
CHAPTER 4 AN INVESTIGATION ON THE EFFECTS OF WELD CURRENT AND HEAT INPUT ON THE SURFACE QUALITY, MICROSTRUCTURE, AND MECHANICAL PROPERTIES OF THIN-WALL PIECES OF AL-SI ALLOY MADE BY GMAW-BASED WAAM .....	53
Abstract.....	53
4.1 Introduction.....	54
4.2 Experimental procedure .....	55
4.3 Results and Discussion .....	59
4.3.1 Surface quality and accuracy .....	59
4.3.2 Microstructure and hardness.....	62

4.3.3	Porosity .....	65
4.3.4	Mechanical properties .....	69
4.3.5	Conclusions.....	70
CONCLUSION .....		71
RECOMMENDATIONS.....		73
LIST OF BIBLIOGRAPHICAL REFERENCES.....		75

## LIST OF TABLES

	Page
Table 1-1	Metal wire feed and heat source used by WAAM processes.....4
Table 2-1	Important parameters affecting the performance of GMAW-P .....19
Table 2-2	Chemical composition of ER4043 and 6061 alloy (WT %).....23
Table 2-3	Mechanical properties of ER4043 .....24
Table 2-4	Welding parameters of the tests .....25
Table 2-5	Total porosity areas over testing area in %.....27
Table 2-6	Summary of images' analysis results of area 1 by ImageJ software .....28
Table 3-1	Chemical composition of ER4043 and 6061 alloy (wt %) .....38
Table 3-2	Initial settings of the parameters .....39
Table 3-3	Terminology and definitions.....39
Table 3-4	Factors and interval values of the test.....40
Table 3-5	Selected tests based on the quality of the weld bead .....41
Table 3-6	Analysis of Variance for $I_{avg}$ .....42
Table 3-7	Analysis of Variance for H.I.....45
Table 3-8	Practical results of welding.....49
Table 4-1	Chemical compositions of ER4043 and 6061 alloy (wt.%).....56
Table 4-2	Mechanical properties of ER4043 .....56
Table 4-3	Welding parameters .....57
Table 4-4	Characteristics of the walls .....57
Table 4-5	Surface roughness parameters for each roughness profile.....61
Table 4-6	Microhardness and grain size at the top section of walls.....64
Table 4-7	Microhardness test results and grain size at the middle section of walls...65

Table 4-8	Summary of porosity analysis by ImageJ software .....	66
Table 4-9	Porosities classified based on their size and percentage.....	67
Table 4-10	Tensile test Results.....	70

## LIST OF FIGURES

		Page
Figure 1.1	Schematic of GTAW-based WAAM.....	5
Figure 1.2	Conventional TIG torch (a), TOPTIG torch (b, c).....	6
Figure 1.3	Schematic of PAW-based WAAM. ....	7
Figure 1.4	Plasma welding robotic torch with wire feeder (a), Plasma Arc Welding (PAW) Print 3-Dimensional (PP3D) (b).....	8
Figure 1.5	Schematic of GMAW-based WAAM.....	9
Figure 1.6	The effects of variable polarity arc on the melt pool and the solidification process.....	12
Figure 1.7	Performance of workpiece vibration for grain refinement; (a) the illustration of the weld pool when using conventional pulse arc; (b) the illustration of the weld pool when using VP-CMT; (c) enlarged illustration of part A in b and showing the effect of bending stress due to vibration on dendritic arms breakage; (d) the illustration of the weld pool after vibration stabilization. ....	13
Figure 1.8	Distribution of residual stress before unclamping (a), distribution of residual stress after unclamping (b), distortion after unclamping (c). ....	14
Figure 1.9	Schematic diagram of the main rolling methods: (a) vertical with a profiled roller; (b) in-situ rolling; (c) pinch rolling (d) rolling with an inverted profiled roller for thick sections and intersections.....	15
Figure 2.1	Schematic of a current–time diagram during pulse-spray welding. ....	19
Figure 2.2	Solubility of hydrogen in aluminum at various temperatures.....	21
Figure 2.3	The effects of variable polarity arc on the melt pool and the solidification process.....	22
Figure 2.4	Fronius TransPuls Synergic 4000, (b) YASKAWA MOTOMAN arm.....	23
Figure 2.5	Effect of DYN on weld droplet.....	24
Figure 2.6	(a) Construction process of the wall by the welder robotic arm, (b) the images of the three walls made, (c) tested areas and locations.....	26

Figure 2.7	Stitched images of the tests and comparison of the walls in terms of EWT and SW values.....	27
Figure 2.8	Analyzed images by ImageJ software for Area 1. ....	28
Figure 2.9	Porosity percentage.....	29
Figure 2.10	Metallography images of samples from the height of the walls with a magnification of 500×.....	30
Figure 2.11	Metallography images of samples from the height of the walls with a magnification of 100×.....	31
Figure 2.12	Hardness profile of the width of the walls. ....	32
Figure 2.13	Normal distribution diagram of hardness of the width of the walls. ....	33
Figure 2.14	Hardness profile of the height of the walls. ....	33
Figure 2.15	Normal distribution diagram of hardness of the height of the walls.....	33
Figure 3.1	The most effective parameters on $I_{avg}$ . (a) Normal plot; (b) Pareto chart. .	43
Figure 3.2	Interaction plots displaying significant trends between factors and response (A gray background represents a term not in the model).....	44
Figure 3.3	The most effective parameters on H.I. (a) Normal plot; (b) Pareto chart. .	46
Figure 3.4	Interaction plots displaying significant trends between factors and response (A gray background represents a term not in the model).....	47
Figure 3.5	Optimization plot for $I_{avg}$ . ....	49
Figure 3.6	The weld seam appearance. ....	49
Figure 3.7	Optimization plot for H.I. ....	50
Figure 4.1	(a) Fronius TransPuls Synergic 4000; (b) Yaskawa Motoman MH6 robot arm; (c) Schematic diagram of WAAM process.....	56
Figure 4.2	Photographs of the deposited walls: (a) First wall, (b) Second wall. ....	58
Figure 4.3	Position of samples. ....	59
Figure 4.4	(1a), (1b), and (1c) First wall surface roughness profiles; (2a), (2b), and (2c) Second wall surface roughness profiles. ....	60

Figure 4.5	The roughness average (Ra), the root mean square (RMS), the roughness (Rq), and the maximum roughness profile height (Rz). ....	61
Figure 4.6	Metallography images of walls: 1T, 2T - top sections of first wall and second wall; 1M, 2M - middle sections of first wall and second wall.....	63
Figure 4.7	The Al-Si phase diagram. ....	63
Figure 4.8	Images analyzed by ImageJ software: (a) first wall, (b) second wall. ....	66
Figure 4.9	Graphical representation of the number of porosities for each size range.	68
Figure 4.10	Graphical representation of the percentage of porosities for each size range.....	68



## LIST OF ABBREVIATIONS

AM	Additive Manufacturing
CM	Conventional Manufacturing
3D	Three-dimensional
WAAM	Wire and Arc Additive Manufacturing
GTAW	Gas Tungsten Arc Welding
PAW	Plasma Arc Welding
GMAW	Gas Metal Arc Welding
GMAW-P	Pulsed Gas Metal Arc Welding
MIG	Metal Inert Gas
TIG	Tungsten Inert Gas
DOE	Design of Experiments
BTF	Buy-to-fly
SMD	Shaped Metal Deposition
SLM	Selective Laser Melting
LMD	Laser Metal Deposition
PP3D	PAW Print 3D
DED	Directed Energy Deposition
PBF	Powder Bed Fusion
CMT	Cold Metal Transfer
STT	Surface Tension Transfer
ODPP	One Drop Per Pulse
HI	welding Heat Input
WFS	Wire Feed Speed
TS	Travel Speed
CTWD	Contact Tip-to-Work Distance
DYN	Dynamic/Pulse Correction
WT%	percentage by weight
OM	Optical Microscope
EWT	Effective Wall Thickness
SW	Surface Waviness
TPA	Total Porosity Areas
ANOVA	Analysis of Variance
DF	Degrees of Freedom
Adj SS	Adjusted sums of squares
Adj MS	Adjusted mean squares
F-value	Value on the Fisher–Snedecor distribution
p-value	Probability value
HAZ	Heat Affected Zone
UTS	Ultimate Tensile Stress
ANN	Artificial Neural Networks
GA	Genetic Algorithm
SMAW	Shielded Metal Arc Welding



## LIST OF SYMBOLS

kg/h	kilograms per hour
$\mu\text{m}$	micrometer
ipm	inches per minute
g	gram
ml	milliliter
m/min	meters per minute
mm	millimeter
cfh	cubic feet per hour
psi	pound-force per square inch
MPa	Megapascal
HV	Hardness in Vickers
V	volt
A	ampere
kJ/in	kilojoules per inch
$^{\circ}\text{C}$	degree Celsius or centigrade
$\alpha$	significance level
$R^2$	coefficient of determination
D	Durbin-Watson Statistic
$R_a$	roughness average
$R_q$	root mean square (RMS) roughness
$R_z$	maximum height of roughness profile



## INTRODUCTION

In recent decades, additive manufacturing techniques (AM), also referred to as 3D printing or rapid prototyping, have attracted the attention of various industries such as aerospace, automotive, and construction. AM is the process of manufacturing 3-D pieces by adding layer-upon-layer of material [1]. The various advantages of AM compared to conventional manufacturing (CM) processes can be discussed in three aspects. First, AM makes it possible to build complex components that are difficult to manufacture by the CM processes [2]. Second, the AM processes improve the buy-to-fly ratio by reducing the amount of waste material, which reduces the final price of the parts. Third, the AM process can have a significant impact on reducing energy consumption and protecting the environment by reducing both the production time and the weight of parts produced due to new designs or material modifications [3-5]. Wire and Arc Additive Manufacturing (WAAM) refers to a specific group of AM techniques that use an electric arc as the heat source and a metal wire as the feedstock. The WAAM technique uses arc welding processes and more specifically automated arc welding. The three welding methods commonly used in the WAAM technique are Gas Tungsten Arc Welding (GTAW), Plasma Arc Welding (PAW), and Gas Metal Arc Welding (GMAW). Therefore, WAAM technique is divided into three groups, namely GTAW-based WAAM, PAW-based WAAM, and GMAW-based WAAM [6-8]. The main advantage of WAAM over other AM techniques is that its deposition rate is higher, hence WAAM is used to produce large near-net-shape components. Another advantage of WAAM is its lower capital costs compared to other methods [9, 10].

Despite the increasing consumption of aluminum and its alloys in various industries due to its unique properties, such as high strength-to-weight ratio, high ductility, and high durability, most of the research and productions in the WAAM field have focused on the stainless steels, nickel and titanium alloys. The main reason is the gas pores and the coarse dendritic structure formation during the WAAM process, which leads to a severe loss of the mechanical properties of the aluminum alloy components [11, 12].

The research in WAAM field follows two branches to reduce the problems caused by gas pores, dendritic and coarse microstructures, and residual stresses. One area of research is interested in combining other AM techniques with WAAM methods [13-15] or adding equipment such as trailing gas shield [16-18], inter-pass cold rolling [19-21], Peening and ultrasonic impact treatment [16, 22, 23], etc. In other areas, researchers are focusing on improving the quality of WAAM components by improved welding parameters [24-26].

This study focuses on the development of wire and arc additive manufacturing (WAAM) parameters of aluminum alloys. A system consisting of a synergic pulsed GMAW source and a robotic arm was used to perform the WAAM process. The alloy and specimens studied are Al-Si alloy and the thin-walls made by the WAAM process, and each layer was made by depositing ER4043 filler metal.

This thesis is organized as follows. Chapter 1 presents the literature review that covers the research undertaken in the scope of this study and provides a necessary background for further discussion in the following chapters. Chapter 2 is for feasibility study of aluminum deposition by using the robotic MIG welding process, which describes the first steps to make the WAAM process operational with the available system. In Chapter 3, the evaluation of the effects of Synergic GMAW-P parameters on weld current and weld heat input using the design of experiments method (DOE) is detailed. Chapter 4 presents a parametric study using DOE where the effects of weld current and heat input on the surface quality, microstructure, and mechanical properties of the thin walls are investigated, which is followed finally by a summary and conclusions.

## CHAPTER 1

### LITERATURE REVIEW

Additive Manufacturing (AM) or 3D printing is an advanced group of manufacturing processes in which the components are manufactured directly layer by layer. Additive manufacturing enables the production of net-shape or near-net-shape components directly from 3D data and saves time, and tools and production costs [27]. The significant advantage of additive manufacturing versus subtractive manufacturing (traditional manufacturing that involves removing sections of the block of material by machining, milling, etc. for achieving the net-shape piece) is the lower buy-to-fly ratio (BTF) [28]. When the topic of discussion is metal additive manufacturing, one of the most commonly used methods is to use a heat source such as an arc, a high-energy electron beam, or a laser beam as a melting source. And a wire of metallic materials is used as feedstock to obtain the designed part by adding a molten wire layer upon layer. The term "Shaped Metal Deposition" (SMD) is commonly used for the mentioned method. Shaped Metal Deposition (SMD) is the name of a fabrication technology presented by Rolls-Royce plc and the University of Sheffield [29]. The main sections of an SMD system consist of: (i) Heat generation unit, which refers to an electric arc, an electron beam or a laser beam unit; (ii) Deposition metal supply unit, which refers to the metal wires and the wire-feed system; (iii) Deposition path movement system, which refers to a welder robot or every system for generating deposition path motion; and (iv) Control movement system, which refers to a control software program for deposition path movement system [30].

#### 1.1 Wire and arc additive manufacturing processes

Wire and Arc Additive Manufacturing (WAAM) is an AM approach that consists of a combination of metal wire feed and arc welding [31]. The type of arc welding process chosen depends on the possibility of its automation. Therefore, Gas Tungsten Arc Welding (GTAW), Plasma Arc Welding (PAW) and Gas Metal Arc Welding (GMAW) are the main options to select as the heat source for the WAAM [32].

The WAAM deposit rate is higher than the other AM methods. For example, Selective Laser Melting (SLM) steel deposition rates reach 0.1 (kg/h), and Laser Metal Deposition (LMD) can reach up to 1 (kg/h) steel deposit, but the steel deposition rate for WAAM technology is 5-6 (kg/h). This advantage leads WAAM to be used to produce large parts [33, 34]. The electric arc has a focused spot radius size in the range of a few millimeters (the focused spot radius for the laser beam is 50 ( $\mu\text{m}$ ), and the electron beam is 100 ( $\mu\text{m}$ )). Hence, the surface roughness of produced pieces by WAAM is high and there is usually a machining step needed after manufacturing by WAAM [35].

WAAM processes generally use commercial welding wire spools as feedstock. Furthermore, ordering special metal alloy in the form of wire spool is also possible[36]. Some of the metal alloys are listed in Table 1.1 along with the heat source used in recent WAAM research.

Table 1-1 Metal wire feed and heat source used by WAAM processes

Metal wire feed	Heat source	References
Mild steel (ER70S-6)	GMAW, PAW	[37-39]
H08Mn2Si	GMAW	[40]
Stainless steel (316L,316L-Si)	GMAW, GTAW, PAW	[41-45]
Stainless steel (17-4 Ph)	GMAW	[46, 47]
Duplex stainless steel (ER-2594)	GMAW, GTAW	[48, 49]
HSLA AWS A5.28 (ER-110S-G)	GMAW, PAW	[50-52]
Hot work tool steel 1.2343 (37CrMoV5-1)	GMAW	[53]
Aluminum alloy (ER-2319)	GTAW	[54]
Aluminum alloy (ER-4043)	GMAW	[55]
Aluminum alloy (ER-4047)	GMAW	[56]
Aluminum alloy (ER- 5356)	GMAW	[56, 57]
High purity (99.99%) iron &1080 (Pure Aluminum)	GTAW	[58]
Ti-6Al-4V&1080 (Pure Aluminum)	GTAW	[59]
Ti-6Al-4V	GMAW, GTAW, PAW	[60-62]
Monel K500 & ERNiCu-7 (FM60)	GMAW	[63]
Pure titanium & 1080 (Pure Aluminum)	GTAW	[64]
Ti-35Al, Ti-45Al, Ti-55Al	GTAW	[65]
ER-NiCrMo-3	GMAW	[66]
HASTELLOY X	GTAW	[67]

### 1.1.1 GTAW-based WAAM

Gas Tungsten Arc welding (GTAW) or Tungsten Inert Gas arc welding (TIG) refers to an arc welding technique where an electric arc is formed inside an inert gas atmosphere between a non-consumable Tungsten electrode and the workpiece [68]. When TIG welding is manual, welder uses welding rods as the filler metal. As shown in Figure 1.1, for automatic TIG used in GTAW-based WAAM, a wire feeder system with a wire spool has to be applied.

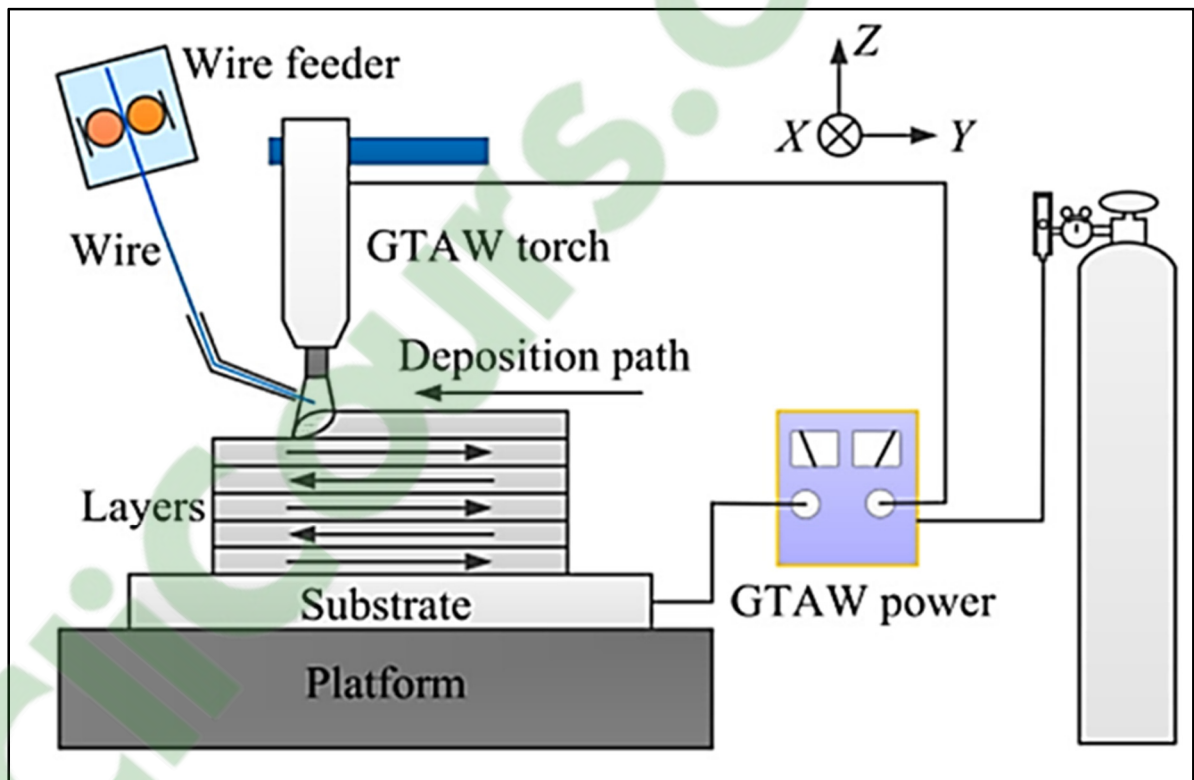


Figure 1.1 Schematic of GTAW-based WAAM.  
Taken from Xiong et al. (2019, p. 2129)

During TIG welding, the filler metal must be in front of the arc. Therefore, as shown in Figure 1.2a, when the torch direction changes, actuated by the 6-axis movement unit, GTAW based-WAAM needs a system for changing the position of filler metal to the fore of the arc.

When using the traditional TIG welding technique for WAAM, the droplet transfer mode is sensitive to the angle between the wire and workpiece [48, 69]. Figure 1.2b shows an

innovation at GTAW. It is named the TOPTIG process and is introduced by Lincoln Electric [70]. As shown in Figure 1.2c, in the TOPTIG process, the wire feeder system is integrated into the torch. This design eliminates many of the limitations of Traditional TIG and provides greater flexibility during welding. In the TOPTIG process, the molten transfer consists in a continuous liquid transfer mode [48]. The advantages of the liquid transfer mode include a high deposition rate at maximum speed, a continuous and regular weld, and a greatly reduced risk of contact of the welding wire with the tungsten electrode [69].

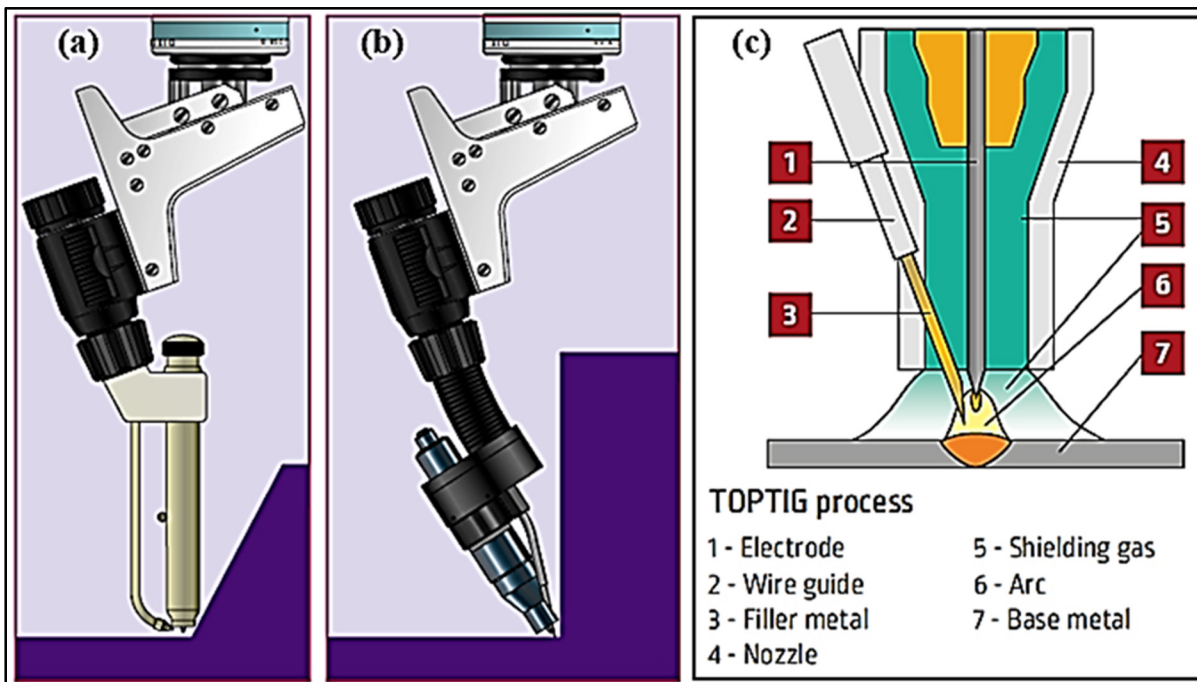


Figure 1.2 Conventional TIG torch (a), TOPTIG torch (b, c).  
Taken from Air Liquide Welding (2008, p. 3)<sup>1</sup> and Lincoln Electric<sup>2</sup>

### 1.1.2 PAW-based WAAM

The plasma arc welding (PAW) process is similar to Gas Tungsten Arc Welding (GTAW), with the difference that PAW brings a much higher energy density at the arc, and produces

<sup>1</sup><http://files.engineering.com/download.aspx?folder=f9d6f4ee-cb78-4cc3-8ded984cb16af90c&file=TOPTIG.pdf>

<sup>2</sup><https://www.lincolnelectric.com/en-gb/automation/Pages/welding-processes-toptig.aspx>

much higher gas velocity and momentum by constraining the arc to flow through a nozzle [71]. The arc energy density in plasma welding can be up to three times that of the GTAW, resulting in less weld distortion and smaller bead welds with higher travel speeds [72]. When using PAW for additive manufacturing, increasing the welding speed can lead to increased production speed. Therefore, it is possible to produce parts with a thinner wall. But the humping phenomenon should not be neglected at high travel speeds [73, 74]. Figure 1.3 shows a schematic of PAW-based WAAM.

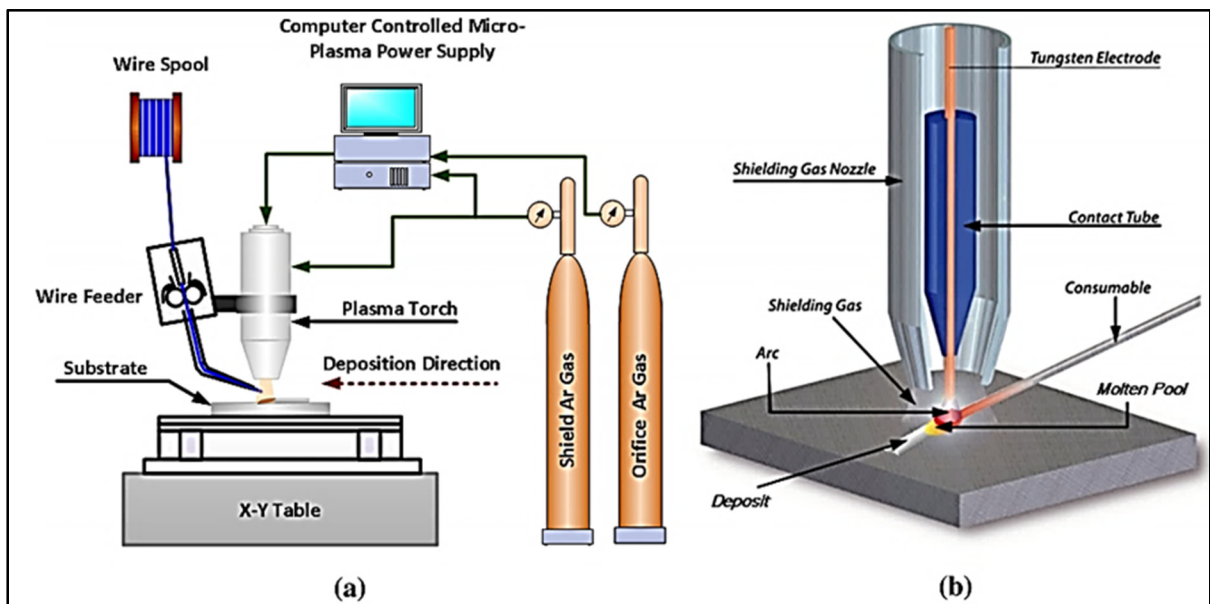


Figure 1.3 Schematic of PAW-based WAAM.  
Taken from S. Jhavar et al. (2016, p. 1804)

Same as for GTAW, in PAW welding, the filler metal must always be in front of the arc, which becomes a problem during the WAAM process because it is necessary to change the direction of the arc. To solve this problem, as shown in Figure 1.4a, a system that simultaneously changes the direction of the arc and the filler metal has to be used. Another method used to eliminate directional sensitivity during PAW-based WAAM is to use three PAW torches arranged around a central wire feeder. This method is known as Plasma Arc Welding (PAW) Print 3-Dimensional (PP3D) [75]. Figure 1.4b shows a schematic of PP3D.

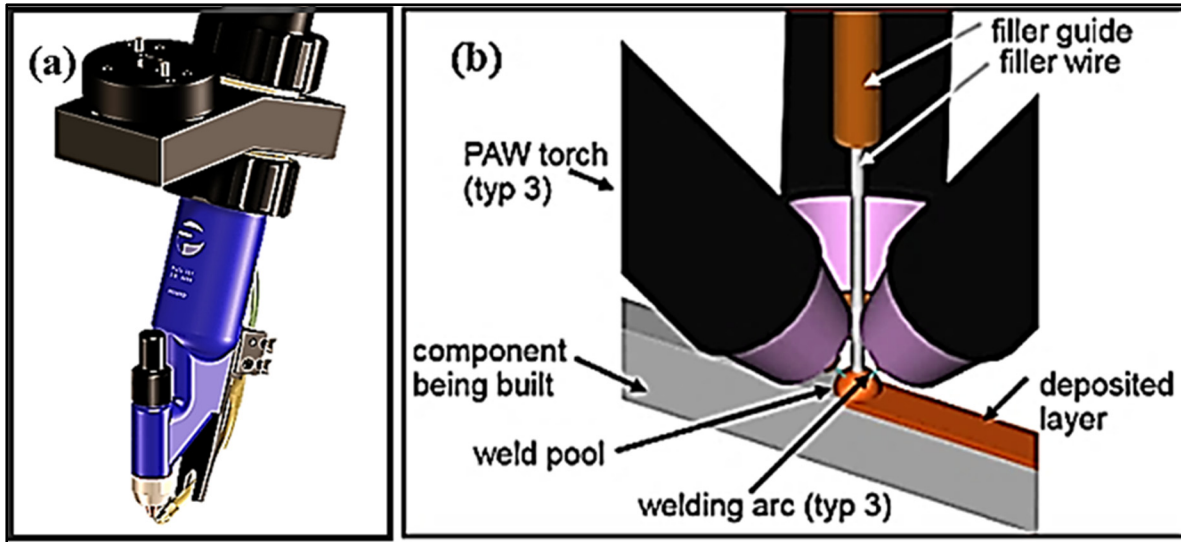


Figure 1.4 Plasma welding robotic torch with wire feeder (a), Plasma Arc Welding (PAW) Print 3-Dimensional (PP3D) (b).

Taken from N. Huft (2019, p. 2) and Aircraft Plasma Equipment<sup>3</sup>

### 1.1.3 GMAW-based WAAM

Gas Metal Arc Welding (GMAW) is a process in which the electrical arc is the heat source and is formed between a consumable electrode and the workpiece. An inert or active gas stream protects the arc and weld pool during welding [76]. GMAW-based WAAM is very suitable for the production of large parts in a short time due to higher deposition rates [77]. Figure 1.5 shows a schematic of GMAW-based WAAM.

<sup>3</sup> <http://www.aircraftplasma.com/welding-gun.html>

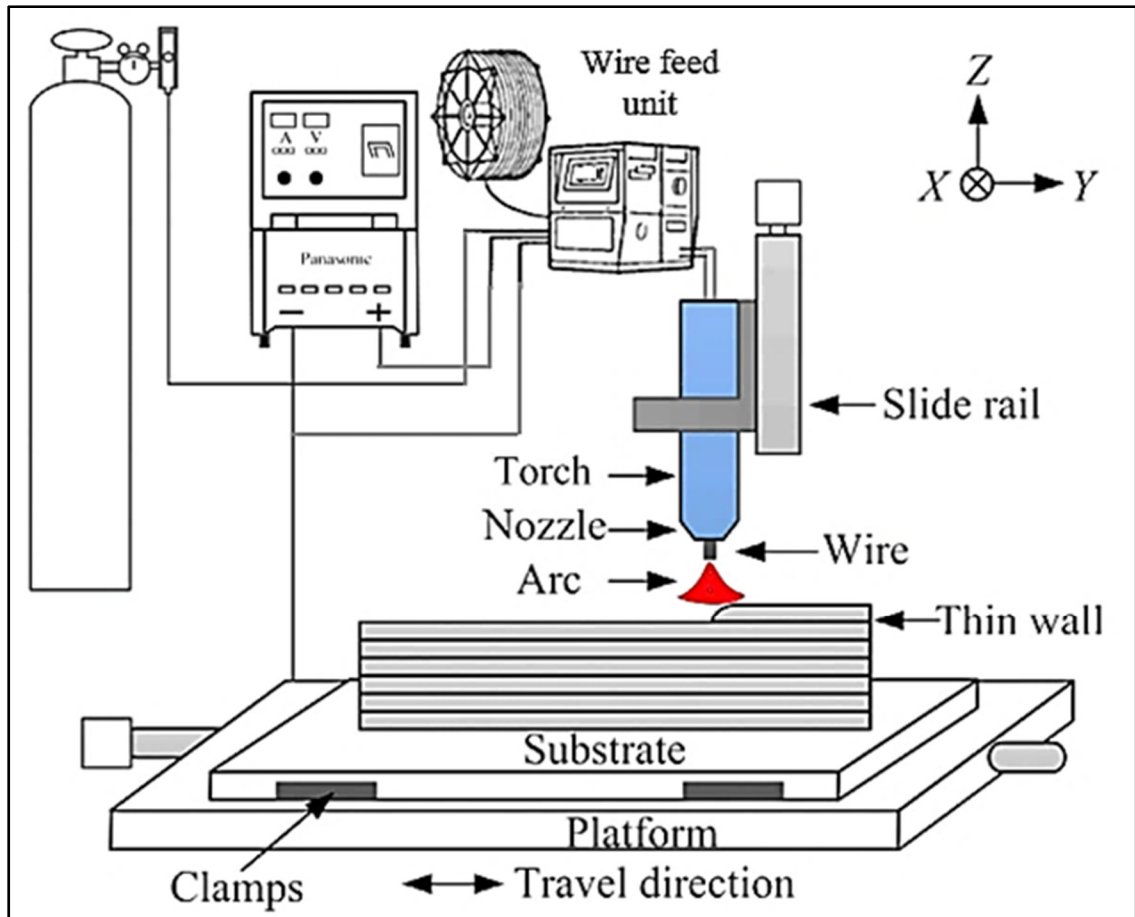


Figure 1.5 Schematic of GMAW-based WAAM.  
Taken from J. Xiong et al. (2018, p. 129)

The dynamic characteristics of the arc and the droplet transfer modes are two important and influential factors on GMAW-based WAAM [78]. The dynamic characteristics of the arc originate from the shape and properties of the weld current wave and voltage wave during the welding process [79]. GMAW has four main modes of droplet transfer: globular mode, short-circuit mode, spray mode, and pulsed-spray mode. Cold Metal Transfer (CMT) is a modified pulsed gas metal arc welding (GMAW-P) introduced by Fronius. CMT is especially considered in GMAW-based WAAM because of its excellent welding performance, low heat input, and virtually spatter-free mode [12, 78, 80, 81].

## **1.2 The challenges of manufacturing by WAAM**

### **1.2.1 Surface roughness**

One of the issues of the pieces produced by WAAM is high initial surface roughness. This problem causes a restriction on the use of components in highly stressed and periodically loaded areas, and thus, after the WAAM process, surface machining is often necessary [82, 83].

The WAAM process parameters, such as heat input, travel speed, layer height, and scan strategy, affect surface roughness [35]. Yehorov et al. [84] showed that the surface roughness of the Al-Mg alloy walls made by GMAW-based WAAM is dependent on a specific range of welding speed. They explained that if the travel speed is low, the surface roughness, and the production cost will increase. On the other hand, if the travel speed is very high, the humps, and valleys form over the layers.

Dinovitzer et al. [67] investigated GTAW-based WAAM parameters on bead geometry and microstructure. The specimens were Hastelloy X alloy. They have found that welding speed and current have the most effect on heat input. Rising welding speed or reducing current have a declining effect on the penetration depth, and growing effect on the roughness of specimens. Xiong et al. [40] discussed the influences of process parameters on surface roughness of H08Mn2Si thin-walled parts in GMAW-based WAAM. Based on their finding, the surface roughness can be reformed by decreasing the inter-layer temperature. If wire feed speed (WFS) and interlayer temperature are considered constant, increasing the travel speed until 0.42 (m/min) will improve the surface quality, but higher travel speed will extend surface roughness due to arc instability.

### **1.2.2 Microstructure and gas porosity**

Quick heating, and subsequently, fast cooling is the main cause of the inhomogeneous microstructure of the WAAM products. The columnar dendritic grains are the principal factor of the heterogeneous characteristics, therefore the mechanical properties of the WAAM pieces

vary in the vertical and horizontal directions. Changing the grain structure from columnar to equiaxed dendritic grains during WAAM is very suitable to achieve homogeneous mechanical properties.

Guo et al. [85] studied the microstructure and mechanical properties of the GTAW-based WAAM AZ80M. Their results show a heterogeneous structure along the deposition direction. The upper zone of the specimen was shaped with many equiaxed dendritic grains, while in the lower layers columnar dendritic grains were formed. Mechanical properties in the horizontal and vertical directions were different.

Birmingham et al. [86] examined the effect of growth restricting solutes and nucleating particles on the columnar to equiaxed transition (CET) during GTAW-based WAAM of titanium alloys. Their findings indicate that grain refining solute only reduces the width of the columnar grains and does not affect the production of equiaxed grains. The nucleating particles not only refine the columnar grain size but also produce an equiaxed zone at the top of the layer. This means that during the solidification process, the temperature gradients are decreased by the presence of nucleating particles in the melting pool, and this authorizes constitutional supercooling and equiaxed grain nucleation.

Lin et al. [62] studied the effect of heat input on the microstructure of Ti-6Al-4V thin walls made by PAW-based WAAM. They concluded that decreasing heat input of each bead and using pulsed current causes a refined microstructure in the thin wall.

Marinelli et al. [87] chose two different unalloyed tantalum wires for GTAW-based WAAM. They found that the anisotropic microstructures for their specimens had grown large columnar grains from the substrate to the height of the deposit. The content of oxygen has a direct effect on the diameter of porosities and increase the microhardness.

Cong et al. [88] focused on the effect of arc mode in CMT process on porosity of Al-6.3%Cu alloy. They used different droplet transfer modes of cold metal transfer (CMT) and made specimens by WAAM. They found that the variable polarity CMT (VP-CMT) arc process eliminated the porosity efficiently and concluded that the critical details are a low heat input, a fine equiaxed grain structure and an effective oxide cleaning of the filler wire.

Guo et al. [89] studied the effect of pulse frequency on grain refinement for AZ31 magnesium alloy components made by GTAW-based WAAM. They used different pulse frequencies and

found that a certain amount of pulse frequencies (5-10 Hz) has the maximum influence on making fine grains and improving tensile properties.

Using the pulse current and variable polarity can transfer the columnar grain into the equiaxed grain and refine the grain size. As shown in Figure 1.6, this kind of currents breaks the arms of columnar dendrites and increases the nuclei for equiaxed dendrites. In the equiaxed grain structure, the gas porosities are fine because their mobility is limited, therefore they cannot attach together and create large pores [90].

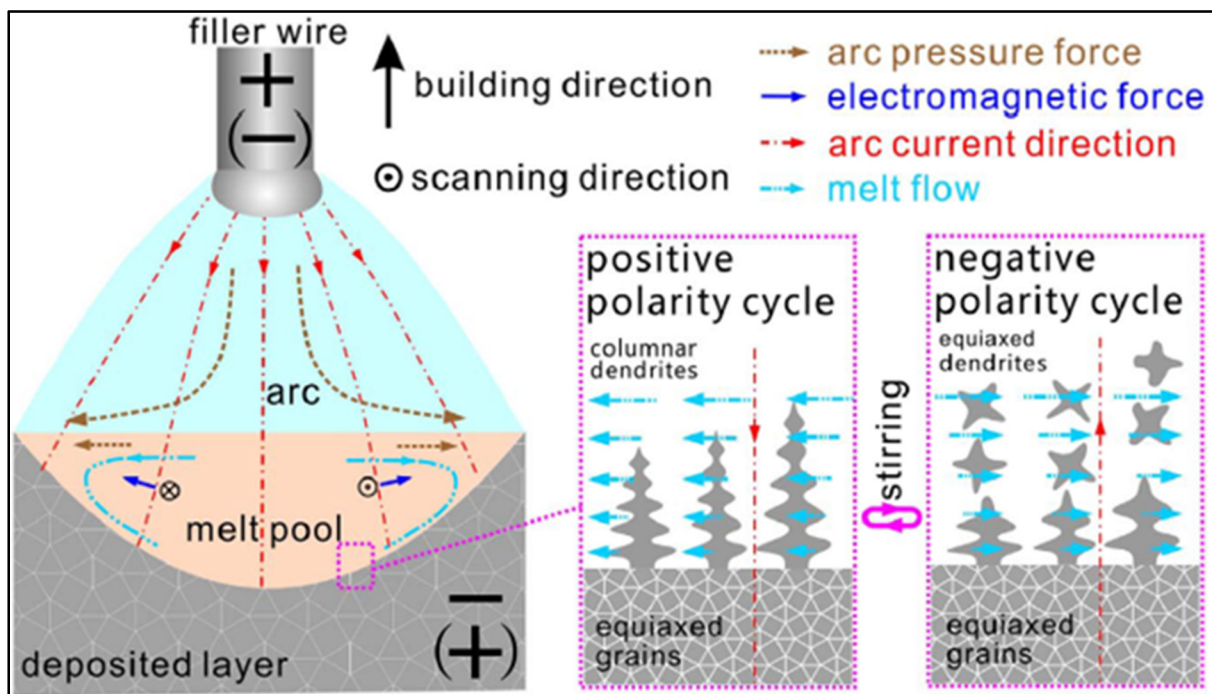


Figure 1.6 The effects of variable polarity arc on the melt pool and the solidification process.  
Taken from C. Zhang et al. (2018, p. 423)

Zhang et al. [91] optimized the microstructure and homogenized the grain distribution using a vibration aging system. Figure 1.7 shows the results of their research. It shows that the workpiece vibration breaks the dendrite arms and refines the grains by creating the new nuclei.

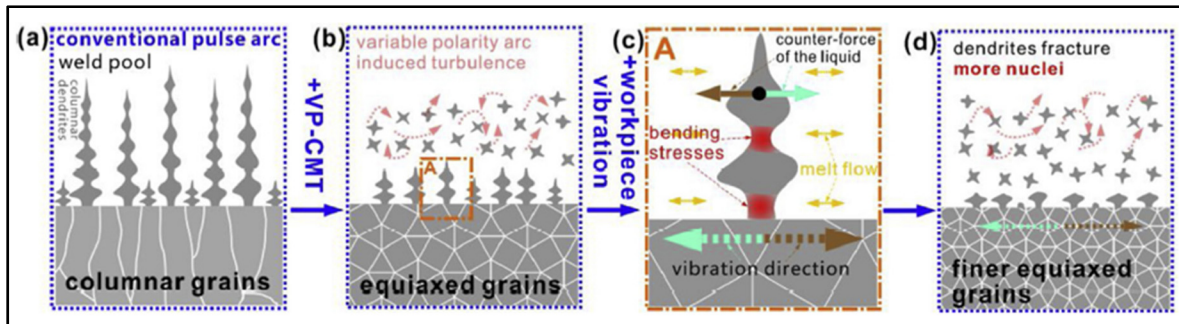


Figure 1.7 Performance of workpiece vibration for grain refinement; (a) the illustration of the weld pool when using conventional pulse arc; (b) the illustration of the weld pool when using VP-CMT; (c) enlarged illustration of part A in b and showing the effect of bending stress due to vibration on dendritic arms breakage; (d) the illustration of the weld pool after vibration stabilization.

Taken from C. Zhang et al. (2019, p. 90)

### 1.2.3 Residual stress and distortion

The thermal cycle of WAAM consists of three steps. Step one is the rapid heating and melting of the feedstock, step two is the solidification of metal deposition by a high cooling rate, and step three is the re-melting of previously solidified underlying layers by new layer deposition [92]. The strain in the deposited layer is due to thermal expansion and contraction of the material. There will always be a strain owing to the contraction in the deposited layer after step two, and that is how residual stress is generated in the deposited layer. The layer is attached to the substrate or previous layer, and the compressive plastic strain is not possible. Therefore, tensile residual stress will be created in the deposited layer. This problem will be more complex considering the strain transformation phases after step three [35]. As a model that is shown in Figure 1.8, if a wall is deposited by WAAM on a clamped substrate, as illustrated in Figure 1.8a, there are uniform residual tensile stresses across the height of the wall and uniform residual compressive stress across the substrate thickness in the longitudinal direction. Figure 1.8b depicts the distribution of residual stress after unclamping. The distribution of residual stress at wall height and substrate thickness is changed in the way that there is residual compressive stress at the top of the wall and residual tensile stress at the lower portion of the wall near to the surface of the substrate. As shown Figure 1.8c, the new distribution of residual stress induces distortion in the wall and substrate [93-95].

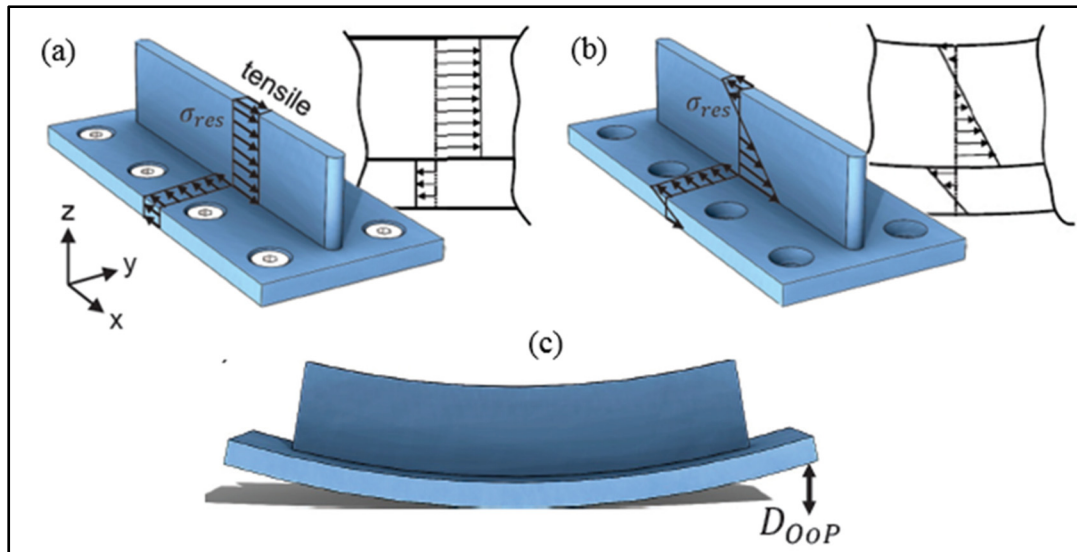


Figure 1.8 Distribution of residual stress before unclamping (a), distribution of residual stress after unclamping (b), distortion after unclamping (c).

Taken from M. Roy et al. (2016, p. 456)

Various ways have been proposed to reduce residual tensile stress. For example, compressive stress can be generated on the surface, which eliminates part of the residual tensile stress by peening. Although peening improves the surface quality and increases the fatigue life of the component, peening can-not have a significant effect on the amount of residual tensile stress due to the low depth of compressive stress induced in the component [96, 97].

Another way to reduce residual stress is to use high-pressure rolling (Figure 1.9). The rolling can be carried out either independently at room temperature or immediately after the deposition head. The effect of this method on reducing the residual tensile stress is much more effective than peening [94, 98].

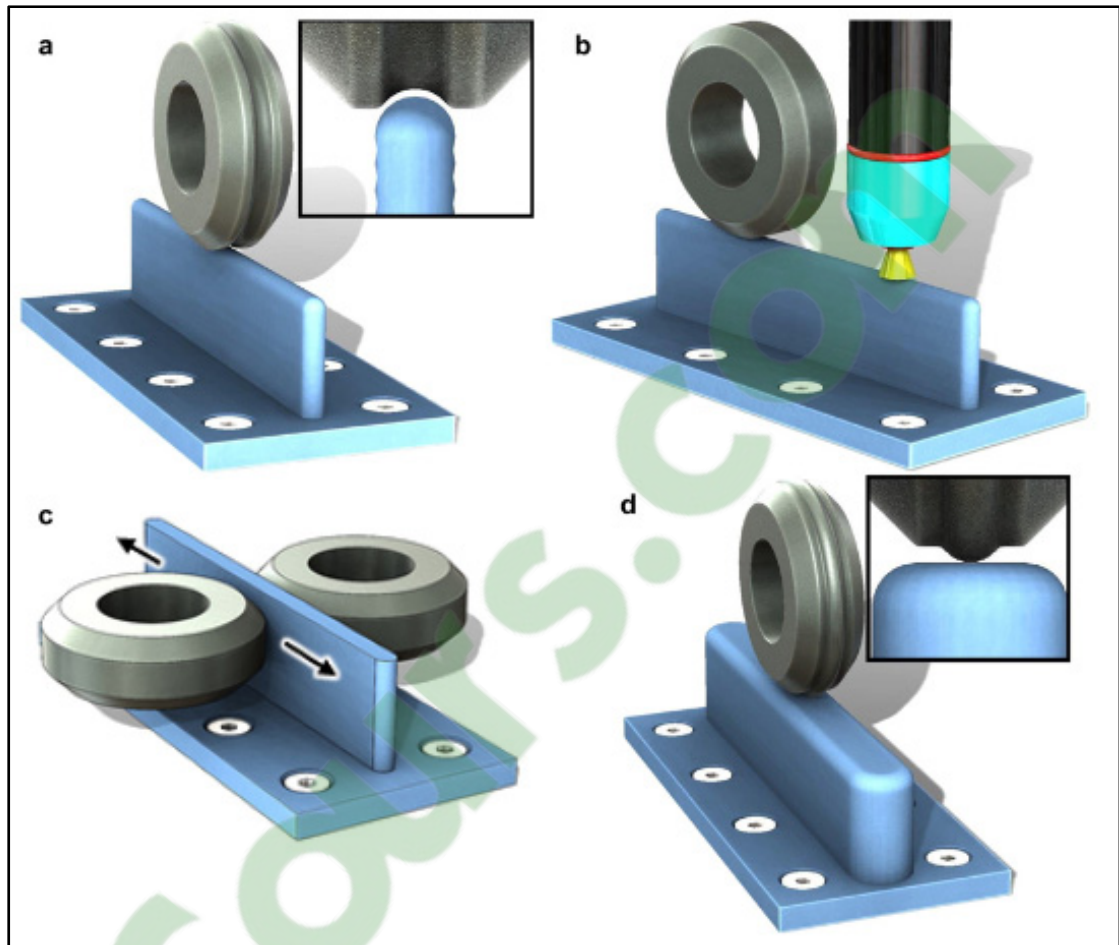


Figure 1.9 Schematic diagram of the main rolling methods: (a) vertical with a profiled roller; (b) in-situ rolling; (c) pinch rolling (d) rolling with an inverted profiled roller for thick sections and intersections.

Taken from P. A. Colegrove et al. (2017, p. 112)



## CHAPTER 2

### FEASIBILITY STUDY OF ALUMINUM DEPOSITION BY ROBOTIC MIG WELDING PROCESS <sup>4</sup>

#### Abstract

Among the various processes of additive manufacturing, the wire arc additive manufacturing process (WAAM) is quite attractive due to its high deposition rate. Although the surface finish of WAAM requires generally machining due to its roughness, it is not significant against its productivity and its low costs. In this study, WAAM is based on the deposition of layer upon layer in which each layer is a bead of metal inert gas (MIG) welding. To make a part, the welder robotic arm was used for torch movement. In recent years, the production of aluminum components with WAAM process has been progressively more and more interested by various industries due to its advantages. In most of the past researches, cold metal transfer (CMT) was used for this purpose. However, in this research, the conventional pulsed spray metal transfer mode was utilized in order to study the feasibility of applying this process to WAAM of 4043 aluminum alloy. Various welding parameters were applied to build walls using ER4043 as filler material and 6061-T6 as substrate. Then, wall quality was investigated in terms of porosity, roughness and effective width. The interaction between layers was also studied in terms of microstructures and micro-hardness at different points in the walls.

Keywords: Aluminum deposition, Mechanical and metallurgical properties, MIG welding, Porosity, Roughness, Wire arc additive manufacturing.

---

<sup>4</sup> This chapter has been presented at CanWeld Conference 2018 (Winnipeg, MB, Canada, Sept. 12-13, 2018).

## 2.1 Introduction

Additive manufacturing (AM) processes are methods for building three-dimensional (3D) components by adding layer upon layer of material [35]. Due to the fact that various types of materials (metals - polymers - ceramics) could be processed by AM, it has a bright future in the industry. Moreover, AM has created great attractions for the industry by reducing production time and cost and improving the buy-to-fly (BTF) ratio [99, 100].

According to ISO/ASTM 52900:2015(E), AM processes are divided into two categories, namely Directed Energy Deposition (DED) and Powder Bed Fusion (PBF) [101]. Wire-arc additive manufacturing (WAAM) is a wire-based DED process in which the wire is used as the feedstock material and the electrical arc is used as the heat source [102]. WAAM is divided into several categories based on the source of heat generation, such as Gas Metal Arc Welding (GMAW), Tungsten Electrode Welding (GTAW) and Plasma Welding (PAW) processes [40]. The selection of welding technology is driven by the type of request. For example, to carry out a fast process with a high deposition rate, GMAW is preferred to other welding technologies [103]. There are four main metal transfer modes for GMAW: globular, short-circuiting, spray and pulse-spray. Of course, to reduce the amount of heat input, more advanced transfer modes such as Cold Metal Transfer (CMT) and Surface Tension Transfer (STT) have been developed. The basis of these modes could be assumed to be an optimized mode of short-circuiting and pulse-spray [104]. In this research, the objective was to perform WAAM of 4043 aluminum alloy using adjusted parameters of pulse-spray metal transfer (GMAW-P).

The waveform of GMAW-P is shown in Figure 2.1. The primary parameters in pulse-spray metal transfer (GMAW-P) are peak current, background current, the peak current duration, background current duration, pulsing frequency and load duty cycle [105, 106].

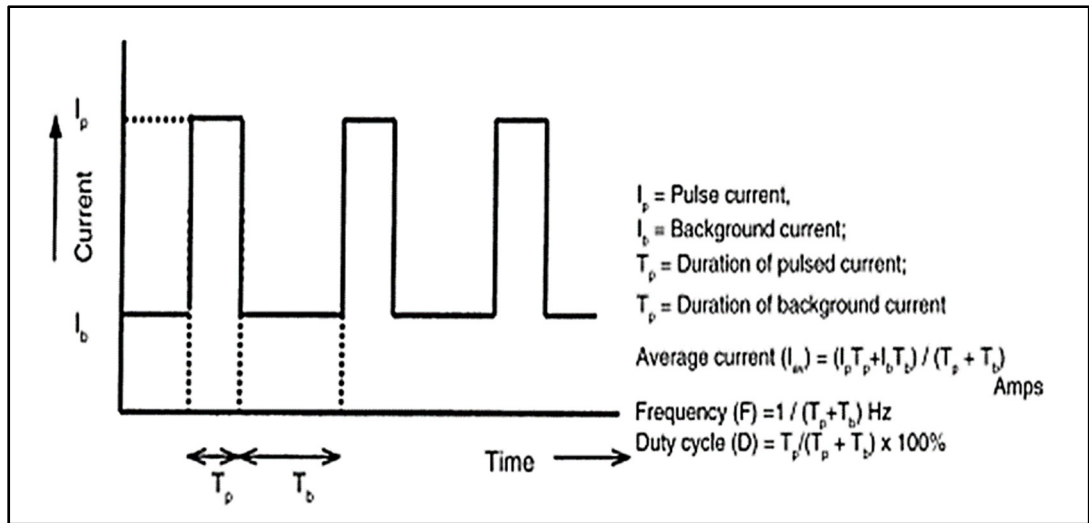


Figure 2.1 Schematic of a current–time diagram during pulse-spray welding.  
 Taken from P. Palani and N. Murugan (2006, p. 3)

Table 2-1 Important parameters affecting the performance of GMAW-P  
 Taken from P. Praveen and P. Yarlagadda (2005, p. 1112)

Parameters	Influences
Peak current	Penetration Molten metal droplet detachment
Peak time	Number of droplets detached per pulse
Base current	Maintains the arc Molten metal droplet detachment Temperature of transferred metal Fluidity
Mean current	Metal transfer mode Heat input to the material
Pulse duration	Number of droplets detached per pulse Must be greater than a critical value Influences drop size
Welding speed	Must produce spray mode of metal transfer Penetration Metal transfer mode Heat Input to the material
Wire size	Penetration Porosity
Wire feed rate	Wetting in weld bead Penetration Weld bead shape

The effect of each parameter on the performance of GMAW-P is summarized in Table 2.1. Adjusting GMAW-P parameters is generally time-consuming by trial and error, to achieve controlled transfer during pulse welding, it is essential that the wire feed rate is balanced by burn rate. This means achieving one drop per pulse (ODPP) all the time, which involves constant control of all the pulse parameters [107, 108]. There is a class of GMAW-P supplies, called synergic power supplies. In this class, the power supply and the wire-feeder are directly linked in such a way that according to the settings of a range of wire feed speed, the amount of mean current is unchanged during the welding process, generating a stable arc [109, 110].

Although most of the research on WAAM has been done on titanium and steel alloys, the increasing use of aluminum alloys in industries, especially in the transport and aerospace industry, has drawn the attention of researchers to the use of aluminum alloys in WAAM. One of the major problems in aluminum welding is hydrogen gas porosity. The reason for this is the high solubility and high dissolution rate under the arc of hydrogen in the aluminum liquid pool. Upon solidification, the hydrogen is rejected in the liquid at the solid-liquid interface because its solubility in the solid phase is much lower. The excess hydrogen in the liquid results in the germination of hydrogen bubbles which may grow and coalesce and form macroscopic porosities in the solidified alloy as shown in Figure 2.2 [111]. The alloying elements are effective in the formation and size of the porosity in aluminum. Gu et al. [112] reported that, during eutectic solidification for a heat-treated aluminum alloy, pores consist of inter-dendritic spaces and they remain motionless and do not float, so they do not expand. But during heat treatment, a large number of some pores combine and form large pores. In non-heat treatable alloys, the presence of volatile elements such as Mg are effective in the formation of pores.

The microstructure of the aluminum pieces always involves a competitive correlation between dendrite growth and pore nucleation rate [12, 113]. Three important factors that define the dendritic morphology are dendrite arm length, aspect ratio, and arm spacing. By reducing the welding heat input (HI), these three factors were improved, which modified the dendritic structure from a very coarse structure to a fine equiaxed structure [114]. In the welding, due to the fact that the weld pool generally solidifies under high thermal gradient, the formation of a columnar dendritic structure throughout the welding metal is expected [115]. Increasing the wire feed speed (WFS) in GMAW may cause a negative temperature gradient in front of the

melt, which reduces the growth of columnar dendrites and creates equiaxed structures [116]. Researches showed also that when applying variable polarity methods in welding, the generated pulses break the secondary arms of the dendrites, and these broken arms will be the nucleation site of the new dendrites. In the other words, when applying the pulsed method in welding, the dendritic structure will be more equiaxed (Figure 2.3) [90, 117]. Considering this, it could be supposed that this result also would happen in the weld structure by applying a pulsed current (GMAW-P). In the columnar dendritic structure, the gas porosities have a great possibility of movement between the dendritic arms during solidification, which causes the fine-pores to join together and make big-pores. But in the equiaxed dendritic structure, the fine-pores' movement become limited and big-pores are not created easily [12]. Therefore, the welding methods can allow the modification of the thermal profile, which can result in fine equiaxed microstructure and the elimination of porosity.

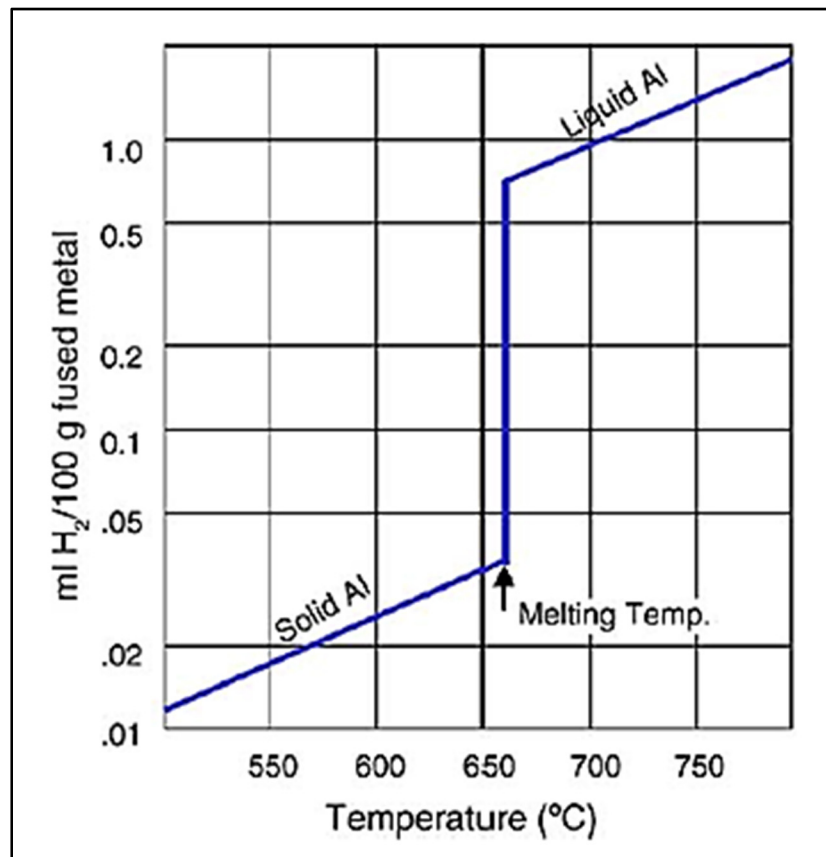


Figure 2.2 Solubility of hydrogen in aluminum at various temperatures.  
Taken from P. Praveen and P. Yarlagadda (2005, p. 1108)

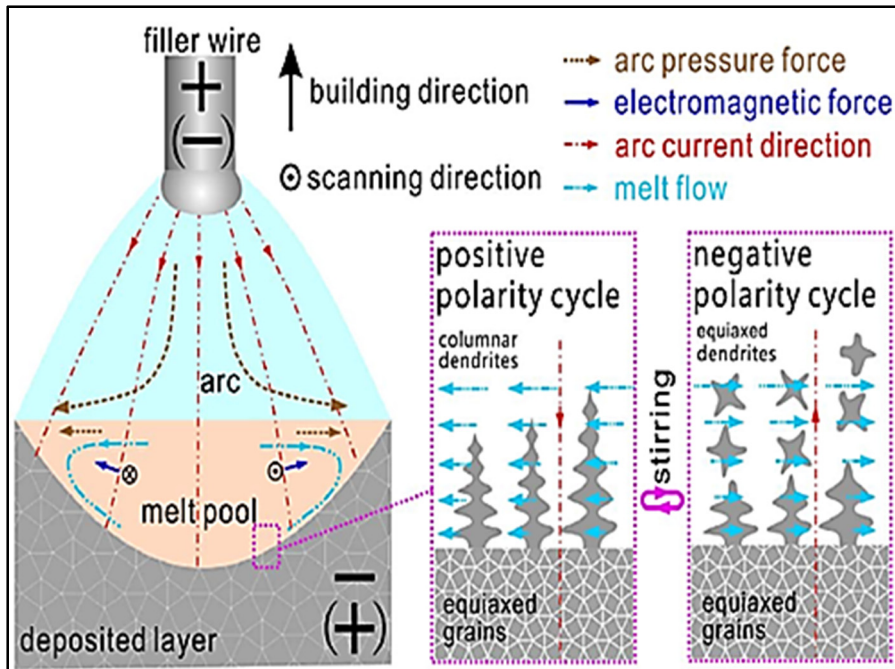


Figure 2.3 The effects of variable polarity arc on the melt pool and the solidification process.

Taken from C. Zhang et al. (2018, p. 423)

In this paper, Pulsed Synergic Mode (GMAW-P) process was used to make walls by AM method. Different welding parameter such as pulse profiles, powers, wire feeding speeds, welding speeds were used to study the feasibility of the process. Surface roughness, effective wall thickness, porosity, hardness and microstructures in parts were evaluated to justify the quality of parts.

## 2.2 Experimental description

In this study, ER4043 wire with a diameter of 1.2 (mm) was used as a MIG welding wire, and aluminum plaque 6061 with a thickness of 9.8 (mm) as a substrate. Their chemical compositions and mechanical properties are listed in Tables 2.2 and 2.3. The power source was a Fronius TransPuls Synergic 4000 (Figure 2.4.a), and a YASKAWA MOTOMAN arm (Figure 2.4.b) provided processing movement. In synergic power supplies, the welding machine is set automatically according to the conditions of one drop per pulse (ODPP). When

using this class of machines for GMAW-P, the main parameters are automatically set by adjusting the wire feed speed (WFS), travel speed (TS), and contact tip-to-work distance (CTWD). Definitely, in the WFS, TS, and CTWD settings, it is necessary to have the precision and skill to achieve the most stable arc and the best weld bead.

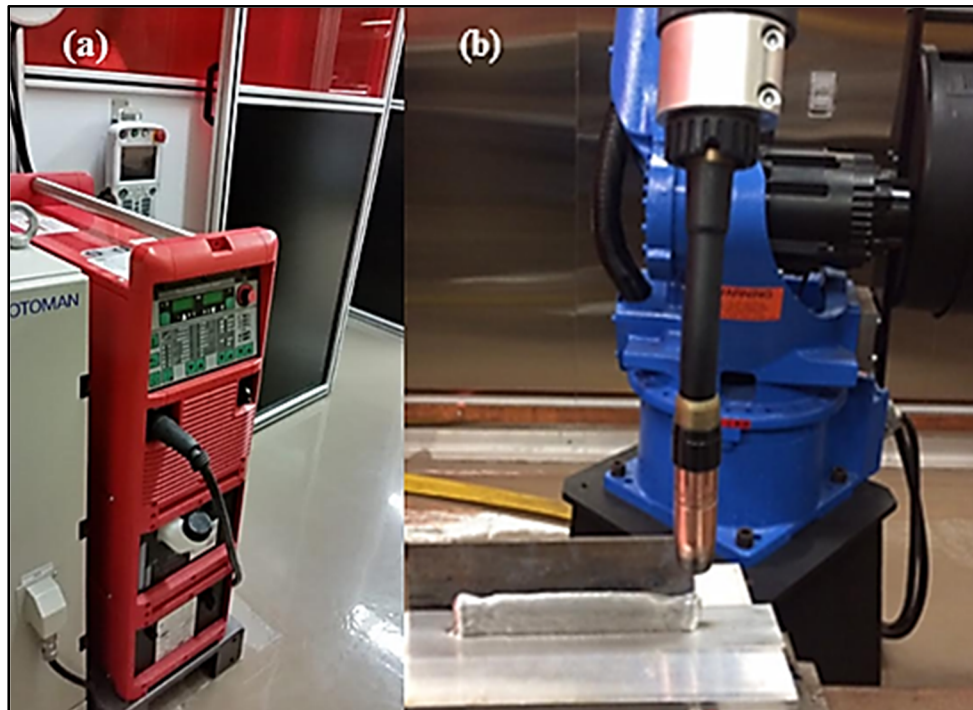


Figure 2.4 Fronius TransPuls Synergic 4000, (b) YASKAWA MOTOMAN arm.

Table 2-2 Chemical composition of ER4043 and 6061 alloy (WT %)

Elements	Al	Si	Mg	Fe	Cu	Mn	Zn	Ti	Be	Cr
ER4043	Balance	4.5- 6.0	0.05 max	0.8 max	0.3 max	0.05 max	0.1 max	0.2 max	0.0003	-
6061	Balance	0.4- 0.8	0.8- 1.2	0.7 max	0.15- 0.4	0.15 max	0.25 max	0.15 max	-	0.04- 0.35

In Pulsed Synergic Mode (GMAW-P), there is another parameter for pulse correction called Dynamic/Pulse Correction (DYN) and it is used to change the frequency value. In Fronius

TransPuls Synergic 4000, the DYN range is adjustable from -5% to +5%. Figure 2.5 shows an example of DYN effects. A negative DYN value results in more pulse per second which reduces pulse current time; this results in smaller droplet sizes carrying less energy. For the positive DYN value, it is the complete opposite: lower frequency, more time spent in the current boost phase, resulting in a fewer droplet detachment, but larger droplets carrying more energy.

Table 2-3 Mechanical properties of ER4043

Ultimate Tensile Strength	Yield Strength	Percent Elongation in 2"
21,000 - 33,000 psi (144-227 MPa)	10,000 - 27,500 psi (69-190 MPa)	5 - 12%

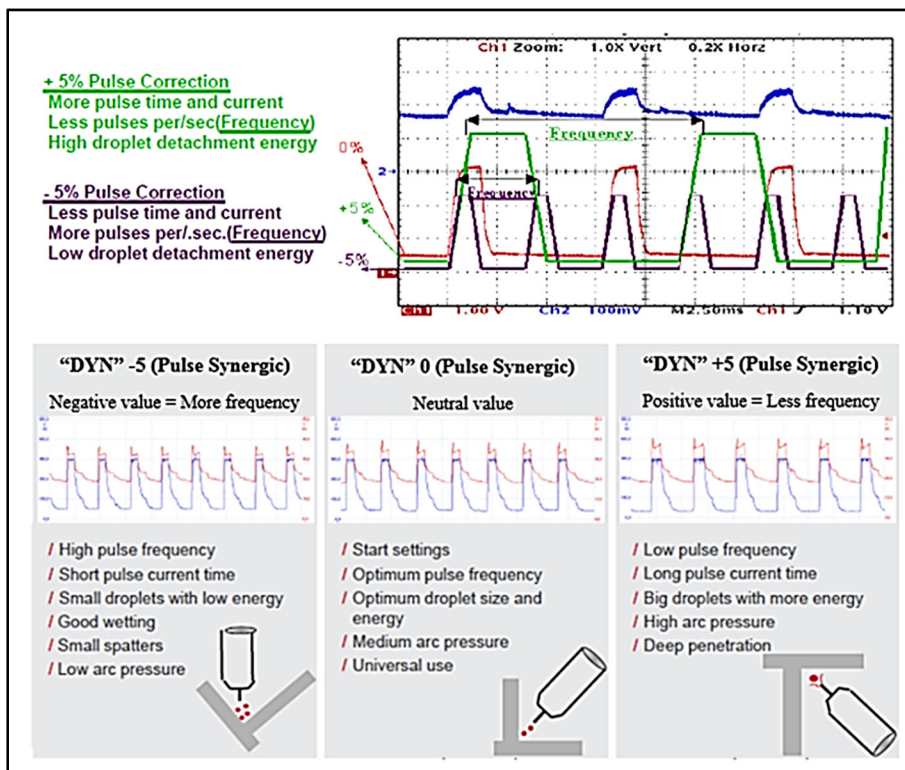


Figure 2.5 Effect of DYN on weld droplet.  
 Taken from Fronius Quick Reference Cards<sup>5</sup>

<sup>5</sup><http://www.robainindustries.com/wp-content/uploads/2016/06/Fronius-TS-Quick-Reference-sheet.pdf>

In this research, in the first test, zero value was considered as the value for DYN and 20 (ipm) for TS. Then, in order to find a stable arc with trial and error, different values were tried for WFS and CTWD in order to find final values for them. For the second test, the amount of DYN was changed to -5%, and for the third test, the amount of DYN was changed to +5%. To get an arc stable, the amounts of TS, WFS and CTWD were changed slightly for the second and third tests in comparison to the first test.

The obtained values for these three tests are shown in Table 2.4. The schematic of the construction of the walls is presented in Figure 2.6.a. The pictures of the walls made in this research are shown in Figure 2.6.b. The walls were examined for porosity, microstructure and micro-hardness where the tested areas are depicted in Figure 2.6.c. For porosity analysis, the as-polished photographs with 50× and 100× magnifications of the test samples were examined by using the ImageJ software.

Table 2-4 Welding parameters of the tests

	DYN (%)	TS (m/min) (ipm)	WFS (m/min) (ipm)	CTWD (mm)	Stick-out (mm)	Ar-Flow (cfh) (Ar≥99.9996)
Test 1	0	0.51 (20)	7.2-7.5 (285.5-295.3)	17-18.8	15	35
Test 2	-5	0.46 (18)	8.9-9.1 (350.4-358.3)	18-19.2	16.5	35
Test 3	+5	0.61 (24)	7.3-7.6 (287.4-299.2)	19-19.7	17.5	35

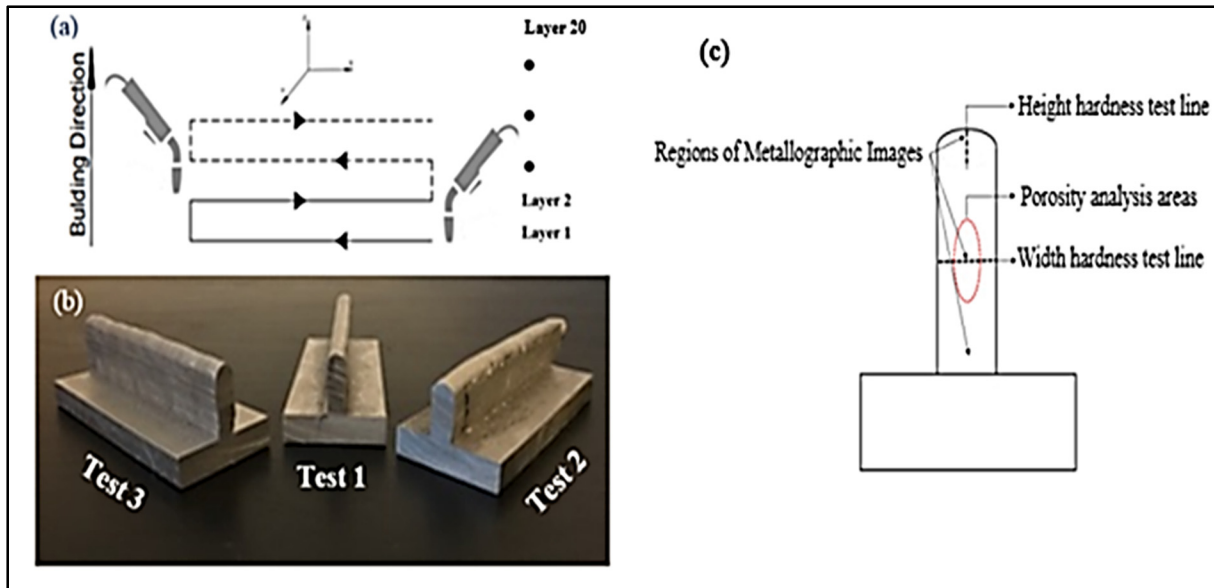


Figure 2.6 (a) Construction process of the wall by the welder robotic arm, (b) the images of the three walls made, (c) tested areas and locations.

To do microhardness, after polishing and preparing the specimens, the microhardness tester FM (FUTURE-TECH) was set to a 50 (g) load that applied for 15 seconds. To investigate the dendritic microstructure, test samples were grinded by abrasive paper, and then polished and corroded. The etchant solution was a combination of 93 (ml) distilled H<sub>2</sub>O, 5 (g) NaF, and 2 (g) NaOH. The corrosion time was 7 seconds. An optical microscope (OM) was used to observe microstructures.

### 2.3 Results and discussion

Figure 2.7 shows the stitched images of the 3 tests provided by the Olympus LEXT OLS4000 confocal microscope with a magnification of 50 $\times$ . In these pictures, height of each wall, penetration depths of every layer and distribution of porosities are clearly visible in all the tests. It was observed that the wall of Test 2 had a larger effective wall thickness (EWT) than the other two walls, and its surface waviness (SW) was higher too, which was caused by the higher amount of WFS and lower amount of TS in comparison to Test 1 and Test 3.

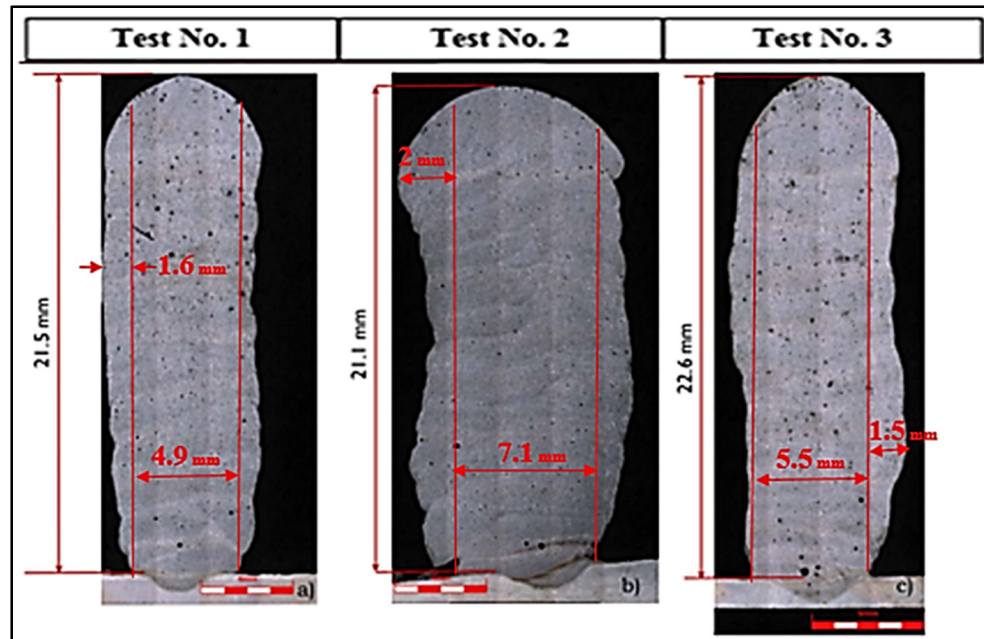


Figure 2.7 Stitched images of the tests and comparison of the walls in terms of EWT and SW values.

In Table 2.5, the percentage of total porosity areas (TPA) divided by the total tested surface area is presented. The porosity areas are assumed as the cross sections of the spheres on the surface of samples. The measurements were performed for each test sample in four areas randomly selected on the surface of test samples by ImageJ software, and the average value for each test sample is calculated at the bottom of each column.

Table 2-5 Total porosity areas over testing area in %

	[Total porosity areas/Testing area] %		
	Test 1	Test 2	Test 3
Area 1	1.632	0.840	1.356
Area 2	0.383	0.353	1.227
Area 3	1.034	0.244	0.616
Area 4	0.453	0.256	0.224
Average	0.875	0.423	0.856

According to Table 2.5, the average TPA for Test 2 is about half the TPA of Test 1 and Test 3. Consequently, it can be concluded that by changing negatively the value of DYN, i.e., increasing the frequency and decreasing the diameter of the droplets, the porosities in the structure of the weld bead decreases. However, the TPA of Test 1 and Test 3 are not much different, and the calculated average for the first test is close to the third test's average.

For a more accurate analysis of Area 1, the images of each test are magnified 50× (Figure 2.8). And, in order to present a more detailed analysis, the results are shown quantitatively in Table 2.6.

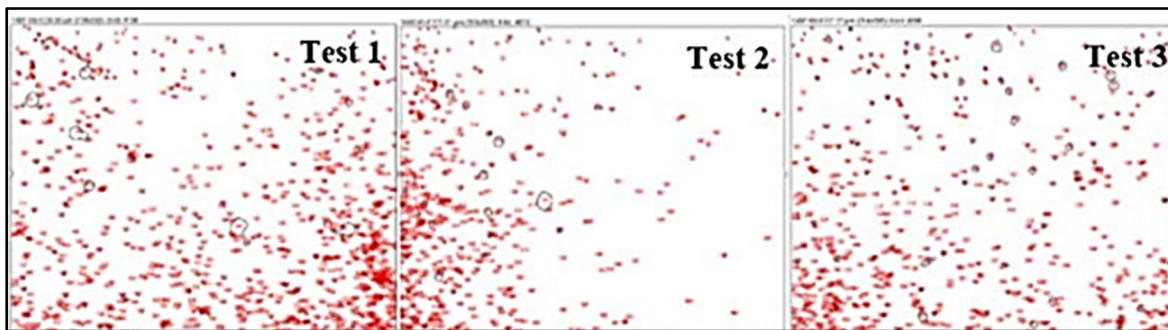


Figure 2.8 Analyzed images by ImageJ software for Area 1.

Table 2-6 Summary of images' analysis results of area 1 by ImageJ software

Area 1	Total number of porosities	Total Area ( $\mu\text{m}^2$ )	Average Size ( $\mu\text{m}^2$ )	Area%
Test 1	963	29994.29	31.147	1.632
Test 2	529	15457.57	29.220	0.84
Test 3	649	24932.76	38.417	1.356

Results in Table 2.6 shows that the average size of porosity in Test 3 is higher than the rest of the tests and that the average size of porosity in Test 2 is the lowest. In Figure 2.9, porosities have been grouped into 2 microns ranges and the porosity distribution of each group in Tests 1, 2, and 3 are expressed. It can be observed in this figure that in Test 2, not only the total number of porosities is lower compared to Tests 1 and 3, but also the percentage of smaller

porosity is higher than the others. This is another reason why the mechanical properties of Test 2 are better than in other tests. Figure 2.9 shows also that the percentage of large porosities in Test 3 is higher than in Test 1. Even though the total number of porosities in Test 3 is lower than in Test 1, it must be noted that big porosity is made by the combination of multiple smaller porosities during solidification. This proves that the total number of porosities might not be a valid criterion for the evaluation of mechanical properties.

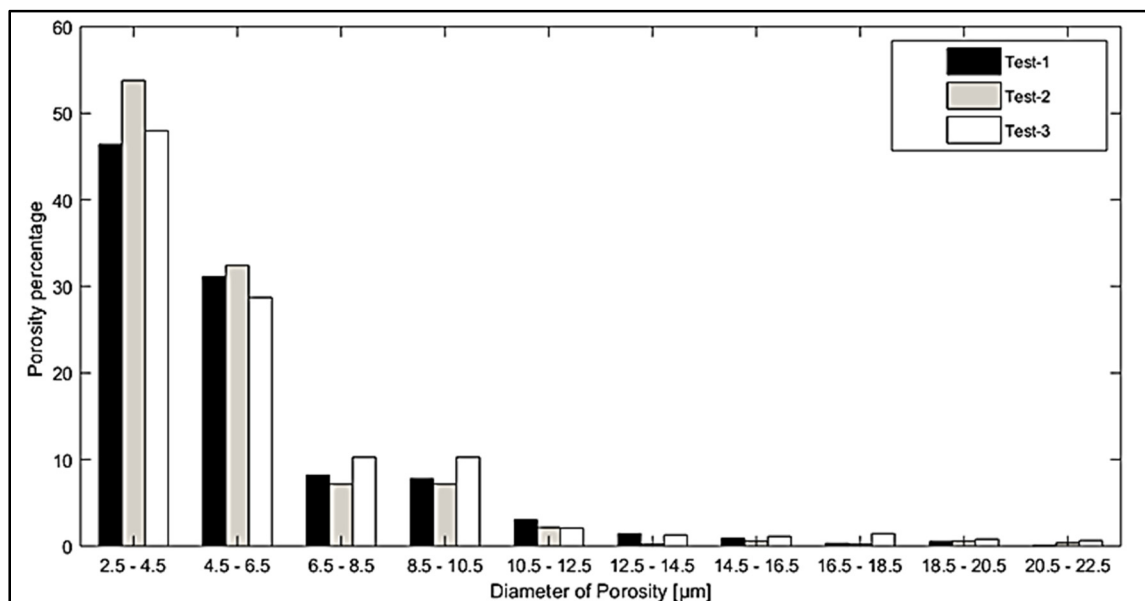


Figure 2.9 Porosity percentage.

From all this information, it is concluded that decreasing the DYN towards negative values, i.e. increasing the frequencies and decreasing the size of the droplets, causes smaller porosities in bead weld whose number is also lower. Vice versa, by increasing the DYN towards positive values, the frequencies decrease and droplets are bigger, even though it is possible that the total number of porosities become less in bead weld, and the tendency of forming bigger porosities increases.

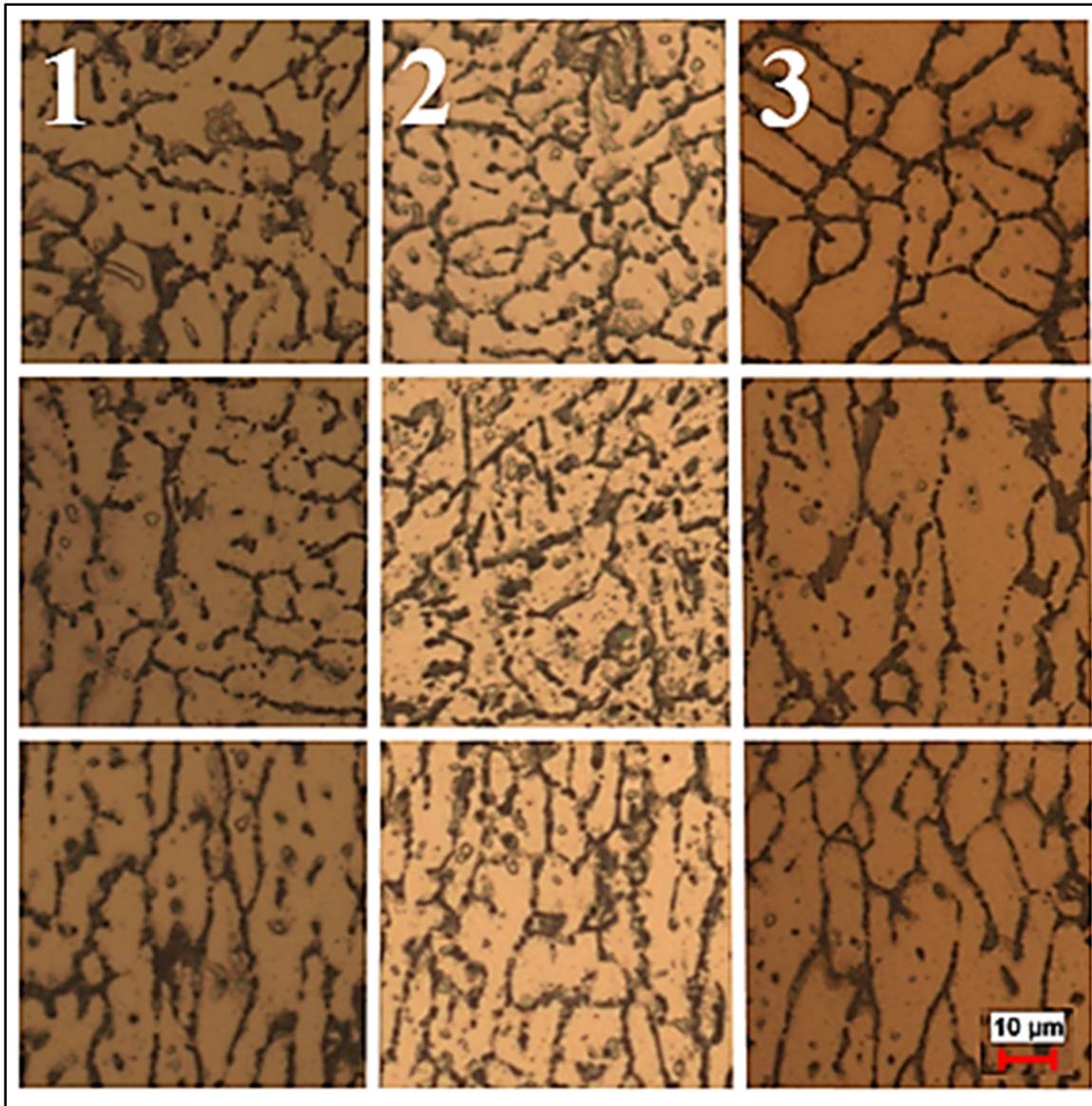


Figure 2.10 Metallography images of samples from the height of the walls with a magnification of 500 $\times$ .

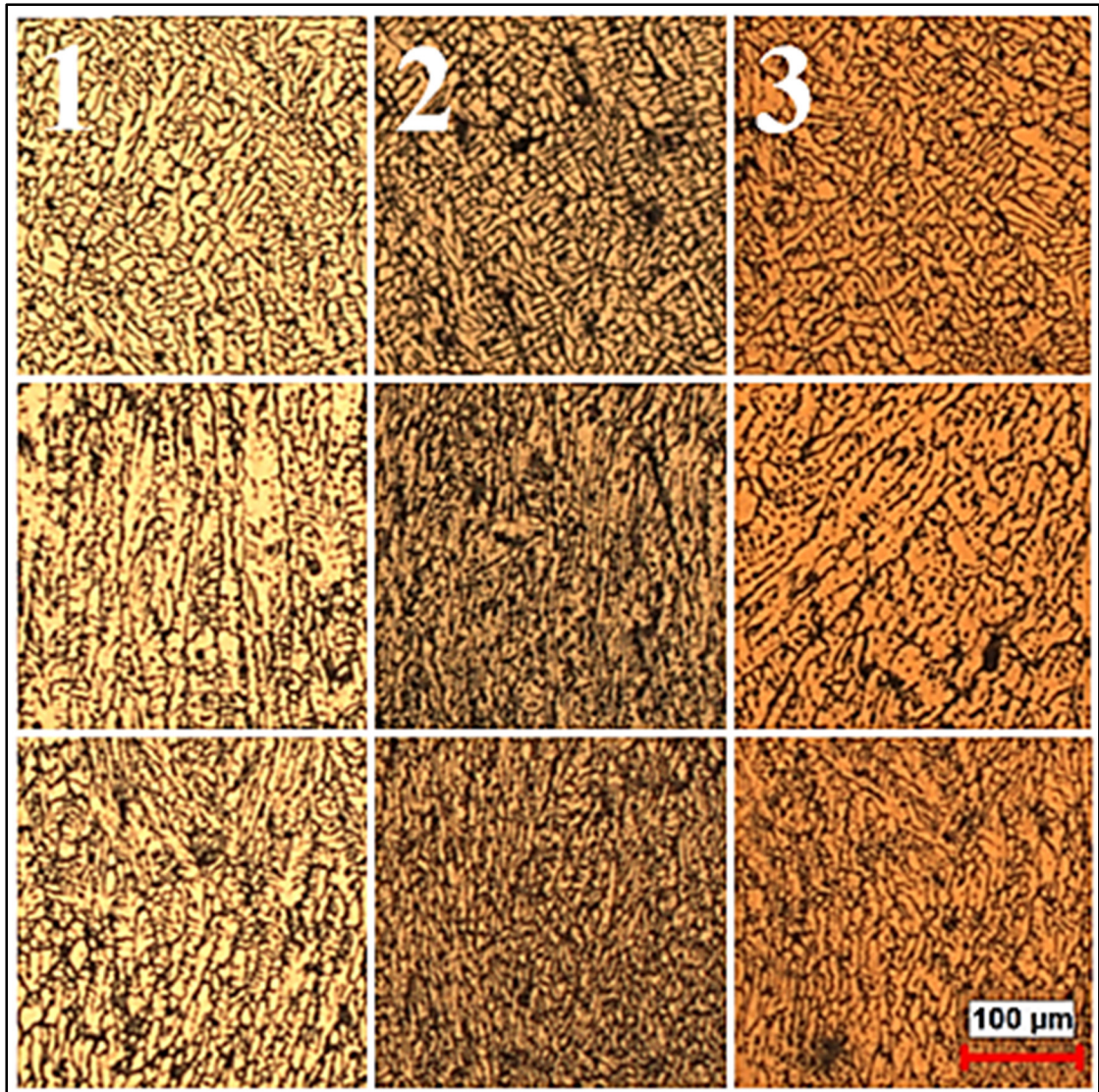


Figure 2.11 Metallography images of samples from the height of the walls with a magnification of  $100\times$ .

Figures 2.10 and 2.11 show the size and the configuration of dendrites from the top part of the three tests. In these figures, the dendritic structure in Test 1 and Test 3 is more columnar, while in some areas of the dendritic structure of Test 2, the equiaxed structure is seen. Also, the columnar dendritic structure in Test 3 is bigger than in Test 1. This shows that dendritic columns in Test 3 have grown with a slower speed along the thermal gradient, so the porosities that did nucleation between the dendritic arms have had enough time to move towards each other and combine and make bigger porosities. Therefore, for the second test that has a smaller

and equiaxed dendritic structure, the nucleation of porosity in between dendritic structure doesn't have enough space and time to combine with other nucleation and gets stuck between the dendritic structure, therefore the size of the porosities would stay smaller.

Figure 2.12 presents the width of the hardness profile in the middle of the wall for all the three tests. This diagram shows that the distribution of hardness in the width of the wall for Test 2 is less than the distribution of hardness in the two other tests. By drawing the normal distribution diagram of hardness in width of the wall of all tests (Figure 2.13), it is clearly seen that when DYN value is adjusted towards negative percentages, not only the width's hardness distribution becomes lower, but also the average of hardness increases. However, when DYN value is adjusted towards positive percentages, the width's hardness distribution becomes higher, and the average of hardness doesn't change much.

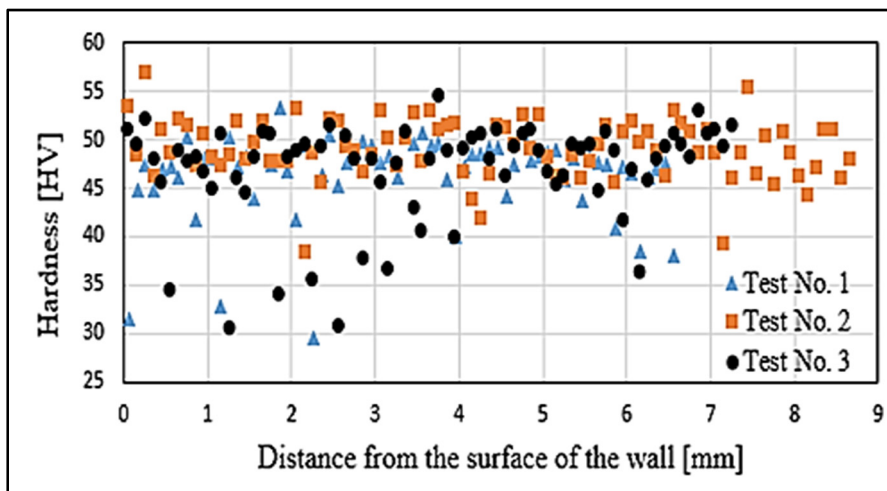


Figure 2.12 Hardness profile of the width of the walls.

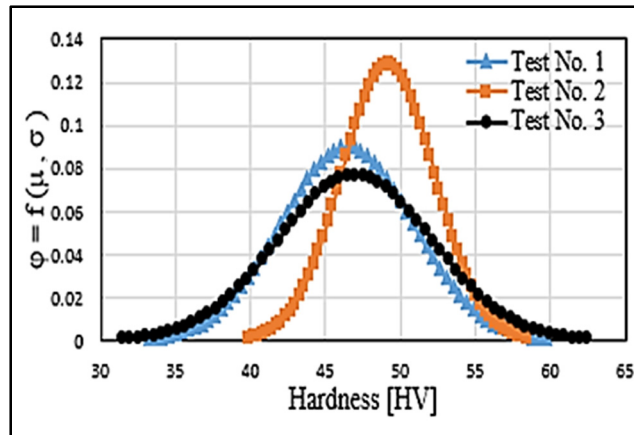


Figure 2.13 Normal distribution diagram of hardness of the width of the walls.

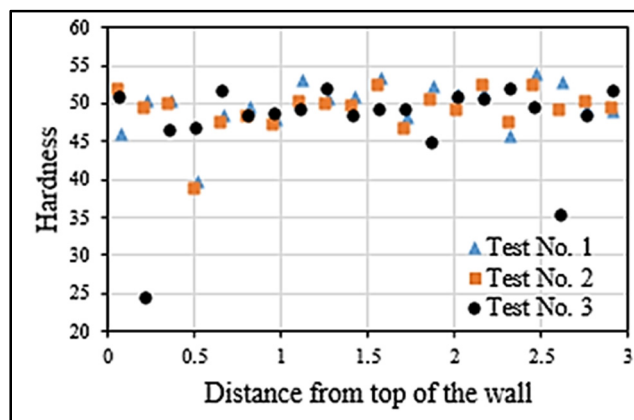


Figure 2.14 Hardness profile along the height of the walls.

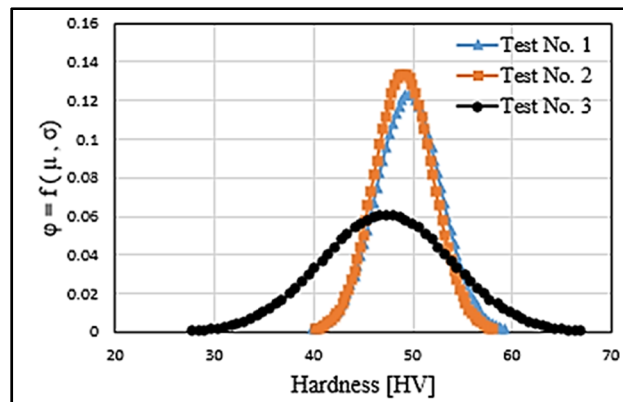


Figure 2.15 Normal distribution diagram of hardness along the height of the walls.

Figure 2.14 shows the hardness profile along the height of the wall. The importance in this zone is that the dendritic structure is not influenced by the heating of upon passes, and the amount and form of this dendritic structure won't change. In this diagram, Test 1 and Test 2 have a similar hardness profile, while the hardness distribution in Test 3 is higher. Figure 2.15 shows the normal distribution diagram of hardness in height of the wall. Based on this diagram, when changing the DYN towards negative percentages (Test 2), there is no big difference in hardness distribution and the average of hardness compared to that in Test 1 where DYN is zero. But if DYN is adjusted toward positive percentages, hardness distribution increases and average hardness decreases.

## **2.4 Conclusion**

In Pulsed Synergic Mode (GMAW-P), by adjusting DYN towards negative percentages, the size of the droplets decreases while their amount increases. This makes the roughness of the surface of the produced wall by WAAM to be poor and the value of the surface waviness (SW) increases. This is while, due to WFS' augmentation and TS' diminution, the deposition increases, and finally the amount of effective wall thickness (EWT) increases. The dendritic structure for the produced walls with a negative DYN changes from coarse columnar to equiaxed. Therefore, porosities in these walls are finer and their density is lower. Also, hardness distribution is lower in these walls, while the average of hardness is higher.

## CHAPTER 3

### **ASSESSING THE EFFECTS OF SYNERGIC GMAW-P PARAMETERS ON WELD CURRENT AND HEAT INPUT IN ALUMINUM ROBOTIC ARC WELDING USING THE DESIGN OF EXPERIMENTS<sup>6</sup>**

#### **Abstract**

The control of heat input during welding has a great influence on the weld seam geometry, as well as the mechanical and metallurgical properties of the welding joint. The amount of residual stresses and distortion in the welded workpiece is directly related to the amount of weld heat input. Gas metal arc welding (GMAW) provides an abundant amount of heat input and, despite modified and controlled metal transfer modes and optimization of feeding techniques, such as synergic control, precision in setting the GMAW parameters is essential to achieve optimal heat input. Weld current, voltage, and speed, which depend on the welding parameters and conditions, are the most important factors that affect weld heat input. The purpose of this study is to identify the effective welding parameters in the weld current and the heat input, then find a model to control the heat input by using the proper setting of the welding parameters. The studies deal with robotic arc welding of aluminum with GMAW-P, and to reduce the number of tests and summarize the trials, statistical methods and design of experiments (DOE) have been used. As a result of this study, two mathematical models for weld current and heat input were created. By using these models, adjustment of weld parameters is effectively and accurately achieved.

Keywords: Aluminum, Analysis of Variance (ANOVA), Design of experiments (DOE), Heat input, Pulsed Gas Metal Arc Welding (GMAW-P), Regression, Robotic arc welding, Synergic control

---

<sup>6</sup> This chapter has been accepted for presentation at CanWeld Conference 2020.

### 3.1 Introduction

Gas Metal Arc Welding (GMAW) is seen as one of the most interesting welding methods in the industry because of its capacity to be semi-automatic or automatic. It is a fusion welding process that produces metal coalescence by creating a welding arc that causes the continuous filler metal electrode and the workpieces to heat, melt and, therefore, bond [118, 119].

One of the concerns of welding engineers is to adjust the welding parameters and to provide appropriate operation control models that reflect the interaction of the welding parameters and their effect on the optimum quality of the weld bead [120].

Heat input is a welding parameter that indicates the energy transferred from the electric arc to the base metal. The amount of heat input is calculated as a function of current, voltage and, travel speed [121-123]. The heat input value is adjusted based on the thickness of base metal, and it affects the melting pool size, amount of liquid metal, weld penetration, welded zone width, and HAZ width [124, 125]. Hot cracking, grain size, and the impact strength value at the welding joint can be controlled by the amount of heat input for welding. Residual stress, deformation, and distortion of welded parts are important welding problems, which are controlled in part by the amount of heat input [33, 126-128].

The design of experiments (DOE) is a statistical method to obtain the maximum information with the least possible testing. In DOE, the factors are independent variables (the inputs to the experiment) that are controlled by the experimenter, and the levels refer to the possible values of a factor in an experimental design throughout the progress of the experiment. The responses are the outputs of the experiment, i.e. the dependent variables [129-131]. After performing all of the trials specified in the DOE Plan, firstly, the effects of multiple levels of numerous factors in each response are compared by analysis of variance (ANOVA), and then an empirical regression model is developed based on the results of ANOVA. Finally, the possible output (response) can be predicted based on the input parameters (factors) of the experimental set-up using the obtained model [132-134].

Wooluru et al. [135] presented the models for penetration, weld bead width, and dilution for Pulsed MIG Welding Using DOE. Izeda et al. [136] used the Taguchi method (DOE) to

optimize bead width, bead penetration, and bead reinforcement for robotic welding in aluminum alloys with pulse transfer mode. Rajendran et al. [137] acquired a model for the ultimate tensile stress (UTS) for AA2014-T6 aluminum alloy joints by adjusting the parameters of friction stir welding (FSW). Subramaniam et al. [138] attempted to model pulse parameters in pulsed GMAW using DOE techniques, such as fractional factorial design and D-optimal design. Allen et al. [139] modeled the GMAW robot parameters to achieve the minimum welding cycle time by maximizing the welding speed. Choudhary et al. [140] introduced the bead width, reinforcement, and penetration models using statistical methods; and discussed the parameters that affect these responses. Nagesh and Datta [141] studied the welded fillet joint of the GMAW process using an integrated approach based on DOE, Artificial Neural Networks (ANN), and Genetic Algorithm (GA). Khamari et al. [142] investigated the influence of welding current and material thickness on the mechanical and microstructural properties of GMAW and SMAW mild steel joints. Hackenhaar et al. [143] investigated the effect of GMAW parameters on fusion efficiency using DOE. In welding research, fusion efficiency is the fraction of net energy delivered that effectively melts the metal, and the portion of arc energy that is lost in the environment is not considered [144]. Vaithiyanathan et al. [145] used DOE and attempted to obtain the maximum tensile strength of Ti-6Al-4V sheets applied in aero-engine components by optimizing gas tungsten arc welding (GTAW) parameters. Dinovitzer et al. [67] studied the influence of welding parameters in TIG-based WAAM using the technique of Taguchi and ANOVA.

The purpose of this study is to identify the effective welding parameters in the heat input and find a model to control the heat input by properly setting the welding parameters. In this article, the design of experiments (DOE) and statistical techniques were adopted to investigate the influence of the most significant parameters of GMAW-P in robotic arc welding with the aim of modeling weld current and heat input.

### **3.2 Experimental Procedure**

To study the influence of the most significant parameters of the GMAW-P in robotic arc welding of aluminum with the aim of modeling the weld current and the heat input, the welding

depositions were done on a plate “bead-on-plate” by GMAW-P synergic mode. To perform the experiments, a robotic system consisting of the Fronius TransPuls Synergic 4000R power source and the Yaskawa Motoman MH6 welding robot was used. The synergic mode of this process is intended to keep the arc length (welding voltage) stable for different wire feed speeds and, as a result, for different current values. In other words, when the current increases during welding, a correction of the voltage that is already programmed in the machine's memory is made by changing the value of the wire feed speed. Therefore, welding voltage modeling for a synergistic welding machine has not been carried out in this study, and the voltage is almost constant in all trials [146, 147].

In this research, ER4043 welding wire with a diameter of 1.2 mm was used as filler metal and 6061-T6 plates with dimensions of 38 mm × 9.45 mm × 127 mm were applied as substrate materials (Table 3.1). Pure argon ( $Ar \geq 99.9996$ ) was used as a protective gas during welding.

Table 3-1 Chemical composition of ER4043 and 6061 alloy (wt %)

	Al	Si	Mg	Fe	Cu
ER4043	Balance	4.50-6.00	0.05 max	0.80 max	0.30 max
6061	Balance	0.40-0.80	0.80-1.20	0.70 max	0.15-0.40

In the robotic system used in this research, wire feed speed (WFS), welding travel speed (TS), contact-tube-to-work distance (CTWD), Dynamic/Pulse correction (DYN) and Argon flow rate are the most important parameters, customizable by the operator and are known as independent factors chosen for GMAW-P parameter development.

The weld current frequency value is adjusted by DYN. In Fronius TransPuls Synergic 4000, the DYN range is adjustable from -5% to + 5% [148, 149].

Parameters adjusted by the robotic system based on independent factors include the average wire feed speed, as well as the average weld current and voltage. As already mentioned, the synergic mode keeps the welding voltage approximately constant (22–25 V) by changing the wire feed speed. Therefore, the dependent parameters (responses) that are modeled in this investigation are the average weld current and the heat input.

For this research, firstly, the plan was to identify independent and process control factors and setting them at three levels. Then, by using Taguchi and Definitive Detection Design

techniques, a matrix for this experiment was obtained. Secondly experiments were performed according to the design matrix and the obtained results for the average wire feed speed, the average welding voltage, and the average welding current were recorded. Thirdly, by visual examination of the weld seams, the tests that had the best quality of weld seams were chosen. Fourthly, based on the trials selected in the previous section and with the Analysis of Variance (ANOVA), the effect of each factors on their respective response (welding current and heat input) was found. Finally, an empirical model for each response was developed by using linear regression.

In previous tests, the initial adjustments were obtained by trials and errors as indicated in Table 3.2. In this investigation, it was decided to optimize and extend the initial settings using DOE. The definition of the terminology and abbreviations is given in Table 3.3.

Table 3-2 Initial settings of the parameters

WFS (ipm)	TS (ipm)	CTWD (mm)	Argon (cfh)	DYN (%)	I <sub>avg</sub> (Amp)	V <sub>avg</sub> (V)	WFS <sub>avg</sub> (ipm)
299.2	46	19	35	5	148	25.2	295.3

Table 3-3 Terminology and definitions

Abbreviation	Definition	Unit
WFS	Wire Feed Speed	ipm
TS	Travel Speed (Welding speed)	ipm
CTWD	Contact Tip to Work Distance	mm
Argon	Argon flow rate	cfh
DYN	Dynamic Pulse Correction (Percentage change in the Pulse frequency)	%
I <sub>avg</sub>	Average current	A
V <sub>avg</sub>	Average voltage	V
WFS <sub>avg</sub>	Average WFS set by the synergic system	ipm
H. I.	Heat input	kJ/in

The purpose of this investigation is to find the most effective degree of the parameters and to optimize the previous tests based on the DOE. Therefore, five factors are investigated at three levels. Table 3.4 shows these factors and their minimum and maximum values.

Table 3-4 Factors and interval values of the test

Factor	Min. value	Max. Value
WFS (ipm)	275.6	322.8
TS (ipm)	44	48
CTWD (mm)	14	19
Argon (cfh)	30	40
DYN (%)	-5	5

Examining the effect of 5 factors on 3 levels, and their interactions in response should involve at least  $3^5$  (= 243) tests. However, by using Taguchi method the number of tests could be significantly reduced. In fact, Taguchi is a statistical method that decreases the number of trials, including all factors that affect performance parameters using the orthogonal matrix method [150]. To examine the effects of 5 factors on three levels, the number of experiments was reduced to 27 tests using the orthogonal matrix L 27 ( $3^5$ ) of the Taguchi technique.

Same as Taguchi method, Definitive Screening Designs allows the experimental study of many factors in a small number of runs [105]. For example, to examine the impacts of 5 factors on 2 levels in one response, it was necessary to perform 13 tests by using Definitive Screening Designs technique.

### 3.3 Results and Discussion

Setting welding parameters based on Taguchi or Definitive Screening Designs techniques cannot guarantee the quality of weld beads in practice.

Therefore, in this study, 40 samples were welded according to the settings provided by Taguchi and the Definitive Screening Design techniques. Then, when verifying the quality of the weld seams, 12 samples with the best visual quality were selected for the continuation of the studies.

The settings for the selected samples are presented in Table 3.5, where WFS<sub>avg</sub> (Wire Feed Speed set by Synergic System) replaces WFS (Taguchi-based wire feed speed and final screening designs), and each test is a 10 cm weld bead.

Table 3-5 Selected tests based on the quality of the weld bead

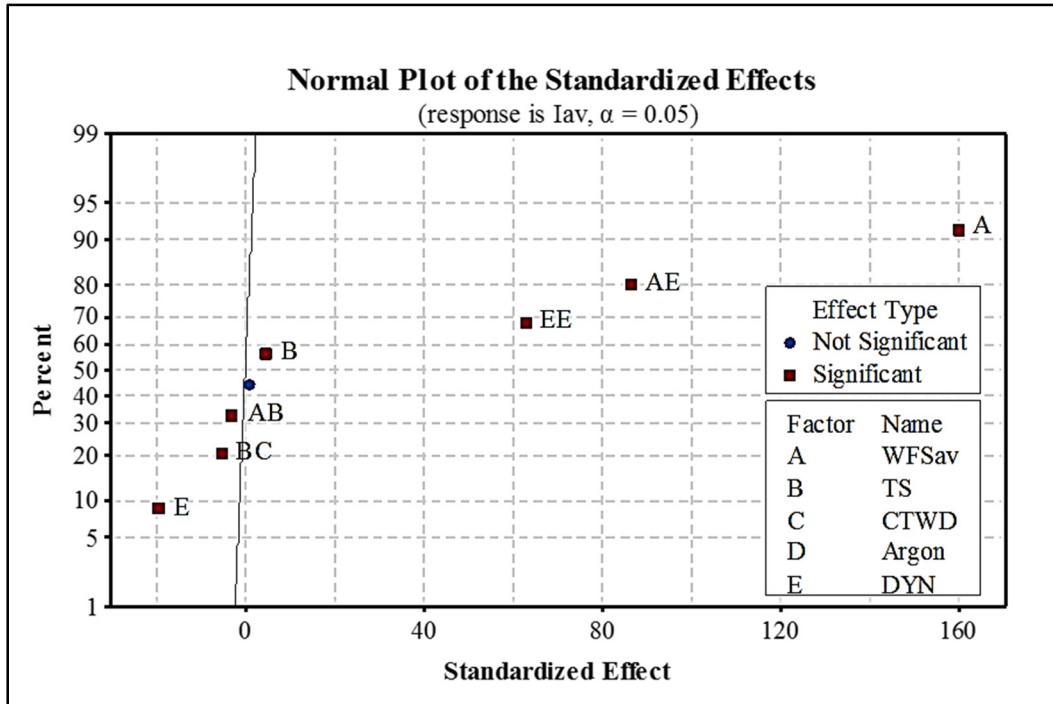
WFS <sub>avg</sub> (ipm)	TS (ipm)	CTWD (mm)	Argon (cfh)	DYN (%)	I <sub>avg</sub> (A)	V <sub>avg</sub> (V)	H.I. (kJ/in)
299.2	44	17	40	-5	156	22.7	4.829
299.2	44	17	40	5	151	24.9	5.127
295.3	46	19	30	-5	154	22.9	4.600
295.3	48	14	35	-5	155	23	4.456
318.9	44	19	35	-5	171	23.8	5.550
322.8	46	14	40	-5	173	23.5	5.303
322.8	46	14	40	0	170	25.1	5.566
318.9	48	17	30	-5	170	23.9	5.079
299.2	44	14	30	-5	155	22.8	4.819
275.6	48	14	35	-5	142	22.6	4.012
322.8	44	14	40	0	169	25.4	5.854
318.9	48	14	30	5	199	24.7	6.144

The ANOVA test for I<sub>avg</sub> is presented in Table 3.6. It is remarked that only the P-value for CTWD is greater than 0.05, which indicates that the CTWD is not individually affected by I<sub>avg</sub>. But the normal plot and Pareto charts shown in Figure 3.1.a and Figure 3.1.b prove that I<sub>avg</sub> takes the most effect from WFS<sub>avg</sub>, (WFS<sub>avg</sub> × DYN), (DYN<sup>2</sup>), and DYN respectively. Based on the ANOVA test, among the factors affecting I<sub>avg</sub>, there is no trace of argon flow rate, which suggests that it does not affect the visual quality of the weld bead. However, further examination of the argon flow rate's effect on porosity and microstructure of weld bead should be performed.

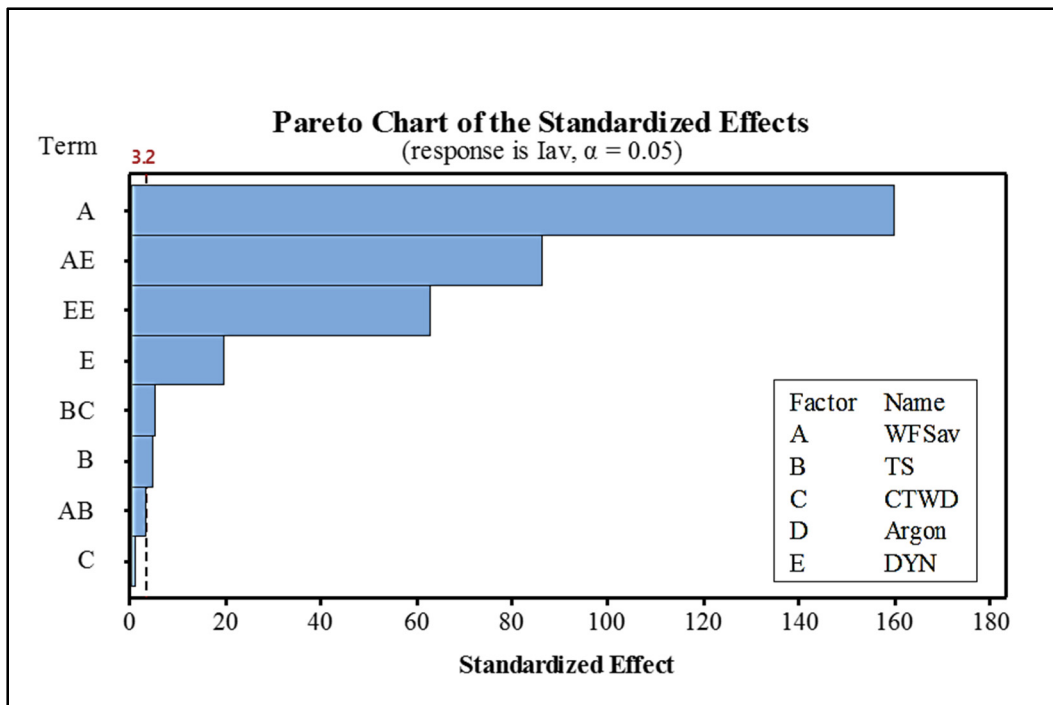
Table 3-6 Analysis of Variance for  $I_{avg}$ 

Source	DF	Adj SS	Adj MS	F-Value	P-Value
Model	8	2430.12	303.77	7116.81	0.000
Linear	4	1278.50	319.63	7488.40	0.000
WFS <sub>avg</sub>	1	1089.25	1089.25	25519.56	0.000
TS	1	0.89	0.89	20.92	0.020
CTWD	1	0.03	0.03	0.81	0.435
DYN	1	16.27	16.27	381.14	0.000
Square	1	168.17	168.17	3939.98	0.000
DYN <sup>2</sup>	1	168.17	168.17	3939.98	0.000
2-Way Interactions	3	348.40	116.13	2720.81	0.000
WFS <sub>avg</sub> ×TS	1	0.44	0.44	10.21	0.050
WFS <sub>avg</sub> ×DYN	1	318.18	318.18	7454.48	0.000
TS×CTWD	1	1.20	1.20	28.15	0.013
Error	3	0.13	0.04		
Total	11	2430.25			

The interaction plot for  $I_{avg}$  shown in Figure 3.2 confirms that there is a strong interaction between the WFS<sub>avg</sub> factor and the DYN factor. In other words, the effect of WFS<sub>avg</sub> in  $I_{avg}$  is dependent on DYN.



a)



b)

Figure 3.1 The most effective parameters on I<sub>avg</sub>. (a) Normal plot; (b) Pareto chart.

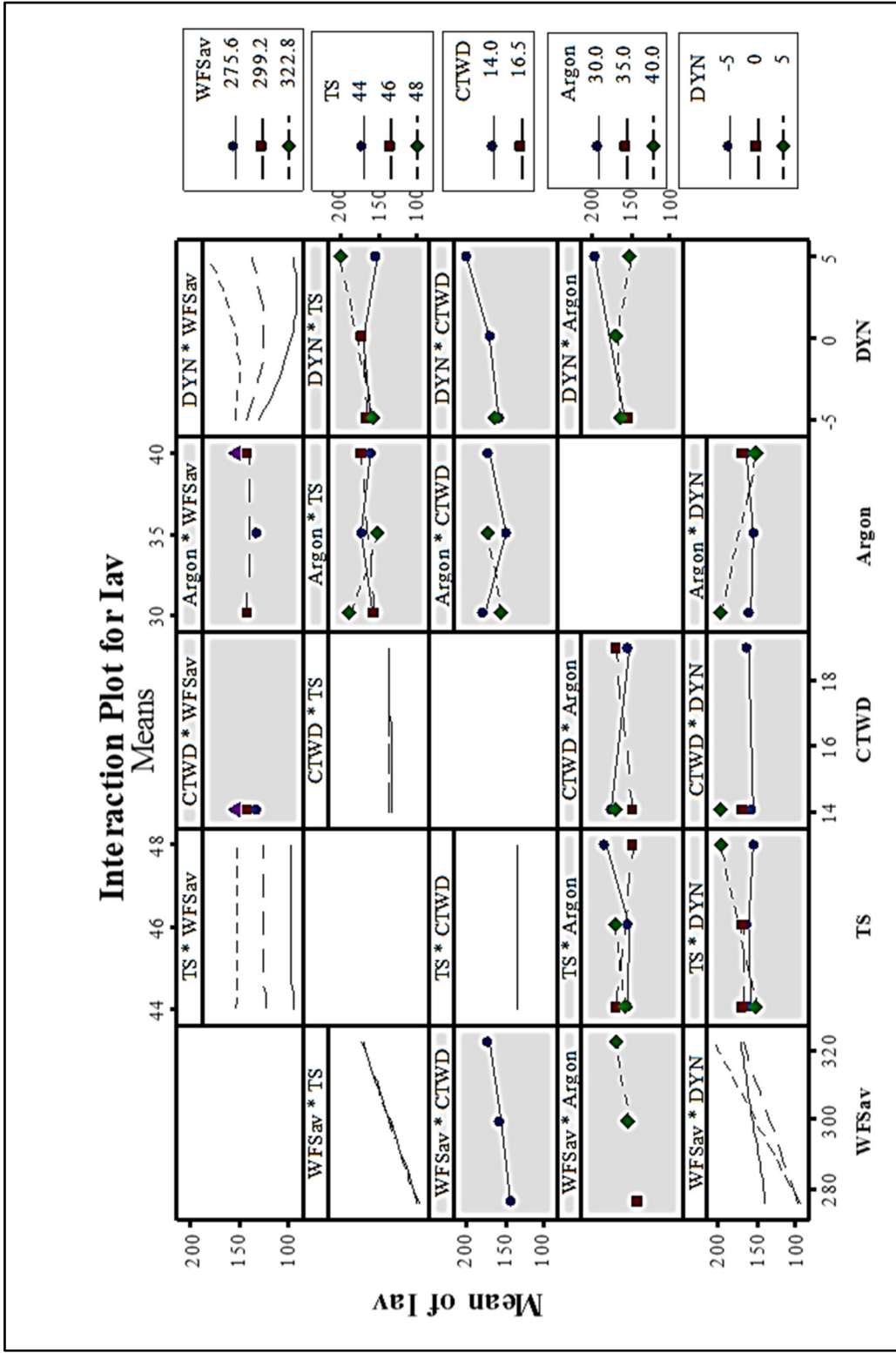


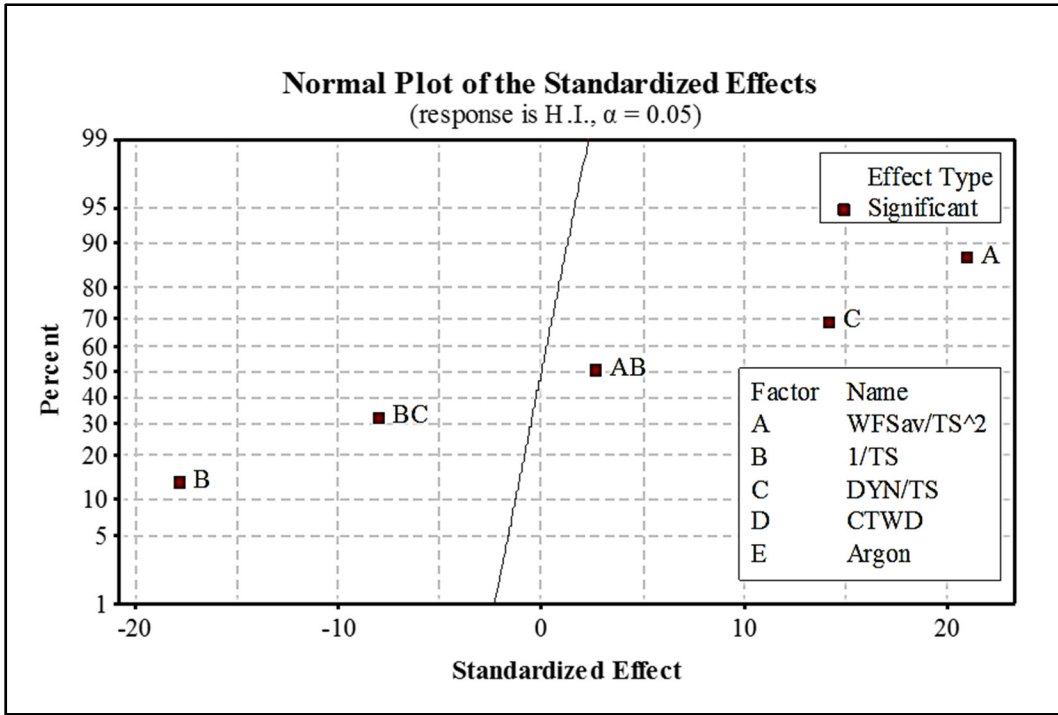
Figure 3.2 Interaction plots displaying significant trends between factors and response (A gray background represents a term not in the model)

To do the ANOVA test for heat input (H.I.), some changes to the response and factors were considered. Firstly, the values of H.I. were calculated based on the heat input formula ( $0.06 \times I_{avg} \times V_{avg}/TS$ ) and were considered as a response. Secondly, the factors were considered as  $WFS_{avg}/TS^2$ ,  $1/TS$ , and  $DYN/TS$ . P-Values and the interaction between them was less than 0.05 (Table 3.7). Therefore, as shown in Figure 3.3.a and Figure 3.3.b, the factors affecting the H.I. response were respectively  $WFS_{avg}/TS^2$ ,  $1/TS$ ,  $DYN/TS$ ,  $DYN/TS^2$ , and  $WFS_{avg}/TS^3$ .

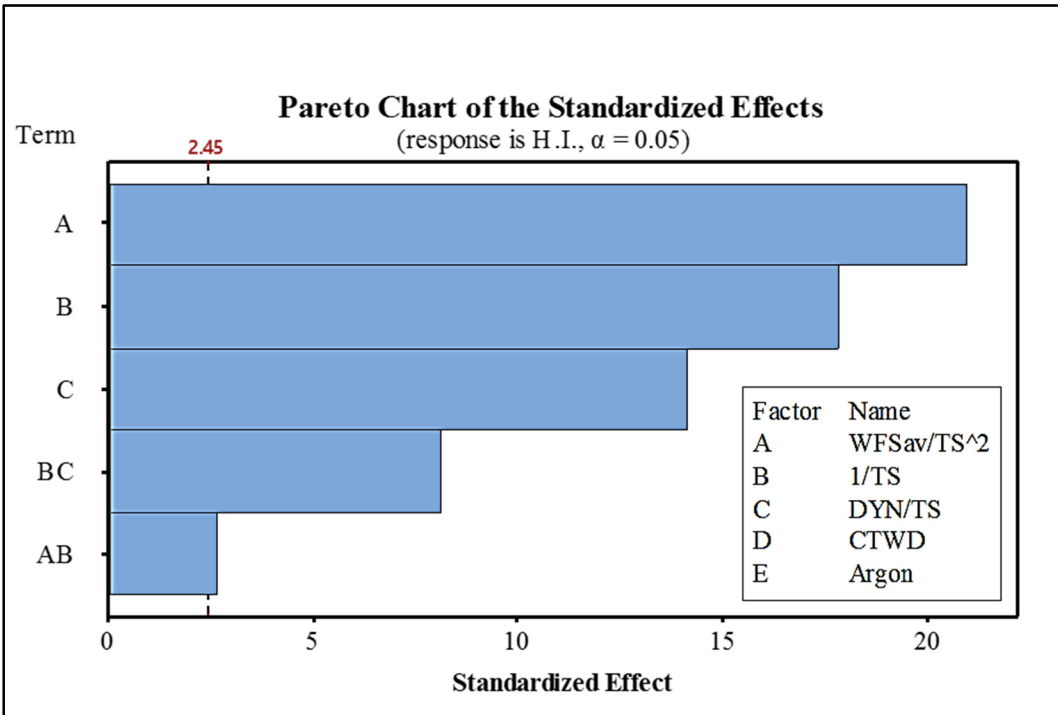
Table 3-7 Analysis of Variance for H.I.

Source	DF	Adj SS	Adj MS	F-Value	P-Value
Model	5	4.09749	0.81950	220.75	0.000
Linear	3	3.18073	1.06024	285.60	0.000
$WFS_{avg}/TS^2$	1	1.63070	1.63070	439.27	0.000
$1/TS$	1	1.18529	1.18529	319.29	0.000
$DYN/TS$	1	0.74119	0.74119	199.66	0.000
2-Way Interactions	2	0.25477	0.12738	34.31	0.001
$WFS_{avg}/TS^3$	1	0.02618	0.02618	7.05	0.038
$DYN/TS^2$	1	0.24361	0.24361	65.62	0.000
Error	6	0.02227	0.00371		
Total	11	4.11976			

As presented in Figure 3.4, the interaction plot for H.I. confirms that there is a strong interaction between  $WFS_{avg}/TS$ ,  $1/TS$  factors and  $DYN/TS$ ,  $1/TS$  factors.



a)



b)

Figure 3.3 The most effective parameters on H.I. (a) Normal plot; (b) Pareto chart.

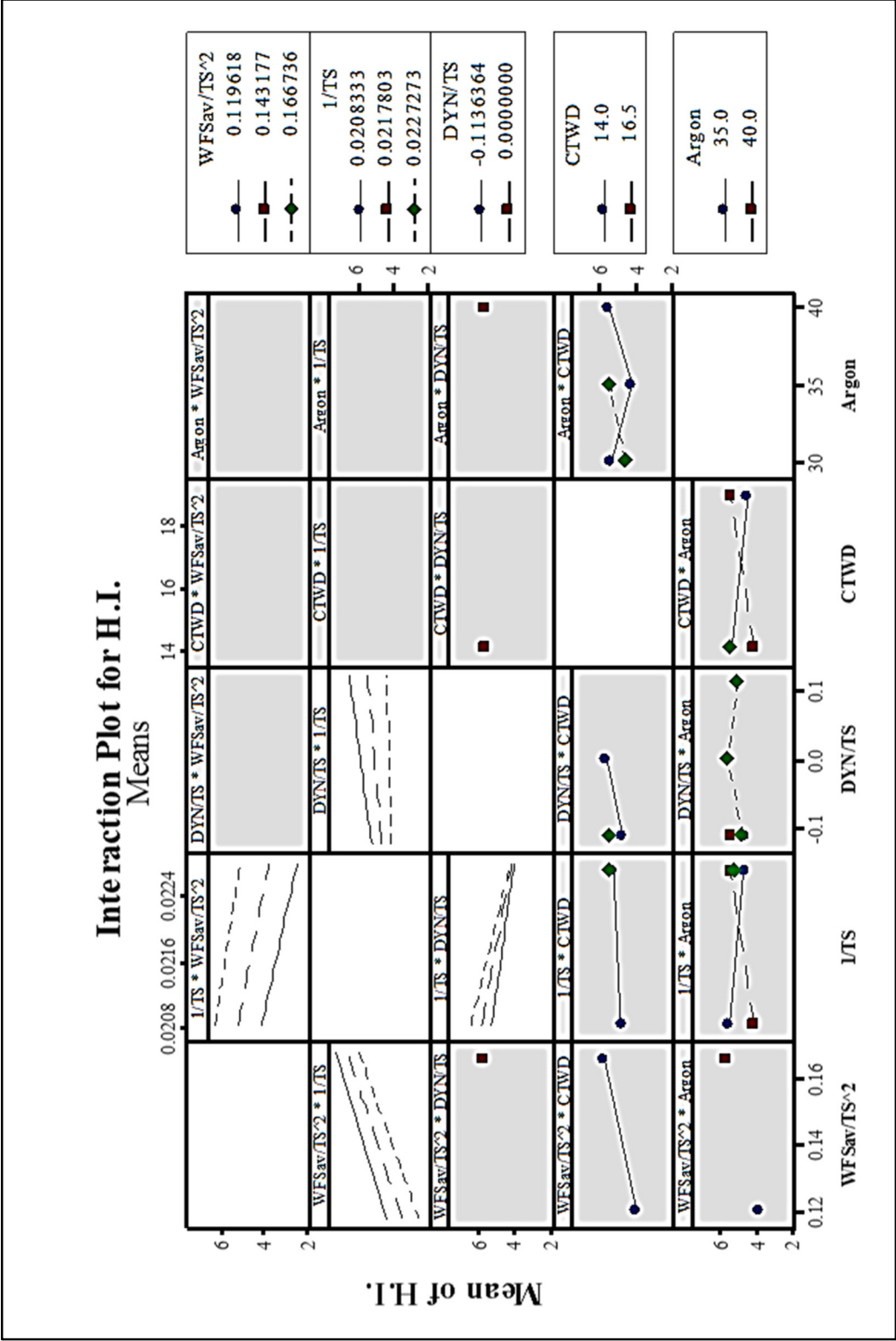


Figure 3.4 Interaction plots displaying significant trends between factors and response (A gray background represents a term not in the model)

Subsequently, using the regression option in the Minitab software, based on the DOE factors, a mathematical model for  $I_{avg}$  was obtained.

It should be noted that the P-values of  $TS \times CTWD$ ,  $TS$  and  $WFS \times TS$  were greater than 0.05 in the first attempt to analyze the regression. Then, these interactions were eliminated and the P-values for all factors ( $DYN2$ ,  $DYN$ ,  $WFS_{avg} \times DYN$  and  $WFS_{avg}$ ) became zero in the subsequent regression analysis, which indicates that there is no correlation between them.

$$I_{avg} = -332.0 + (0.8436 \times DYN^2) - (53.43 \times DYN) + (0.17661 \times WFS_{avg} \times DYN) + (1.5535 \times WFS_{avg})$$

(Equation 3-1)

$I_{avg}$  model coefficient of determination is  $R^2 = 99.70\%$ , which indicates its good explanatory performance. Durbin-Watson Statistic is  $D = 2.23$ , which shows the good level of the autocorrelation of residuals.

Through the same method, a mathematical model for H.I. was obtained using the regression option in the Minitab software.

$$H.I. = 23.32 + \left(\frac{1}{TS}\right) \times \left[ -1236.1 + (46.47 \times DYN) - \left(\frac{1990 \times DYN}{TS}\right) + \left(\frac{2781 \times WFS_{avg}}{TS^2}\right) \right]$$

(Equation 3-2)

The coefficient of determination of the H.I. model is  $R^2 = 99.26\%$ , which indicates its good explanatory performance. Durbin-Watson Statistic is  $D = 1.83$ , which shows the good level of the autocorrelation of residuals.

According to previous research, when  $DYN$  is set at  $-5\%$ , the weld bead will have the lowest porosity [149]. For the welding of aluminum alloys by the GMAW-P mode, when the diameter of the aluminum wire used as filler metal is 1.2 mm,  $I_{avg}$  must be at least 140 A to provide a stable arc [105, 150]. Therefore,  $I_{avg} = 142$  A and  $DYN = -5\%$  were first considered in this

study, and then the remaining parameters were extracted through the DOE of the investigation as shown in Figure 3.5.

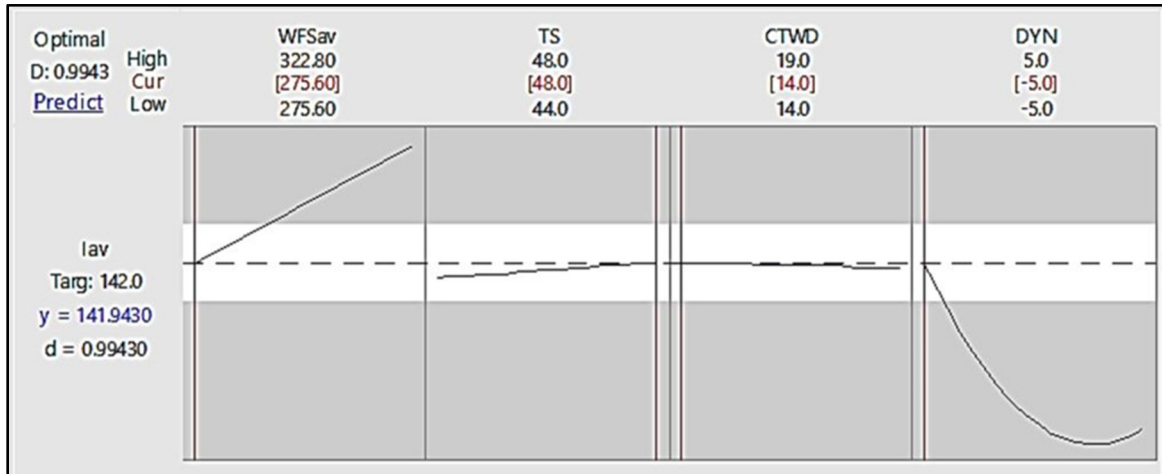


Figure 3.5 Optimization plot for  $I_{avg}$ .

When inserting the DOE results in the  $I_{avg}$  mathematical model (Equation 3-1), the average weld current  $I_{avg}$  is 141 A. In the next step, the welding machine (Fronius TransPuls Synergic 4000) was adjusted based on the DOE results and welded a 10 cm weld bead. The practical results and the image of the weld bead are shown in Table 3.8 and Figure 3.6.

Table 3-8 Practical results of welding

WFS	TS	CTWD	Argon	DYN	$I_{avg}$	$V_{avg}$	H.I.
(ipm)	(ipm)	(mm)	(cfh)	(%)	(Amp)	(V)	(kj/in)
275.6	48	14	40	-5	144	22.1	3.978

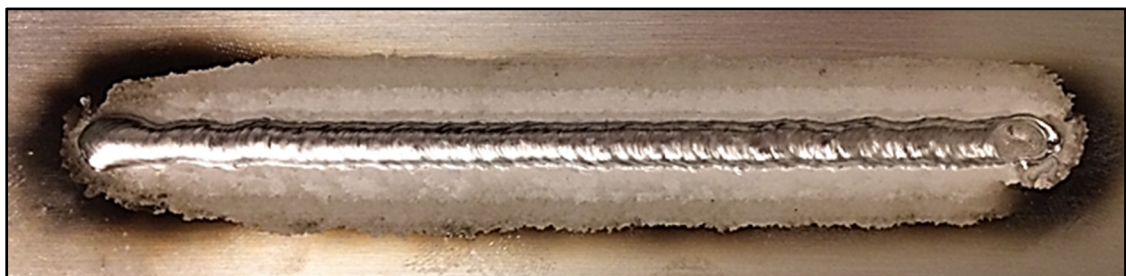


Figure 3.6 The weld seam appearance.

According to Table 3.8, the practical values of factors were considered in DOE and the H.I. result obtained by Minitab became 3.978 (kj/in) as indicated in Figure 3.7.

On the other hand, by putting the practical values of factors in the H.I. mathematical model (Equation 3-2), the value of the theory of H.I. based on the model were 3.976 (kj/in).

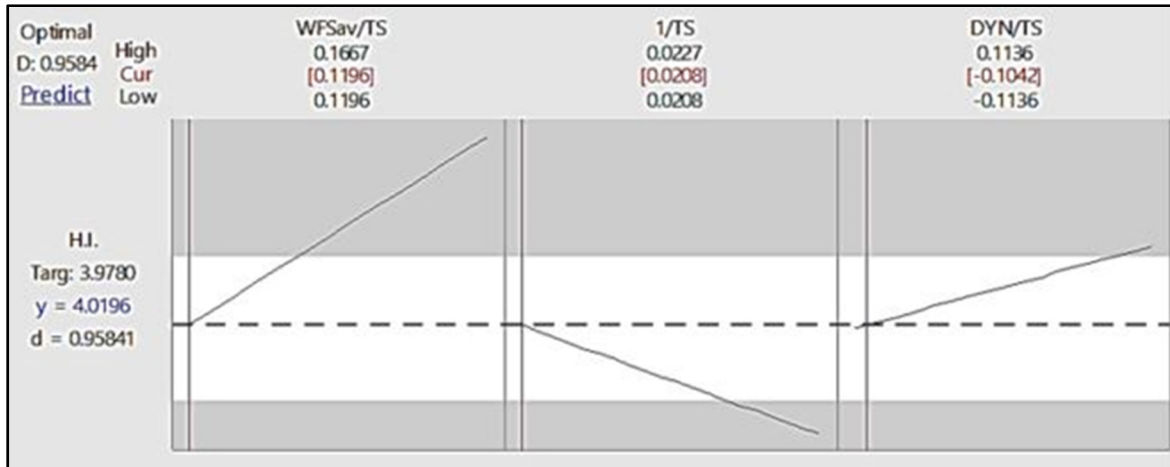


Figure 3.7 Optimization plot for H.I.

### 3.4 Summary and conclusion

The influence of the most significant parameters of the GMAW-P in robotic arc welding of aluminum was studied to model the weld current and heat input; welding operations were used with simple depositions on a plate (“bead-on-plate”) by GMAW pulse synergic mode. Five factors (WFS, TS, CTWD, DYN, and argon flow rate) were investigated at three levels. The number of trials was summarized using the DOE technique. Based on the selected trials, ANOVA determined the effects of multiple levels of various factors in every response (weld current and heat input). Then two empirical models for weld current and heat input were developed by linear regression. Based on the weld current model, the values of the welding parameters were calculated for 142 (A) weld current. The welding machine was adjusted based on the calculated parameters and the welding was practically done. The appearance of the weld seam was of good quality, and the parameter values were obtained from the welding machine based on practical welding. The practical values of the weld current were 144 (A), and H.I. equaled 3,978 (kj/in). By inserting the values of the practical parameters in the H.I. model, the

value of H.I. was obtained based on model 3.976 (kj/in). Therefore, the error of the models obtained is  $-1.4\%$  for the weld current and  $-0.05\%$  for H.I., which is an acceptable error for welding. The obtained models proved to have a good performance in setting the welding parameters to achieve optimum heat input.



## CHAPTER 4

### AN INVESTIGATION OF THE EFFECTS OF WELDING PARAMETERS ON THE PROPERTIES OF THIN WALL PIECES OF AL-SI ALLOY MADE USING GMAW-BASED WIRE ARC ADDITIVE MANUFACTURING<sup>7</sup>

#### Abstract

Wire arc additive manufacturing (WAAM) is a near-net shape part manufacturing method, which, in recent years, has seen increased attention paid to its use in the production of aluminum alloy parts in industry. As a WAAM technique, pulsed gas metal arc welding (GMAW-P) with two different sets of welding parameters was used in this study. Two thin walls made of ER4043 filler were created using this WAAM technique. The surface roughness, microstructure, porosity, and mechanical properties of the walls were investigated. Results show that the surface roughness increases as the heat input, which is directly related to the welding current, rises as well. When the heat input is increased, a portion of the aluminum may evaporate, leading to a change in the chemical composition of the alloy. Thus, although a coarser microstructure is created, changes in microhardness are not noticeable. Boosting the heat input results in increases in both the number and sizes of gas pores. The tensile strength and elongation of both walls are higher in the longitudinal direction (parallel to the weld passes) than in the height direction.

Keywords: ER4043 Aluminum alloy, Heat input, Pulsed gas metal arc welding (GMAW-P), Robotic arc welding, Synergic control, Wire arc additive manufacturing (WAAM)

---

<sup>7</sup> This chapter has been accepted for presentation at the Conference of metallurgists (COM2020).

## 4.1 Introduction

Additive manufacturing (AM), called 3D printing, is a technology used for low cost near-net shape part manufacturing [11]. AM processes can mainly be classified as directed energy deposition (DED) or powder bed fusion (PBF) processes[151]. Wire arc additive manufacturing (WAAM) is a DED process used to build net shape metal pieces through a layer-upon-layer deposition technique by simultaneously using an electric arc as a primary heat source and a wire as a feedstock [67, 152]. Some welding methods, such as gas metal arc welding (GMAW), gas tungsten arc welding (GTAW), and plasma arc welding (PAW), are used for the WAAM process [56]. The lower capital costs and the higher deposition rate provided by WAAM are two of its main advantages over other forms of metallic additive manufacturing [104]. Among the WAAM welding technologies, the GMAW-based welding technology is considered in many studies due to its higher deposition rates in the manufacture of large parts [153, 154]. One of the problems with parts manufactured by WAAM processes is their high surface roughness, which inevitably requires subsequent machining [40]. The parameters of the WAAM process, such as the heat input, travel speed, layer height, and scan strategy, affect surface roughness [35]. Research results indicate that in a close range of travel speeds (TS), the surface roughness becomes suitable for WAAM parts. In other words, when the welding speed is less than the range threshold, the surface roughness will increase because the weld pool becomes larger and hotter. At very high TS, humps and valleys occur above the weld layer, and the electric arc becomes unstable [40, 84, 155]. Xiong et al. [156] tried to present a process planning that could improve the surface roughness of WAAM parts by using a variable bead width during the process.

Most of the research of WAAM focuses on metals such as stainless steels, titanium alloys, and nickel alloys [157-159]. The use of aluminum alloys in the automobile, aerospace, construction, and other industries has been growing in recent decades owing to properties such as a high strength-to-weight ratio, high ductility, and high durability presented by such alloys. However, the application of aluminum alloys in the WAAM process is still limited due to the fact that the gas pores and the coarse dendritic structure present during the WAAM process result in a severe loss of mechanical properties for aluminum alloy components [12, 160-162].

Related investigations have shown that lower heat inputs and faster cooling rates lead to a more equiaxed microstructure and fewer gas pores in the aluminum pieces produced by WAAM than what is observed with other processes [163].

The research efforts of (Ortega et al., 2019) [11] have shown that the melt viscosity decreases with increasing heat input, and consequently, soluble gas easily drops out of the weld pool, thus decreasing the gas porosities in the WAAM piece. However, they did not consider the fact that the dissolution of hydrogen in the melt increases significantly by increasing the heat of the aluminum melt [122, 164, 165].

The directional solidification of WAAM products means that a fair portion of their crystal structure consists of columnar dendrites, thus making their mechanical properties anisotropic. Anisotropy is directly related to the crystallographic texture, grain shape, and size development during directional column growth deposition [166, 167].

The purpose of this study is to investigate the effect of weld current intensity and heat input on the surface roughness of specimens made using GMAW-based WAAM and to examine their microstructure, porosity and mechanical properties.

## **4.2 Experimental procedure**

A Fronius TransPuls Synergic 4000 source and a Yaskawa Motoman MH6 robot were used for WAAM process. The experimental setup and schematic diagram of WAAM are shown in Figure 4.1.

An ER4043 welding wire with a 1.2 (mm) diameter and 38 (mm) × 9.5 (mm) × 300 (mm) 6061-T6 plates were selected as the feedstock and substrate in this study. The chemical compositions of ER4043 and 6061 are listed in Table 4.1, while the mechanical properties of ER4043 are presented in Table 4.2.

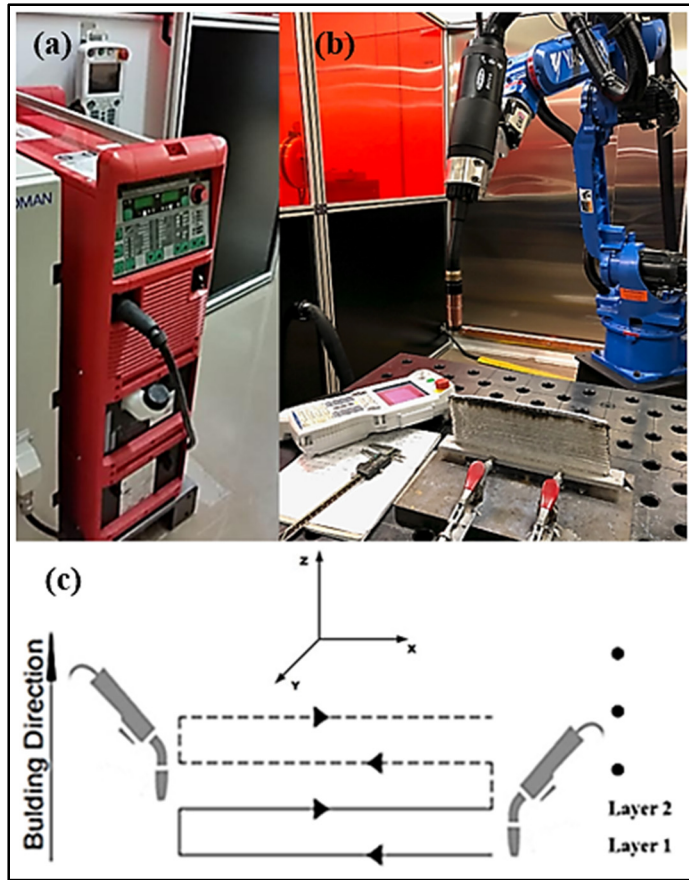


Figure 4.1 (a) Fronius TransPuls Synergic 4000; (b) Yaskawa Motoman MH6 robot arm; (c) Schematic diagram of WAAM process.

Table 4-1 Chemical compositions of ER4043 and 6061 alloy (wt.%)

	Al	Si	Mg	Fe	Cu
ER4043	Balance	4.50-6.00	0.05 max	0.80 max	0.30 max
6061	Balance	0.40-0.80	0.80-1.20	0.70 max	0.15-0.40

Table 4-2 Mechanical properties of ER4043

Ultimate Tensile Strength	Yield Strength	Percent Elongation in 2"
21,000 - 33,000 psi (144-227 MPa)	10,000 - 27,500 psi (69-190 MPa)	5 - 12%

In this study, two walls, named First wall and Second wall, were built layer-by-layer respectively with two different sets of welding parameters as listed in Table 4.3. The arc travel speed (TS), contact tip to work distance (CTWD), Argon gas flow rate, dynamic pulse correction (DYN) and welding voltage were kept the same for both sets. The welding current and the amount of heat input (H. I.) varied as a function of the wire feed speed (WFS).

Table 4-3 Welding parameters

	WFS (ipm)	TS (ipm)	CTWD (mm)	Argon (cfh)	DYN (%)	I <sub>avg.</sub> (Amp)	V <sub>avg.</sub> (V)	H.I. (kj/in)
First wall	275.6	48	14	40	-5	144	22.1	3.978
Second wall	305.9	48	14	40	-5	172	22.1	4.752

Before the first layer deposition, substrates were cleaned by a wire brush and rinsed with acetone, and after each layer was made, the layer surface was brushed to remove any aluminum oxide present. Once the temperature of previous layer cooled down to between 35–55°C the next one would then be added. Figure 4.2 and Table 4.4 show the appearance of the walls and their characteristics.

Table 4-4 Characteristics of the walls

	Number of layers	Length (mm)	Height (mm)	Width (mm)	Total weight (g)
First wall	108	254	101	6.64	472.45
Second wall	129	254	101	7.89	558.91

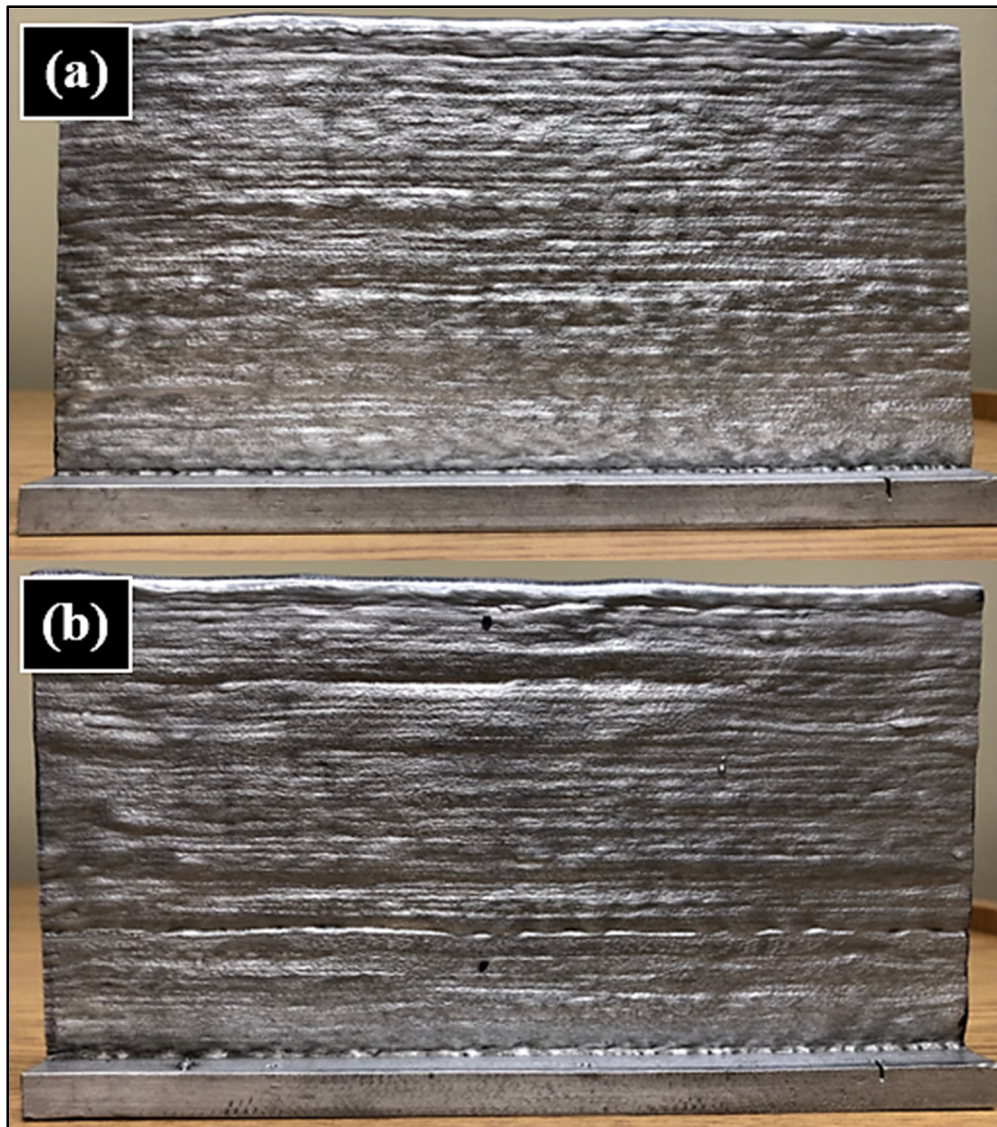


Figure 4.2 Photographs of the deposited walls: (a) First wall, (b) Second wall.

After the WAAM process was complete, the surface roughness was evaluated with a Mitutoyo surface roughness tester (SJ-410). Three lines on the surfaces of each wall were randomly selected (lines a, b, and c, each being 25 (mm) in length) to measure the surface roughness according to the wall height direction. The samples selection for microhardness, metallography analysis and tensile tests is indicated in Figure 4.3.

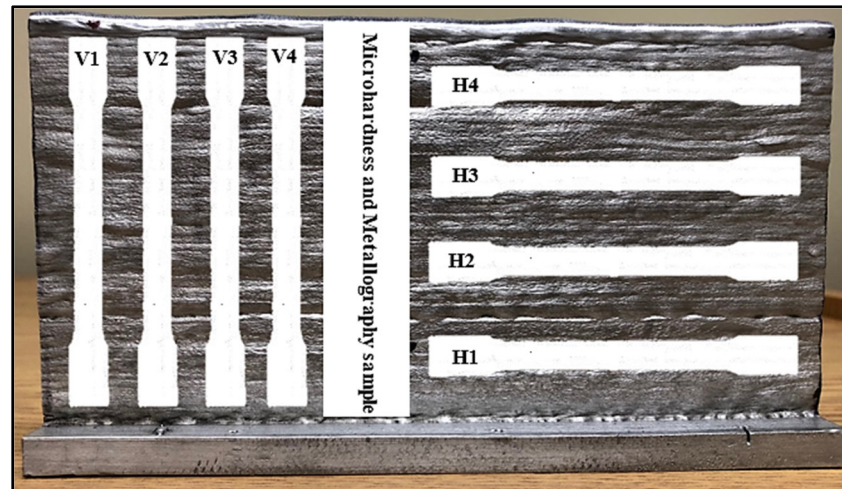


Figure 4.3 Position of samples.

For the metallography, microhardness and porosity analysis, samples were made from a strip as shown in Figure 4.3 selected from the central portion of each thin wall. For the microhardness tests, the cross-section of the sample was respectively polished with 400, 800, 1200, 1500 abrasive paper, and then polished with 3  $\mu\text{m}$  alumina suspensions. Each microhardness test with a 50 g load was performed for 15 seconds with the FM microhardness tester. Before metallography was performed with an optical microscope, the sample was etched for 7 seconds with 0.5% HF. For tensile tests, as shown in Figure 4, four horizontal and four vertical specimens for each wall were made based on ASTM E8 / E8M-09 [168], and then the experiments were carried out at a tensile rate of 1 mm per minute.

## 4.3 Results and Discussion

### 4.3.1 Surface quality and accuracy

An advantage of the WAAM method is its higher deposition rate as compared to other AM methods (50–130 g/min). However, the surface quality of the parts produced with the method is poor, and subsequent machining is usually required [169].

Figure 4.4 illustrates the surface roughness profiles for a, b, and c checked lines, and the surface roughness parameter values for each roughness profile are presented in table 4.5.

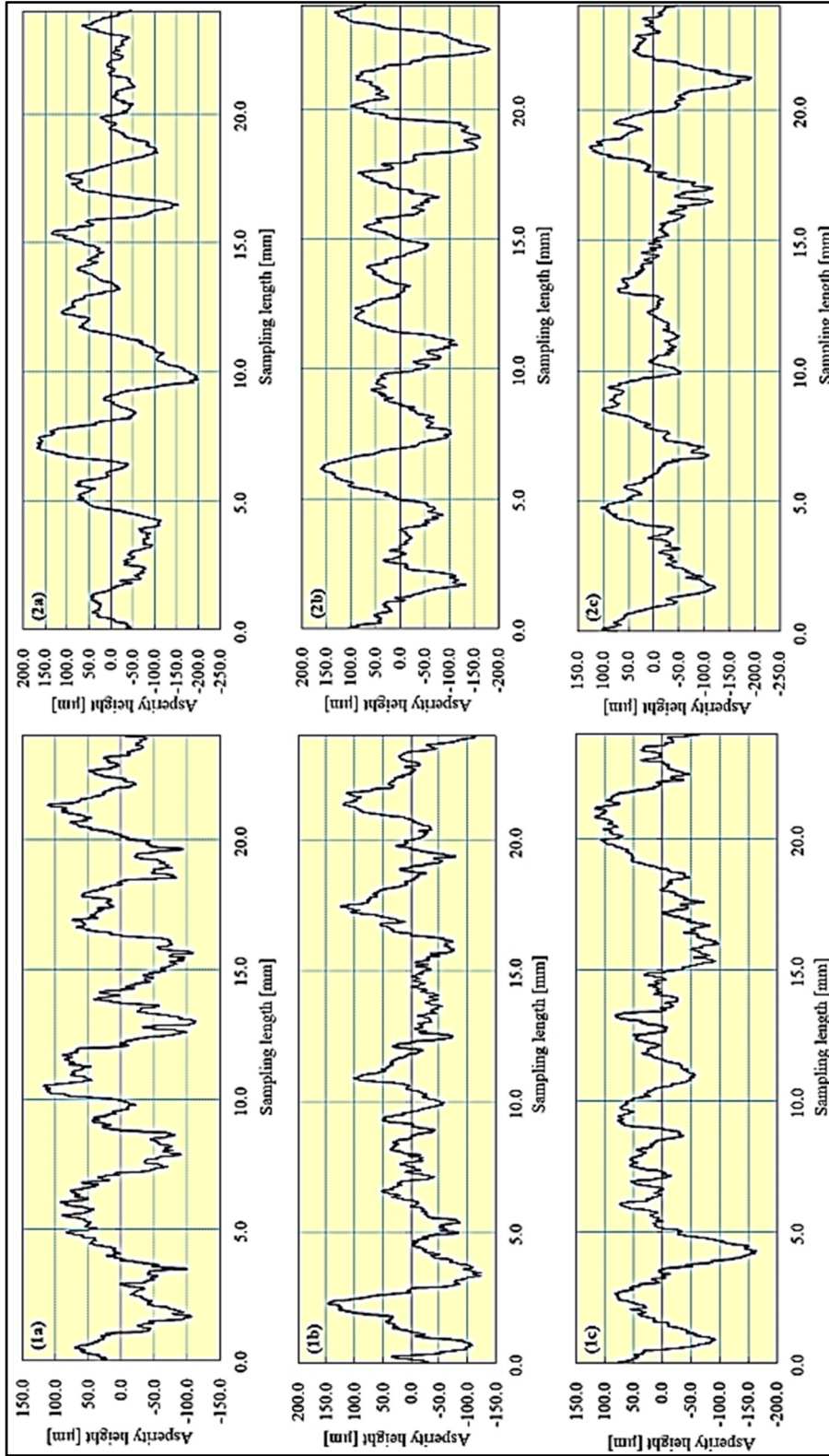


Figure 4.4 (1a), (1b), and (1c) First wall surface roughness profiles; (2a), (2b), and (2c) Second wall surface roughness profiles.

Table 4-5 Surface roughness parameters for each roughness profile

	(1a)	(1b)	(1c)	(2a)	(2b)	(2c)
$R_a$ ( $\mu\text{m}$ )	46.747	40.264	42.884	57.588	59.234	46.661
$R_q$ ( $\mu\text{m}$ )	53.669	50.882	53.582	71.220	70.578	57.644
$R_z$ ( $\mu\text{m}$ )	211.612	228.805	213.429	290.833	273.831	237.210

The surface roughness parameters, including the average roughness ( $R_a$ ), the root mean square (RMS) roughness ( $R_q$ ), and the maximum roughness profile ( $R_z$ ), are introduced in Figure 4.5.

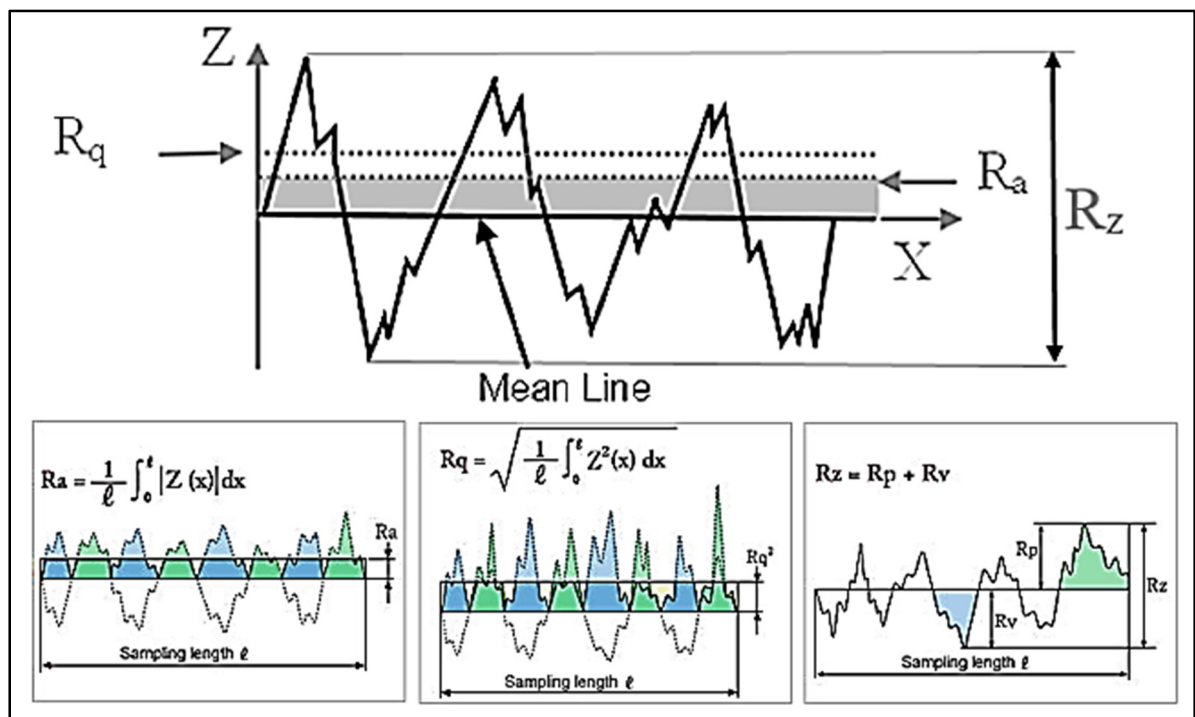


Figure 4.5 The roughness average ( $R_a$ ), the root mean square (RMS), the roughness ( $R_q$ ), and the maximum roughness profile height ( $R_z$ ).

Taken from Rubert<sup>8</sup> and Olympus<sup>9</sup>

<sup>8</sup> <http://www.rubert.co.uk/faqs/roughness-parameters/>

<sup>9</sup> <https://www.olympus-ims.com/en/metrology/surface-roughness-measurement-portal/parameters/>

According to the results, the surface waviness of the second wall is greater than that of the first wall. Therefore, it can be concluded that if the TS and voltage are kept constant during Gas Metal Arc Welding, then, as the WFS increases, the weld current will rise, and the heat input will consequently be boosted. In other words, the higher heat input generates a bigger and hotter weld pool in every layer of the second wall. As well, a higher weld current results in a greater arc force applied to the weld pool and will cause the weld pool to overflow. The roughness and waviness of the surfaces of the second wall are thus greater than those of the first wall, which has a lower weld current and smaller heat input.

#### **4.3.2 Microstructure and hardness**

The microstructure of the different sections (top and middle) of the first and second walls was examined by optical micrography as shown in Figure 4.6. Here, 1T and 2T are for the top section of the first wall and the second wall, respectively; and 1M and 2M are for the middle section of the first wall and the second wall, respectively. ImageJ software was used to measure the percentage of Al-Si eutectic phase. Results show that the amount of the Al-Si eutectic phase in 2T (39.47%) is greater than that in 1T (27.87%). Using the Al-Si phase diagram (Figure 4.7) and the lever rule, the chemical compositions of the first and second walls were measured as 95.33% Al - 4.67% Si and 94.06% Al - 5.94% Si, respectively.

Considering that the boiling points of the Al and Si elements are 2470°C and 3265°C, respectively, and assuming that the mass of silicon in both walls remains unchanged, the Al mass in the second wall will be 22.43% lower than that in the first wall. In other words, this amount of aluminum is lost due to evaporation caused by a higher weld current and heat input, for the second wall.

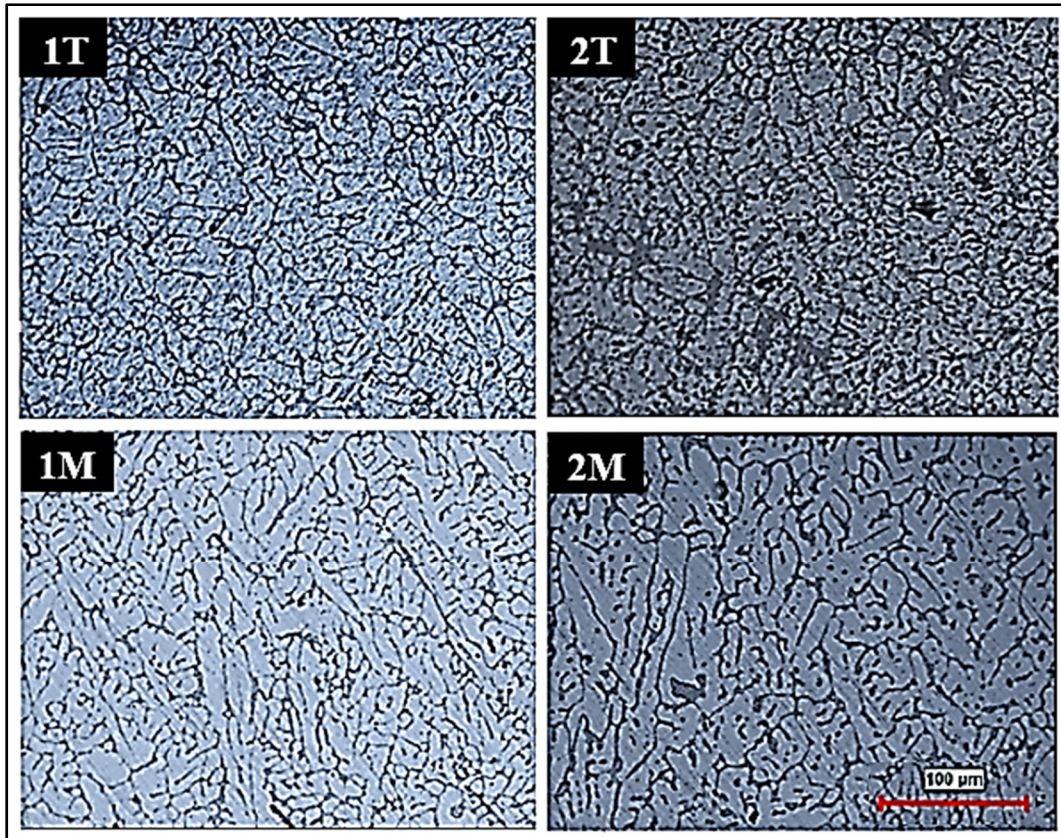


Figure 4.6 Metallography images of walls: 1T, 2T - top sections of first wall and second wall; 1M, 2M - middle sections of first wall and second wall.

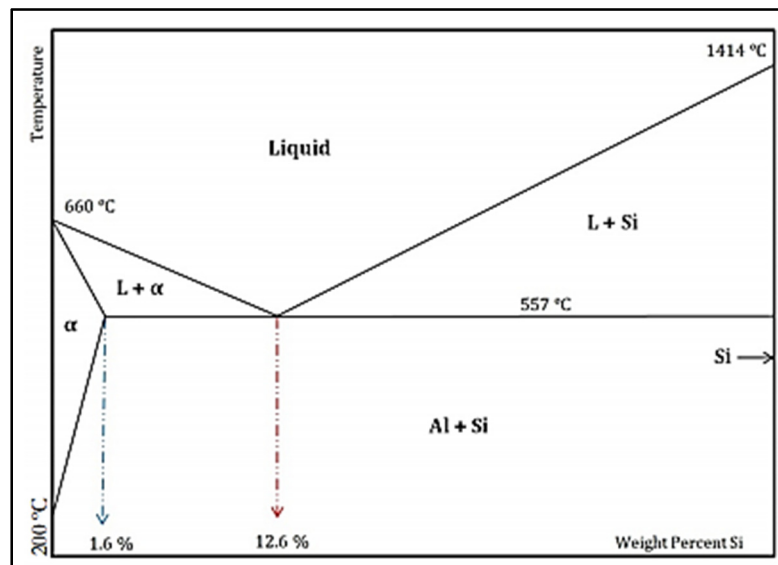


Figure 4.7 The Al-Si phase diagram.  
Taken from M. Zamani (2017, p. 5)

Table 4.6 shows the microhardness and grain size measured at a distance of 95 ( $\mu\text{m}$ ) from the top of the wall. As indicated, the grain size at the top of the second wall is slightly larger than that for the first wall, which could be due to the higher arc heat in the second wall.

According to the grain size results, the mean of hardness at the top of the second wall is expected to be lower than that for the first wall, but the results show that the hardness at the top of the second wall (51.17 HV) is greater than for the first wall (47.92 HV). This is due to the higher silicon percentage in the chemical composition of the second wall. In other words, the hardness results confirm that a portion of aluminum is fumed due to the high weld current and heat input.

Table 4-6 Microhardness and grain size at the top section of walls

Variable	Microhardness					Mean of grains size ( $\mu\text{m}$ )
	Number of values	Mean (HV)	Minimum (HV)	Maximum (HV)	Standard deviation	
First wall	32	47.92	39.58	52.31	3.120	14
Second wall	35	51.17	45.21	57.37	2.834	19

Table 4.7 shows the hardness and grain size for two width lines and a vertical line at the middle section of each wall. The hardness results show that, unlike in the top section of the walls, the hardness of the two walls in the middle section does not differ significantly. Given the average size of the dendrites (mean width size and longitudinal size of the dendrites), the second wall has the bigger size of dendrites (images 1M and 2M of Figure 4.6), which is due to the higher heat input, which leads more dendrites to grow. Thus, although it was predicted that the hardness would be higher at the middle section of the second wall than the first wall based on the hardness of the wall's top section and the percentage of silicon, hardness was reduced due to the bigger size of the dendrites. Consequently, the hardness of the second wall was roughly equivalent to that of the first wall.

Table 4-7 Microhardness test results and grain size at the middle section of walls

Variable	Microhardness					Mean of dendrites size	
	Number of values	Mean (HV)	Minimum (HV)	Maximum (HV)	Standard deviation	Width ( $\mu\text{m}$ )	Length ( $\mu\text{m}$ )
First wall width 1	40	45.41	31.45	50.61	3.431		
First wall width 2	40	44.43	33.01	49.45	4.346	15	24
First wall vertical	25	46.60	34.96	51.33	3.227		
Second wall width 1	56	44.56	31.21	51.94	3.924		
Second wall width 2	57	45.28	33.51	49.68	3.806	20	32
Second wall vertical	25	45.66	41.44	51.33	2.456		

### 4.3.3 Porosity

A porosity analysis for each wall at two equal surface positions (in the middle section) was performed using ImageJ software. Figure 4.8 shows a schematic diagram of the porosity density in the first and second walls. The porosity analysis results are summarized in Table 4.8.

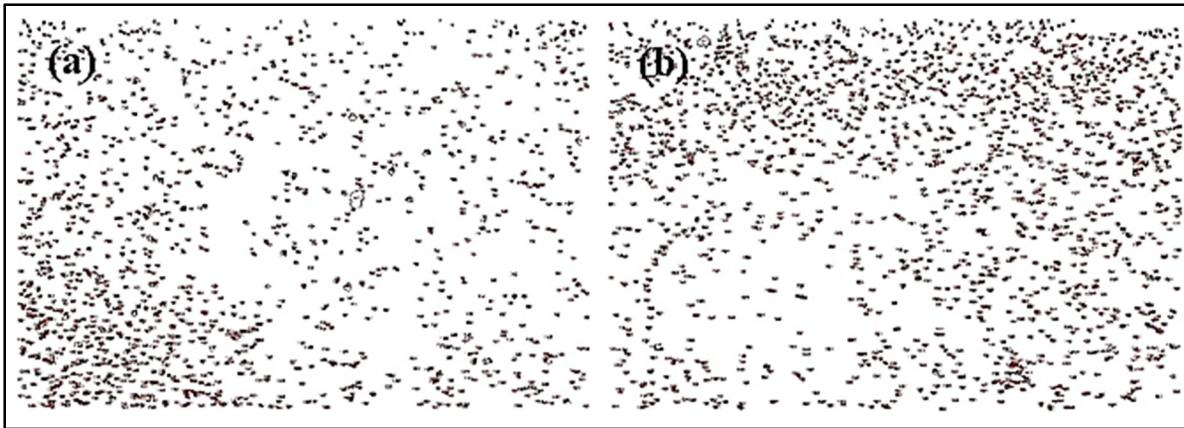


Figure 4.8 Images analyzed by ImageJ software: (a) first wall, (b) second wall.

Table 4-8 Summary of porosity analysis by ImageJ software

		Total number of porosities	Total area of porosities ( $\mu\text{m}^2$ )	Average size of porosities ( $\mu\text{m}$ )	Area of porosities to test area (%)
First wall	Surface 1	1515	12229.56	8.07	1.34
	Surface 2	1244	7852.12	6.32	0.86
Second wall	Surface 1	1964	15341.75	7.81	1.68
	Surface 2	1817	15665.68	8.62	1.71

The total number of porosities in two positions for each wall based on the diameters of the porosities is classified as presented in Table 4. 9, and each porosity size range is expressed as a percentage of the total number of porosities as depicted in Figures 4.9 and 4.10.

Table 4-9 Porosities classified based on their size and percentage

Diameter of porosity (µm)	First wall		Second wall	
	Number of porosities	Porosity percentage	Number of porosities	Porosity percentage
0-2.5	1817	65.9%	2020	53.4%
2.5-4.5	669	24.3%	1266	33.5%
4.5-6.5	191	6.9%	352	9.3%
6.5-8.5	42	1.5%	108	2.9%
8.5-10.5	18	0.7%	29	0.8%
10.5-12.5	14	0.5%	2	0.1%
12.5-14.5	4	0.1%	1	0.0%
14.5-16.5	1	0.0%	1	0.0%
16.5-18.5	0	0.0%	0	0.0%
18.5-20.5	1	0.0%	0	0.0%
20.5-22.5	0	0.0%	1	0.0%
22.5-24.5	0	0.0%	0	0.0%
24.5-26.5	0	0.0%	0	0.0%
26.5-28.5	0	0.0%	0	0.0%
28.5-30.5	0	0.0%	0	0.0%
30.5-32.5	1	0.0%	0	0.0%
More	0	0.0%	0	0.0%

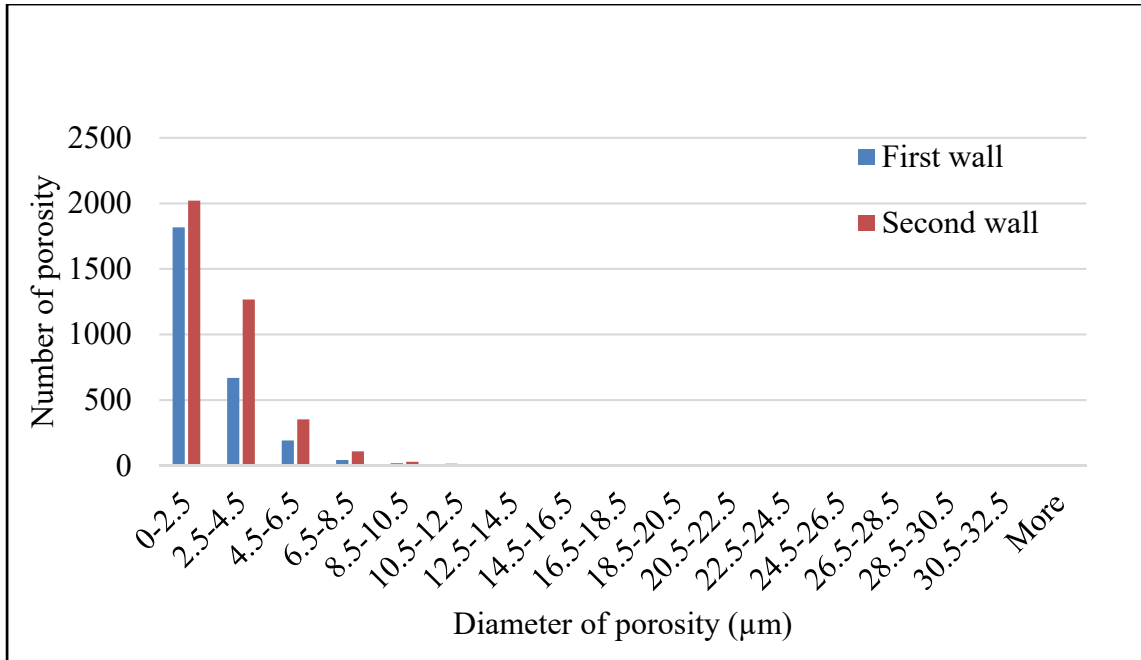


Figure 4.9 Graphical representation of the number of porosities for each size range.

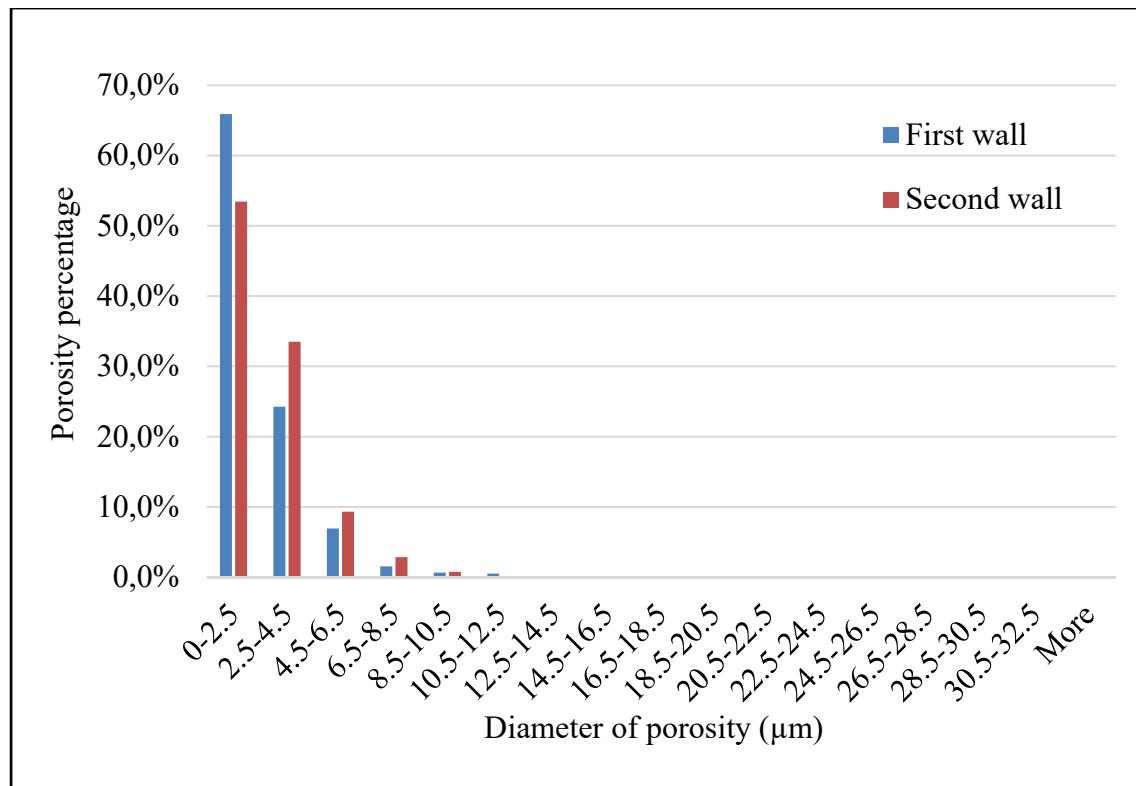


Figure 4.10 Graphical representation of the percentage of porosities for each size range.

Figure 4.9 shows that the number of porosities in all diameter regions is smaller in the first wall than that in the second wall. Therefore, as the heat input increases, so does the number of pores. The results in Figure 4.10 indicate that with lower heat input, the pores for the first wall are finer. In other words, when the heat input for the second wall was increased, not only did the number of pores increase, but some pores also adhered to each other, thereby increasing their diameter. This is due to the lower melt viscosity in the weld pool and the longer solidification time.

#### **4.3.4 Mechanical properties**

The tensile test was carried out on four specimens in the longitudinal direction (horizontal) and on four specimens in the wall height (vertical) direction for each wall. The results of the tests are summarized in Table 4.10.

Based on the chemical composition of the second wall, which had a higher silicon content than the first wall, it was expected that a higher tensile strength (UTS) would be achieved for the second wall. However, given the greater number of porosities and larger size of porosities in the second wall, as indicated in Table 4.10, there was no significant difference in the tensile test results between the first wall and the second wall. Noticeable on both walls was that the mechanical properties were superior in the horizontal direction than in the vertical direction. This was due to the columnar dendritic structure, and according to other sources [170-172], this is also due to the texture orientation in components made by the WAAM technique.

Table 4-10 Tensile test Results

Specimen position	Specimen number	First wall		Second wall	
		UTS (MPa)	Elongation (%)	UTS (MPa)	Elongation (%)
Horizontal	H1	159.21	13.15	155.64	14.75
	H2	161.39	16.72	156.83	17.90
	H3	157.17	13.05	154.19	13.60
	H4	158.32	13.43	152.83	11.11
Vertical	V1	132.40	7.37	133.66	7.27
	V2	143.54	8.06	132.20	7.95
	V3	140.80	8.86	140.85	8.49
	V4	136.45	7.40	132.84	5.76

#### 4.3.5 Conclusions

In this study, two thin walls made of ER4043 aluminum wire with a 3.978 (kJ/in) and 4.752 (kJ/in) heat input adjustments were made using the GMAW-based WAAM method. The following results were obtained by examining the walls:

- As the heat input increases, the wall width increases as well, but the weld layer heights decrease.
- Boosting the heat input increases the surface roughness of the wall.
- At higher heat inputs, some of the aluminum evaporates and the chemical composition of the alloy changes.
- A higher heat input increases the size of the dendrites. This eliminates the influence of changes in the chemical composition of the hardness of the walls and their tensile strength.
- The number and size of the gas pores increases with increasing heat input.
- Directional mechanical properties can be recognized on both walls, which depend on the walls' crystallographic texture.

## CONCLUSION

- The GMAW-P process can be used to manufacture aluminum pieces in the WAAM technique;
- The parameters that affect the GMAW-P process are adjustable with the DOE;
- Dynamic / Pulse Correction (DYN) is a parameter that regulates the frequency of the weld current. The percentage of DYN that was adjusted during the experiments significantly affected the surface quality, microstructure, and porosity of the specimens made by WAAM;
- Increasing the weld heat input can cause partial evaporation of aluminum and alter the chemical composition of the alloy;
- The adjustment of the weld heat input can control the thickness, surface roughness, microstructure, and porosity of the specimen;
- The mechanical properties of the manufactured specimens are influenced by heat input. Increasing the heat input leads to a greater heat treatment (tempering or annealing) of the microstructure.



## **RECOMMENDATIONS**

The use of an Al-Si alloy poses a challenge to the WAAM technique because of its high flowability. On the other hand, Al-Si alloys are not sensitive to hot cracking, which is one of the major issues in the WAAM technique. Therefore, it is recommended to conduct a similar study on other grades of Al alloys to investigate the effect of process parameters on the hot crack generated in specimens prepared by the WAAM technique.



## LIST OF BIBLIOGRAPHICAL REFERENCES

- [1] *Additive manufacturing - General principles - Terminology (ISO/ASTM 52900:2015)* 2015.
- [2] T. J. Horn and O. L. Harrysson, "Overview of current additive manufacturing technologies and selected applications," *Science progress*, vol. 95, no. 3, pp. 255-282, 2012.
- [3] C. DOE, "Quadrennial Technology Review 2015—Chapter 6: Innovating Clean Energy Technologies in Advanced Manufacturing—Composite materials," ed, 2015.
- [4] R. Huang *et al.*, "Energy and emissions saving potential of additive manufacturing: the case of lightweight aircraft components," *Journal of Cleaner Production*, vol. 135, pp. 1559-1570, 2016.
- [5] A. Totin, E. MacDonald, and B. P. Conner, "Additive Manufacturing for Aerospace Maintenance and Sustainment (Postprint)," Youngstown State University Youngstown United States 2019.
- [6] K. Derekar, "A review of wire arc additive manufacturing and advances in wire arc additive manufacturing of aluminium," *Materials Science and Technology*, vol. 34, no. 8, pp. 895-916, 2018.
- [7] H. Li and J. Norrish, "Arc Welding Processes for Additive Manufacturing: A Review," *Transactions on Intelligent Welding Manufacturing: Volume I No. 1 2017*, p. 3, 2017.
- [8] M. A. Jackson, A. Van Asten, J. D. Morrow, S. Min, and F. E. Pfefferkorn, "A comparison of energy consumption in wire-based and powder-based additive-subtractive manufacturing," *Procedia Manufacturing*, vol. 5, pp. 989-1005, 2016.
- [9] A. Ermakova, A. Mehmanparast, and S. Ganguly, "A review of present status and challenges of using additive manufacturing technology for offshore wind applications," *Procedia Structural Integrity*, vol. 17, pp. 29-36, 2019.
- [10] S. Williams and F. Martina, "Wire+ arc additive manufacturing vs. traditional machining from solid: a cost comparison," Technical report. Welding Engineering and Laser Processing Centre, Cranfield, 2015.

- [11] A. G. Ortega *et al.*, "Characterisation of 4043 aluminium alloy deposits obtained by wire and arc additive manufacturing using a Cold Metal Transfer process," *Science and Technology of Welding and Joining*, pp. 1-10, 2019.
- [12] J. Gu, B. Cong, J. Ding, S. W. Williams, and Y. Zhai, "Wire+ arc additive manufacturing of aluminium," in *Proceedings of the 25th Annual International Solid Freeform Fabrication Symposium, Austin, TX, USA*, 2014, pp. 4-6.
- [13] F. Li, S. Chen, J. Shi, Y. Zhao, and H. Tian, "Thermoelectric cooling-aided bead geometry regulation in wire and arc-based additive manufacturing of thin-walled structures," *Applied Sciences*, vol. 8, no. 2, p. 207, 2018.
- [14] X. Shi *et al.*, "Selective laser melting-wire arc additive manufacturing hybrid fabrication of Ti-6Al-4V alloy: Microstructure and mechanical properties," *Materials Science and Engineering: A*, vol. 684, pp. 196-204, 2017.
- [15] Z. Li *et al.*, "Reducing arc heat input and obtaining equiaxed grains by hot-wire method during arc additive manufacturing titanium alloy," *Materials Science and Engineering: A*, vol. 742, pp. 287-294, 2019.
- [16] B. Wu, "Quality improvement in wire arc additive manufacturing," 2018.
- [17] B. Wu *et al.*, "Mitigation of thermal distortion in wire arc additively manufactured Ti6Al4V part using active interpass cooling," *Science and Technology of Welding and Joining*, vol. 24, no. 5, pp. 484-494, 2019.
- [18] B. Wu *et al.*, "Effects of heat accumulation on the arc characteristics and metal transfer behavior in Wire Arc Additive Manufacturing of Ti6Al4V," *Journal of Materials Processing Technology*, vol. 250, pp. 304-312, 2017.
- [19] P. A. Colegrove, J. Donoghue, F. Martina, J. Gu, P. Prangnell, and J. Hönnige, "Application of bulk deformation methods for microstructural and material property improvement and residual stress and distortion control in additively manufactured components," *Scripta Materialia*, vol. 135, pp. 111-118, 2017.
- [20] P. A. Colegrove *et al.*, "High pressure interpass rolling of wire+ arc additively manufactured titanium components," in *Advanced Materials Research*, 2014, vol. 996, pp. 694-700: Trans Tech Publ.
- [21] A. R. McAndrew *et al.*, "Interpass rolling of Ti-6Al-4V wire+ arc additively manufactured features for microstructural refinement," *Additive Manufacturing*, vol. 21, pp. 340-349, 2018.

- [22] F. Ning, "Microstructure and mechanical property of TiB reinforced Ti matrix composites fabricated by ultrasonic vibration-assisted laser engineered net shaping," *Rapid Prototyping Journal*, vol. 25, no. 3, pp. 581-591, 2019.
- [23] H. H. E. Park, "Visuai-JW~@~® OSAKA UNIVERSITY," 2016.
- [24] A. Gomez Ortega, L. Corona Galvan, F. Deschaux-Beaume, B. Mezrag, and S. Rouquette, "Effect of process parameters on the quality of aluminium alloy Al5Si deposits in wire and arc additive manufacturing using a cold metal transfer process," *Science and Technology of Welding and Joining*, vol. 23, no. 4, pp. 316-332, 2018.
- [25] L. Wahsh *et al.*, "Parameter Selection for Wire Arc Additive Manufacturing (WAAM) Process," 2018.
- [26] C. B. Kumar and V. Anandkrishnan, "Experimental investigations on the effect of wire arc additive manufacturing process parameters on the layer geometry of Inconel 825," *Materials Today: Proceedings*, 2019.
- [27] R. Kleer and F. T. Piller, "Local manufacturing and structural shifts in competition: Market dynamics of additive manufacturing," *International Journal of Production Economics*, vol. 216, pp. 23-34, 2019.
- [28] A. R. Catalano, V. Lunetto, P. C. Priarone, and L. Settineri, "A Survey on Energy Efficiency in Metal Wire Deposition Processes," in *International Conference on Sustainable Design and Manufacturing*, 2019, pp. 311-322: Springer.
- [29] G. Escobar-Palafox, "Robotic manufacturing by shaped metal deposition: state of the art," *Industrial Robot: An International Journal*, vol. 38, no. 6, pp. 622-628, 2011.
- [30] A. A. Ugla, O. Yilmaz, and A. R. Almusawi, "Development and control of shaped metal deposition process using tungsten inert gas arc heat source in additive layered manufacturing," *Proceedings of the Institution of Mechanical Engineers, Part B: Journal of Engineering Manufacture*, vol. 232, no. 9, pp. 1628-1641, 2018.
- [31] S. Reddy *et al.*, "A new approach for attaining uniform properties in build direction in additive manufactured components through coupled thermal-hardness model," *Journal of Manufacturing Processes*, vol. 40, pp. 46-58, 2019.
- [32] A. A. Ugla, H. J. Khaudair, and A. R. Almusawi, "Metal Inert Gas Welding-Based-Shaped Metal Deposition in Additive Layered Manufacturing: A," *World Academy of Science, Engineering and Technology International Journal of Mechanical and Materials Engineering*, vol. 13, p. 14, 2019.

- [33] S. W. Williams, F. Martina, A. C. Addison, J. Ding, G. Pardal, and P. Colegrove, "Wire+ arc additive manufacturing," *Materials Science and Technology*, vol. 32, no. 7, pp. 641-647, 2016.
- [34] A. Paskual, P. Álvarez, and A. Suárez, "Study on arc welding processes for high deposition rate additive manufacturing," *Procedia Cirp*, vol. 68, pp. 358-362, 2018.
- [35] T. DebRoy *et al.*, "Additive manufacturing of metallic components—process, structure and properties," *Progress in Materials Science*, vol. 92, pp. 112-224, 2018.
- [36] B. Wu *et al.*, "A review of the wire arc additive manufacturing of metals: properties, defects and quality improvement," *Journal of Manufacturing Processes*, vol. 35, pp. 127-139, 2018.
- [37] A. Shirizly and O. Dolev, "From Wire to Seamless Flow-Formed Tube: Leveraging the Combination of Wire Arc Additive Manufacturing and Metal Forming," *JOM*, vol. 71, no. 2, pp. 709-717, 2019.
- [38] A. Waqas, X. Qin, J. Xiong, H. Wang, and C. Zheng, "Optimization of Process Parameters to Improve the Effective Area of Deposition in GMAW-Based Additive Manufacturing and its Mechanical and Microstructural Analysis," *Metals*, vol. 9, no. 7, p. 775, 2019.
- [39] W. Liu, C. Jia, M. Guo, J. Gao, and C. Wu, "Compulsively constricted WAAM with arc plasma and droplets ejected from a narrow space," *Additive Manufacturing*, vol. 27, pp. 109-117, 2019.
- [40] J. Xiong, Y. Li, R. Li, and Z. Yin, "Influences of process parameters on surface roughness of multi-layer single-pass thin-walled parts in GMAW-based additive manufacturing," *Journal of Materials Processing Technology*, vol. 252, pp. 128-136, 2018.
- [41] L. Wang, J. Xue, and Q. Wang, "Correlation between arc mode, microstructure, and mechanical properties during wire arc additive manufacturing of 316L stainless steel," *Materials Science and Engineering: A*, vol. 751, pp. 183-190, 2019.
- [42] W. Wu, J. Xue, L. Wang, Z. Zhang, Y. Hu, and C. Dong, "Forming Process, Microstructure, and Mechanical Properties of Thin-Walled 316L Stainless Steel Using Speed-Cold-Welding Additive Manufacturing," *Metals*, vol. 9, no. 1, p. 109, 2019.

- [43] N. Rodriguez, L. Vázquez, I. Huarte, E. Arruti, I. Taberero, and P. Alvarez, "Wire and arc additive manufacturing: a comparison between CMT and TopTIG processes applied to stainless steel," *Welding in the World*, vol. 62, no. 5, pp. 1083-1096, 2018.
- [44] J. Näsström, F. Brueckner, and A. F. Kaplan, "Laser enhancement of wire arc additive manufacturing," *Journal of Laser Applications*, vol. 31, no. 2, p. 022307, 2019.
- [45] J. Rodriguez, K. Hoefler, A. Haelsing, and P. Mayr, "Functionally Graded SS 316L to Ni-Based Structures Produced by 3D Plasma Metal Deposition," *Metals*, vol. 9, no. 6, p. 620, 2019.
- [46] F. Martina, J. Ding, S. Williams, A. Caballero, G. Pardal, and L. Quintino, "Tandem metal inert gas process for high productivity wire arc additive manufacturing in stainless steel," *Additive Manufacturing*, vol. 25, pp. 545-550, 2019.
- [47] A. Caballero, J. Ding, S. Ganguly, and S. Williams, "Wire+ Arc Additive Manufacture of 17-4 PH stainless steel: Effect of different processing conditions on microstructure, hardness, and tensile strength," *Journal of Materials Processing Technology*, vol. 268, pp. 54-62, 2019.
- [48] X. Zhang *et al.*, "Microstructure and mechanical properties of TOP-TIG-wire and arc additive manufactured super duplex stainless steel (ER2594)," *Materials Science and Engineering: A*, p. 138097, 2019.
- [49] D. Arun, K. D. Ramkumar, and R. Vimala, "Multi-pass arc welding techniques of 12 mm thick super-duplex stainless steel," *Journal of Materials Processing Technology*, vol. 271, pp. 126-143, 2019.
- [50] T. A. Rodrigues, V. Duarte, J. A. Avila, T. G. Santos, R. Miranda, and J. Oliveira, "Wire and arc additive manufacturing of HSLA steel: Effect of thermal cycles on microstructure and mechanical properties," *Additive Manufacturing*, vol. 27, pp. 440-450, 2019.
- [51] K. P. Prajadhama *et al.*, "Development of Bead Modelling for Distortion Analysis Induced by Wire Arc Additive Manufacturing using FEM and Experiment," in *MATEC Web of Conferences*, 2019, vol. 269, p. 05003: EDP Sciences.
- [52] S. Jhavar, C. P. Paul, and N. K. Jain, "Micro-plasma transferred arc additive manufacturing for die and mold surface remanufacturing," *JOM*, vol. 68, no. 7, pp. 1801-1809, 2016.

- [53] Y. Ali, P. Henckell, J. Hildebrand, J. Reimann, J. Bergmann, and S. Barnikol-Oettler, "Wire arc additive manufacturing of hot work tool steel with CMT process," *Journal of Materials Processing Technology*, vol. 269, pp. 109-116, 2019.
- [54] R. Sun *et al.*, "Microstructure, residual stress and tensile properties control of wire-arc additive manufactured 2319 aluminum alloy with laser shock peening," *Journal of Alloys and Compounds*, vol. 747, pp. 255-265, 2018.
- [55] L. Zhu, Y. Luo, J. Han, C. Zhang, J. Xu, and D. Chen, "Energy characteristics of droplet transfer in wire-arc additive manufacturing based on the analysis of arc signals," *Measurement*, vol. 134, pp. 804-813, 2019.
- [56] M. Köhler, S. Fiebig, J. Hensel, and K. Dilger, "Wire and Arc Additive Manufacturing of Aluminum Components," *Metals*, vol. 9, no. 5, p. 608, 2019.
- [57] K. Derekar, J. Lawrence, G. Melton, A. Addison, X. Zhang, and L. Xu, "Influence of Interpass Temperature on Wire Arc Additive Manufacturing (WAAM) of Aluminium Alloy Components," in *MATEC Web of Conferences*, 2019, vol. 269, p. 05001: EDP Sciences.
- [58] C. Shen *et al.*, "Neutron diffraction residual stress determinations in Fe<sub>3</sub>Al based iron aluminide components fabricated using wire-arc additive manufacturing (WAAM)," *Additive Manufacturing*, 2019.
- [59] J. Wang, Z. Pan, L. Wei, S. He, D. Cuiuri, and H. Li, "Introduction of ternary alloying element in wire arc additive manufacturing of titanium aluminide intermetallic," *Additive Manufacturing*, vol. 27, pp. 236-245, 2019.
- [60] A. Ho, H. Zhao, J. W. Fellowes, F. Martina, A. E. Davis, and P. B. Prangnell, "On the origin of microstructural banding in Ti-6Al4V wire-arc based high deposition rate additive manufacturing," *Acta Materialia*, vol. 166, pp. 306-323, 2019.
- [61] P. Dryburgh *et al.*, "Spatially resolved acoustic spectroscopy for integrity assessment in wire-arc additive manufacturing," *Additive Manufacturing*, vol. 28, pp. 236-251, 2019.
- [62] J. Lin *et al.*, "Microstructural evolution and mechanical properties of Ti-6Al-4V wall deposited by pulsed plasma arc additive manufacturing," *Materials & Design*, vol. 102, pp. 30-40, 2016.

- [63] O. Marenych, A. Kostryzhev, C. Shen, Z. Pan, H. Li, and S. van Duin, "Precipitation Strengthening in Ni–Cu Alloys Fabricated Using Wire Arc Additive Manufacturing Technology," *Metals*, vol. 9, no. 1, p. 105, 2019.
- [64] J. Wang, Z. Pan, G. Yang, J. Han, X. Chen, and H. Li, "Location dependence of microstructure, phase transformation temperature and mechanical properties on Ni-rich NiTi alloy fabricated by wire arc additive manufacturing," *Materials Science and Engineering: A*, vol. 749, pp. 218-222, 2019.
- [65] J. Wang, Z. Pan, D. Cuiuri, and H. Li, "Phase constituent control and correlated properties of titanium aluminide intermetallic alloys through dual-wire arc additive manufacturing," *Materials Letters*, vol. 242, pp. 111-114, 2019.
- [66] I. Jurić, I. Garašić, M. Bušić, and Z. Kožuh, "Influence of Shielding Gas Composition on Structure and Mechanical Properties of Wire and Arc Additive Manufactured Inconel 625," *JOM*, vol. 71, no. 2, pp. 703-708, 2019.
- [67] M. Dinovitzer, X. Chen, J. Laliberte, X. Huang, and H. Frei, "Effect of wire and arc additive manufacturing (WAAM) process parameters on bead geometry and microstructure," *Additive Manufacturing*, vol. 26, pp. 138-146, 2019.
- [68] S. A. Vendan, L. Gao, A. Garg, P. Kavitha, G. Dhivyasri, and S. Rahul, "Welding an Overview," in *Interdisciplinary Treatment to Arc Welding Power Sources*: Springer, 2019, pp. 1-14.
- [69] T. Opderbecke and S. Guiheux, "TOPTIG: robotic TIG welding with integrated wire feeder," *Welding International*, vol. 23, no. 7, pp. 523-529, 2009.
- [70] A. L. WELDING, "TOPTIG, A new robot welding process for industry," p. 12 Available: <http://files.engineering.com/download.aspx?folder=f9d6f4ee-eb78-4cc3-8ded-984cb16af90c&file=TOPTIG.pdf>
- [71] J. Metcalfe and M. Quigley, "Keyhole stability in plasma arc welding," *Welding Journal*, vol. 54, no. 11, p. 401, 1975.
- [72] Z. Pan, D. Ding, B. Wu, D. Cuiuri, H. Li, and J. Norrish, "Arc welding processes for additive manufacturing: a review," in *Transactions on Intelligent Welding Manufacturing*: Springer, 2018, pp. 3-24.
- [73] J. N. Stavinoha, *Investigation of plasma arc welding as a method for the additive manufacturing of titanium-(6) aluminum-(4) vanadium alloy components*. Montana Tech of The University of Montana, 2012.

- [74] Y. Feng, B. Zhan, J. He, and K. Wang, "The double-wire feed and plasma arc additive manufacturing process for deposition in Cr-Ni stainless steel," *Journal of Materials Processing Technology*, vol. 259, pp. 206-215, 2018.
- [75] N. Huft, "Investigation of Multiple Torch PAW-Based Additive Manufacturing," 2019.
- [76] M. Singla, D. Singh, and D. Deepak, "Parametric optimization of gas metal arc welding processes by using factorial design approach," *Journal of Minerals and Materials Characterization and Engineering*, vol. 9, no. 04, p. 353, 2010.
- [77] T. A. Rodrigues, V. Duarte, R. Miranda, T. G. Santos, and J. Oliveira, "Current Status and Perspectives on Wire and Arc Additive Manufacturing (WAAM)," *Materials*, vol. 12, no. 7, p. 1121, 2019.
- [78] J. Z. Li, M. R. Alkahari, N. A. B. Rosli, R. Hasan, M. N. Sudin, and F. R. Ramli, "Review of Wire Arc Additive Manufacturing for 3D Metal Printing," *International Journal of Automation Technology*, vol. 13, no. 3, pp. 346-353, 2019.
- [79] K. Skrzyniecki, A. Kolasa, and P. Cegielski, "Study of static and dynamic characteristics of welding power source-arc systems," *Welding International*, vol. 29, no. 11, pp. 865-867, 2015.
- [80] J. Prado-Cerqueira, J. Diéguez, and A. Camacho, "Preliminary development of a Wire and Arc Additive Manufacturing system (WAAM)," *Procedia Manufacturing*, vol. 13, pp. 895-902, 2017.
- [81] C. G. Pickin, S. W. Williams, and M. Lunt, "Characterisation of the cold metal transfer (CMT) process and its application for low dilution cladding," *Journal of Materials Processing Technology*, vol. 211, no. 3, pp. 496-502, 2011.
- [82] S. Bagehorn, J. Wehr, and H. Maier, "Application of mechanical surface finishing processes for roughness reduction and fatigue improvement of additively manufactured Ti-6Al-4V parts," *International Journal of Fatigue*, vol. 102, pp. 135-142, 2017.
- [83] A. Simar, S. Godet, and T. R. Watkins, "Highlights of the special issue on metal additive manufacturing," ed: Elsevier, 2018.
- [84] Y. Yehorov, L. J. da Silva, and A. Scotti, "Balancing WAAM Production Costs and Wall Surface Quality through Parameter Selection: A Case Study of an Al-Mg5 Alloy Multilayer-Non-Oscillated Single Pass Wall," *Journal of Manufacturing and Materials Processing*, vol. 3, no. 2, p. 32, 2019.

- [85] Y. Guo, H. Pan, L. Ren, and G. Quan, "Microstructure and mechanical properties of wire arc additively manufactured AZ80M magnesium alloy," *Materials Letters*, vol. 247, pp. 4-6, 2019.
- [86] M. Bermingham, D. StJohn, J. Krynen, S. Tedman-Jones, and M. Dargusch, "Promoting the columnar to equiaxed transition and grain refinement of titanium alloys during additive manufacturing," *Acta Materialia*, vol. 168, pp. 261-274, 2019.
- [87] G. Marinelli, F. Martina, S. Ganguly, and S. Williams, "Microstructure, hardness and mechanical properties of two different unalloyed tantalum wires deposited via wire+ arc additive manufacture," *International Journal of Refractory Metals and Hard Materials*, p. 104974, 2019.
- [88] B. Cong, J. Ding, and S. Williams, "Effect of arc mode in cold metal transfer process on porosity of additively manufactured Al-6.3% Cu alloy," *The International Journal of Advanced Manufacturing Technology*, vol. 76, no. 9-12, pp. 1593-1606, 2015.
- [89] J. Guo, Y. Zhou, C. Liu, Q. Wu, X. Chen, and J. Lu, "Wire arc additive manufacturing of AZ31 magnesium alloy: Grain refinement by adjusting pulse frequency," *Materials*, vol. 9, no. 10, p. 823, 2016.
- [90] C. Zhang, Y. Li, M. Gao, and X. Zeng, "Wire arc additive manufacturing of Al-6Mg alloy using variable polarity cold metal transfer arc as power source," *Materials Science and Engineering: A*, vol. 711, pp. 415-423, 2018.
- [91] C. Zhang, M. Gao, and X. Zeng, "Workpiece vibration augmented wire arc additive manufacturing of high strength aluminum alloy," *Journal of Materials Processing Technology*, vol. 271, pp. 85-92, 2019.
- [92] C. Li, Z. Liu, X. Fang, and Y. Guo, "Residual stress in metal additive manufacturing," *Procedia Cirp*, vol. 71, pp. 348-353, 2018.
- [93] J. Ding, P. Colegrove, J. Mehnert, S. Williams, F. Wang, and P. S. Almeida, "A computationally efficient finite element model of wire and arc additive manufacture," *The International Journal of Advanced Manufacturing Technology*, vol. 70, no. 1-4, pp. 227-236, 2014.
- [94] P. A. Colegrove *et al.*, "Microstructure and residual stress improvement in wire and arc additively manufactured parts through high-pressure rolling," *Journal of Materials Processing Technology*, vol. 213, no. 10, pp. 1782-1791, 2013.

- [95] M. Roy, S. Williams, P. Colegrove, S. Ganguly, and J. Hönnige, "Residual Stress Characterization and Control in the Additive Manufacture of Large Scale Metal Structures," *Materials Research Proceedings*, vol. 2.
- [96] P. Withers, "Residual stress and its role in failure," *Reports on progress in physics*, vol. 70, no. 12, p. 2211, 2007.
- [97] K. Kirkhope, R. Bell, L. Caron, R. Basu, and K.-T. Ma, "Weld detail fatigue life improvement techniques. Part 1," *Marine structures*, vol. 12, no. 6, pp. 447-474, 1999.
- [98] J. Hönnige *et al.*, "Residual stress and texture control in Ti-6Al-4V wire+ arc additively manufactured intersections by stress relief and rolling," *Materials & Design*, vol. 150, pp. 193-205, 2018.
- [99] S. Ford and M. Despeisse, "Additive manufacturing and sustainability: an exploratory study of the advantages and challenges," *Journal of Cleaner Production*, vol. 137, pp. 1573-1587, 2016.
- [100] K. Derekar, "A review of wire arc additive manufacturing and advances in wire arc additive manufacturing of aluminium," *Materials Science and Technology*, pp. 1-22, 2018.
- [101] *Standard Terminology for Additive Manufacturing – General Principles – Terminology*, 2015.
- [102] S. W. Williams, F. Martina, A. C. Addison, J. Ding, G. Pardal, and P. Colegrove, "Wire + Arc Additive Manufacturing," *Materials Science and Technology*, vol. 32, no. 7, pp. 641-647, 2016.
- [103] S. Kou, "Welding metallurgy," *New Jersey, USA*, pp. 431-446, 2003.
- [104] D. Ding, Z. Pan, D. Cuiuri, and H. Li, "Wire-feed additive manufacturing of metal components: technologies, developments and future interests," *The International Journal of Advanced Manufacturing Technology*, vol. 81, no. 1-4, pp. 465-481, 2015.
- [105] P. Palani and N. Murugan, "Selection of parameters of pulsed current gas metal arc welding," *Journal of Materials Processing Technology*, vol. 172, no. 1, pp. 1-10, 2006.
- [106] E. F. da Silva, J. Rubens, A. Scotti, and J. C. de Oliveira, "Power quality analysis of gas metal ARC welding process operating under different drop transfer modes," in *Power Electronics Conference (COBEP), 2011 Brazilian*, 2011, pp. 129-135: IEEE.

- [107] T. Kurşun, "Effect of the GMAW and the GMAW-P welding processes on microstructure, hardness, tensile and impact strength of AISI 1030 steel joints fabricated by ASP316L austenitic stainless steel filler metal," *Archives of Metallurgy and Materials*, vol. 56, no. 4, pp. 955-963, 2011.
- [108] L. O. Vilarinho and A. Scotti, "An alternative algorithm for synergic pulsed GMAW of aluminium," *Australasian Welding Journal*, vol. 45, no. 2, pp. 36-44, 2000.
- [109] A. Joseph, D. Farson, D. Harwig, and R. Richardson, "Influence of GMAW-P current waveforms on heat input and weld bead shape," *Science and Technology of Welding and Joining*, vol. 10, no. 3, pp. 311-318, 2005.
- [110] P. Praveen, P. Yarlagadda, and M.-J. Kang, "Advancements in pulse gas metal arc welding," *Journal of Materials Processing Technology*, vol. 164, pp. 1113-1119, 2005.
- [111] P. Praveen and P. Yarlagadda, "Meeting challenges in welding of aluminum alloys through pulse gas metal arc welding," *Journal of Materials Processing Technology*, vol. 164, pp. 1106-1112, 2005.
- [112] J. Gu, J. Ding, S. W. Williams, H. Gu, P. Ma, and Y. Zhai, "The effect of inter-layer cold working and post-deposition heat treatment on porosity in additively manufactured aluminum alloys," *Journal of Materials Processing Technology*, vol. 230, pp. 26-34, 2016.
- [113] P. Lee and J. Hunt, "Hydrogen porosity in directional solidified aluminium-copper alloys: in situ observation," *Acta Materialia*, vol. 45, no. 10, pp. 4155-4169, 1997.
- [114] V. Goyal, P. Ghosh, and J. Saini, "Process-controlled microstructure and cast morphology of dendrite in pulsed-current gas-metal arc weld deposits of aluminum and Al-Mg alloy," *Metallurgical and Materials Transactions A*, vol. 38, no. 8, pp. 1794-1805, 2007.
- [115] G. M. Reddy, A. A. Gokhale, and K. P. Rao, "Weld microstructure refinement in a 1441 grade aluminium-lithium alloy," *Journal of Materials Science*, vol. 32, no. 15, pp. 4117-4126, 1997.
- [116] F. Wang, S. Williams, and M. Rush, "Morphology investigation on direct current pulsed gas tungsten arc welded additive layer manufactured Ti6Al4V alloy," *The international journal of advanced manufacturing technology*, vol. 57, no. 5-8, pp. 597-603, 2011.

- [117] C. Cunningham, J. Flynn, A. Shokrani, V. Dhokia, and S. Newman, "Invited Review Article: Strategies and Processes for High Quality Wire Arc Additive Manufacturing," *Additive Manufacturing*, 2018.
- [118] C. Favi, F. Campi, and M. Germani, "Comparative life cycle assessment of metal arc welding technologies by using engineering design documentation," *The International Journal of Life Cycle Assessment*, pp. 1-33, 2019.
- [119] M. Raval, S. Shah, and G. Acharya, "Optimization of Pulsed Gas Metal Arc Welding Parameters for Fabrication of Austenitic Stainless Steel," 2017.
- [120] J.-Y. Shim, J.-W. Zhang, H.-Y. Yoon, B.-Y. Kang, and I.-S. Kim, "Prediction model for bead reinforcement area in automatic gas metal arc welding," *Advances in Mechanical Engineering*, vol. 10, no. 8, p. 1687814018781492, 2018.
- [121] V. Malin and F. Sciammarella, "Controlling heat input by measuring net power," *Welding journal*, vol. 85, no. 7, 2006.
- [122] J. F. Lincoln, "The procedure handbook of arc welding," *The James F. Lincoln Arc Welding Foundation*, 2000.
- [123] P. Sharma, S. Chattopadhyaya, and N. Singh, "A review on magnetically supported gas metal arc welding process for magnesium alloys," *Materials Research Express*, vol. 6, no. 8, p. 082002, 2019.
- [124] L. H. S. Barbosa, P. J. Modenesi, L. B. Godefroid, and A. R. Arias, "Fatigue crack growth rates on the weld metal of high heat input submerged arc welding," *International Journal of Fatigue*, vol. 119, pp. 43-51, 2019.
- [125] K. Benyounis, A. Olabi, and M. Hashmi, "Effect of laser welding parameters on the heat input and weld-bead profile," *Journal of materials processing technology*, vol. 164, pp. 978-985, 2005.
- [126] P. Posinasetti and P. K. Yarlagadda, "Meeting challenges in welding of aluminium alloys through pulse gas metal arc welding," *Journal of Materials Processing Technology*, vol. 164, no. AMPT/AMME05 Part 2, pp. 1106-1112, 2005.
- [127] P. Kah, R. Suoranta, and J. Martikainen, "Advanced gas metal arc welding processes," *The International Journal of Advanced Manufacturing Technology*, vol. 67, no. 1-4, pp. 655-674, 2013.

- [128] R. Talalaev, R. Veinthal, A. Laansoo, and M. Sarkans, "Cold metal transfer (CMT) welding of thin sheet metal products," *Estonian Journal of Engineering*, vol. 18, no. 3, p. 243, 2012.
- [129] R. A. Munro, G. Ramu, and D. J. Zrymiak, *The certified Six Sigma green belt handbook*. ASQ Quality Press, 2015.
- [130] W. Chen, J. K. Allen, K.-L. Tsui, and F. Mistree, "A procedure for robust design: minimizing variations caused by noise factors and control factors," 1996.
- [131] A. Freddi and M. Salmon, "Design of Experiment," in *Design Principles and Methodologies*: Springer, 2019, pp. 127-158.
- [132] J. Filliben and W. Guthrie, "NIST/SEMTECH Engineering Statistics Handbook," *Gaithersburg: www.itl.nist.gov/div898/handbook, NIST*, 2002.
- [133] R. K. Roy, *Design of experiments using the Taguchi approach: 16 steps to product and process improvement*. John Wiley & Sons, 2001.
- [134] S. P. Kondapalli, S. R. Chalamalasetti, and N. R. Damera, "Application of Taguchi based design of experiments to fusion arc weld processes: A review," *International Journal of Business Research and Development*, vol. 4, no. 3, 2013.
- [135] Y. Wooluru, D. Swamy, and J. Rangaswamy, "Development of Mathematical Model to Predict Weld Bead Geometry and Parameters Optimization for Pulsed MIG Welding Using Statistical Design of Experiments," *International Journal of Applied Engineering Research*, vol. 13, no. 12, pp. 10298-10309, 2018.
- [136] A. E. Izeda, A. Pascoal, G. Simonato, N. Mineiro, J. Gonçalves, and J. E. Ribeiro, "Optimization of Robotized Welding in Aluminum Alloys with Pulsed Transfer Mode Using the Taguchi Method," in *Multidisciplinary Digital Publishing Institute Proceedings*, 2018, vol. 2, no. 8, p. 426.
- [137] C. Rajendran, K. Srinivasan, V. Balasubramanian, H. Balaji, and P. Selvaraj, "Data set on prediction of friction stir welding parameters to achieve maximum strength of AA2014-T6 aluminium alloy joints," *Data in Brief*, vol. 23, p. 103735, 2019.
- [138] S. Subramaniam, D. White, J. Jones, and D. Lyons, "Experimental approach to selection of pulsing parameters in pulsed GMAW," *WELDING JOURNAL-NEW YORK-*, vol. 78, pp. 166-s, 1999.

- [139] T. Allen, R. Richardson, D. Tagliabue, and G. Maul, "Statistical process design for robotic GMA welding of sheet metal," *Welding Journal(USA)*, vol. 81, no. 5, p. 69, 2002.
- [140] A. Choudhary, M. Kumar, and D. R. Unune, "Experimental investigation and optimization of weld bead characteristics during submerged arc welding of AISI 1023 steel," *Defence Technology*, vol. 15, no. 1, pp. 72-82, 2019.
- [141] D. Nagesh and G. Datta, "Modeling of fillet welded joint of GMAW process: integrated approach using DOE, ANN and GA," *International Journal on Interactive Design and Manufacturing (IJIDeM)*, vol. 2, no. 3, p. 127, 2008.
- [142] B. K. Khamari, S. S. Dash, S. K. Karak, and B. B. Biswal, "Effect of welding parameters on mechanical and microstructural properties of GMAW and SMAW mild steel joints," *Ironmaking & Steelmaking*, pp. 1-8, 2019.
- [143] W. Hackenhaar, A. R. Gonzalez, I. G. Machado, and J. A. Mazzaferro, "Welding parameters effect in GMAW fusion efficiency evaluation," *The International Journal of Advanced Manufacturing Technology*, vol. 94, no. 1-4, pp. 497-507, 2018.
- [144] C. L. Jenney and A. O'Brien, *Welding handbook: welding science and technology*. American Welding Society, 2001.
- [145] V. Vaithyanathan, V. Balasubramanian, S. Malarvizhi, V. Petley, and S. Verma, "Gas tungsten constricted arc welding (GTCAW) parameters optimization to attain maximum tensile strength in Ti-6Al-4V alloy sheets used in aero-engine components," *Multiscale and Multidisciplinary Modeling, Experiments and Design*, pp. 1-11, 2019.
- [146] FRONIUS, "FRONIUS TS SERIES QUICK REFERENCE CARDS MIG/MAG," ed, 2016.
- [147] Mehdi Gharagozloo, Xuan-Tan Pham, and C.-C. Nguyen, "Feasibility study of aluminum deposition by robotic MIG welding process," presented at the CanWeld, Winnipeg/Canada, 2018.
- [148] R. Ranjit, "A primer on the Taguchi method: Society of Manufacturing Engineers," *Estados Unidos: Society of Manufacturing Engineers*, pp. 172-174, 2010.
- [149] B. Jones and C. J. Nachtsheim, "Definitive screening designs with added two-level categorical factors," *Journal of Quality Technology*, vol. 45, no. 2, pp. 121-129, 2013.

- [150] S. Ueguri, K. Hara, and H. Komura, "Study of metal transfer in pulsed GMA welding," *Welding Journal*, vol. 64, no. 8, pp. 242-250, 1985.
- [151] A. Standard, "F2792-12a: Standard Terminology for Additive Manufacturing Technologies (ASTM International, West Conshohocken, PA, 2012)," P. Jain, AM Kuthe, *Feasibility study of manufacturing using rapid prototyping: FDM approach*, *Procedia Eng*, vol. 63, pp. 4-11, 2013.
- [152] A. Saboori, D. Gallo, S. Biamino, P. Fino, and M. Lombardi, "An overview of additive manufacturing of titanium components by directed energy deposition: microstructure and mechanical properties," *Applied Sciences*, vol. 7, no. 9, p. 883, 2017.
- [153] M. Mughal, H. Fawad, and R. Mufti, "Three-dimensional finite-element modelling of deformation in weld-based rapid prototyping," *Proceedings of the Institution of Mechanical Engineers, Part C: Journal of Mechanical Engineering Science*, vol. 220, no. 6, pp. 875-885, 2006.
- [154] P. Colegrove and S. Williams, "High deposition rate high quality metal additive manufacture using wire+ arc technology," *Cranfield University*, 2013.
- [155] M. Freund, V. Ventzke, N. Kashaev, B. Klusemann, and J. Enz, "Thermal Analysis of Wire-based Direct Energy Deposition of Al-Mg using Different Laser Irradiances," *Additive Manufacturing*, 2019.
- [156] Y. Xiong *et al.*, "Process planning for adaptive contour parallel toolpath in additive manufacturing with variable bead width," *The International Journal of Advanced Manufacturing Technology*, pp. 1-12, 2019.
- [157] C. Cunningham, J. Flynn, A. Shokrani, V. Dhokia, and S. Newman, "Invited review article: Strategies and processes for high quality wire arc additive manufacturing," *Additive Manufacturing*, vol. 22, pp. 672-686, 2018.
- [158] J. J. Lewandowski and M. Seifi, "Metal Additive Manufacturing: A Review of Mechanical Properties (Postprint)," Case Western Reserve University Cleveland United States 2016.
- [159] M. Srinivas and B. S. Babu, "A critical review on recent research methodologies in additive manufacturing," *Materials Today: Proceedings*, vol. 4, no. 8, pp. 9049-9059, 2017.

- [160] H. Ye, "An overview of the development of Al-Si-alloy based material for engine applications," *Journal of Materials Engineering and Performance*, vol. 12, no. 3, pp. 288-297, 2003.
- [161] D. Ashkenazi, "How aluminum changed the world: A metallurgical revolution through technological and cultural perspectives," *Technological Forecasting and Social Change*, vol. 143, pp. 101-113, 2019.
- [162] S. Hegde and K. N. Prabhu, "Modification of eutectic silicon in Al-Si alloys," *Journal of materials science*, vol. 43, no. 9, pp. 3009-3027, 2008.
- [163] S. Thapliyal, "Challenges associated with the wire arc additive manufacturing (WAAM) of Aluminum alloys," *Materials Research Express*, 2019.
- [164] S. V. Belyaev *et al.*, "Saturation Dynamics of Aluminum Alloys with Hydrogen," 2017.
- [165] V. Dobatkin, R. Gabidullin, B. Kolachev, and G. Makarov, "Gases and Oxides in Aluminum Deformable Alloys," *Publ Metallurgiya Moscow*, 1976.
- [166] D. Wang *et al.*, "Reducing Porosity and Refining Grains for Arc Additive Manufacturing Aluminum Alloy by Adjusting Arc Pulse Frequency and Current," *Materials*, vol. 11, no. 8, p. 1344, 2018.
- [167] Z. Qi, B. Qi, B. Cong, H. Sun, G. Zhao, and J. Ding, "Microstructure and mechanical properties of wire+ arc additively manufactured 2024 aluminum alloy components: As-deposited and post heat-treated," *Journal of Manufacturing Processes*, vol. 40, pp. 27-36, 2019.
- [168] I. Astm, "Standard Test Methods for Tension Testing of Metallic Materials Designation: E8/E8M-09," *Universidad Del Valle, Pennsylvania*, 2010.
- [169] Q. Wu *et al.*, "Effect of molten pool size on microstructure and tensile properties of wire arc additive manufacturing of Ti-6Al-4V alloy," *Materials*, vol. 10, no. 7, p. 749, 2017.
- [170] A. Waqas, Q. Xiansheng, X. Jiangtao, W. Hongbo, M. Muzamil, and A. Majeed, "Directional Tensile properties of steel structure manufactured by robotic assisted GMAW additive manufacturing," in *2019 16th International Bhurban Conference on Applied Sciences and Technology (IBCAST)*, 2019, pp. 239-242: IEEE.
- [171] Q. Yang, C. Xia, Y. Deng, X. Li, and H. Wang, "Microstructure and Mechanical Properties of AlSi7Mg0. 6 Aluminum Alloy Fabricated by Wire and Arc Additive

Manufacturing Based on Cold Metal Transfer (WAAM-CMT)," *Materials*, vol. 12, no. 16, p. 2525, 2019.

- [172] Y. Kok *et al.*, "Anisotropy and heterogeneity of microstructure and mechanical properties in metal additive manufacturing: A critical review," *Materials & Design*, vol. 139, pp. 565-586, 2018.